Development and Testing of an IceAct Imaging Atmospheric Cherenkov Telescope with Target C based Electronics

Master's thesis in physics

Presented by

Kristof Kremer

14. June 2018

Physikalisches Institut II

Erlangen Centre for Astroparticle Physics

Friedrich-Alexander-Universität Erlangen-Nürnberg

Supervisor: Prof. Dr. Stefan Funk

Abstract

The IceAct is a small scale Imaging Atmospheric Cherenkov Telescope designed to operate in coincidence with the IceCube detector to veto air shower induced neutrinos.
The TARGET C/T5TEA based electronics of the newest version of IceAct are tested and characterized with a single silicon photo multiplier (SiPM) as photo detector. The data stream is examined at all points of the analog and digital data path. The calibration of the Target output data is examined and optimized.
The charge resolution and saturation behavior of a single SiPM pixel is determined by illumination with a homogeneous laser field with tuneable intensities up to the saturation. As there are no official IceAct requirements, the performance is compared to the requirements for the camera system CHEC for CTA. The fractional charge resolution of the IceAct is better than required for CHEC up to its saturation at ~ 500 detected photons per event.
The electronics (SiPM, preamplifier and signal shaping circuit) are simulated with LTSpice and the results are compared to measurements with Target and with an oscilloscope for reference. Furthermore, the saturation behavior of the preamplifier and the shaper is simulated and it is evident that the preamplifier saturates first.
A modified version of a CHEC shaping circuit for analog pulse shaping is compared to the standard issue in respect for gain and signal performance and the modified version has proven to be the favorable choice for the IceAct.
A field test of the telescope setup with the single SiPM has been conducted in the city area of Erlangen. A trigger scan over the night sky background has been performed and cosmic radiation events were detected. With the full camera of 64 SiPM pixels and Winston cones attached to them an increase in sensitivity by a factor of at least $\sim 10^2$ is expected for the full IceAct camera.

Contents

1 Introduction

Astronomy counts among the oldest natural sciences, probably because the night sky is one of the most beautiful and intriguing puzzles that nature has to offer. Today's understanding of the universe is one of the great success stories of human curiosity. Especially during the last 400 years our knowledge of the universe has grown dramatically which has had a great impact on our society and our self conception. For example, the discovery that we are not in the center of the universe or the transition to the heliocentric system altered one of the most commonly held believes at that time.

For a large part of human history the amount of available information about the universe was more or less constant. The only way to observe the stars was through visible light detectable by the naked eye. Then the development of scientific tools enabled a continuous growth of the available information. Two fundamentally different mechanisms or "milestones" can be separated: The first is an increase in sensitivity e.g. to small amounts of visible light. The second one is an expansion of the available set of messengers e.g. to the full spectrum of electromagnetic radiation or particles such as neutrinos or cosmic rays.

The first to achieve a gain in sensitivity was Galileo Galilei in 1609 with the use of an optical telescope for astronomical observation. Thus, much fainter light sources could be detected and the surface of nearby astronomical bodies such as the moon could be studied in far greater detail. However, the visible regime only represents a small part of the electromagnetic spectrum and is thus fundamentally limited to a subset of all available information.

The expansion of the available messengers started in the 20th century with the discovery of cosmic radiation by Victor Hess [9]. Between 1911 and 1913 he undertook several balloon flights to measure the amount of ionizing radiation in different heights with precise electrometers. The amount of ionization increased with height so he concluded that this "cosmic radiation" must be extraterrestrial. In 1968 the first solar neutrinos were detected experimentally [3], which marked the beginning of the promising field of neutrino astronomy.

In contemporary astrophysics it is common practice to use different types of messengers to observe the same source or process. By cleverly combining the information of multiple

messengers one can examine not only the separate effects a process has on each of the messengers but also the interplay and connection between them. Thus, it is possible to reconstruct a more detailed picture of an astrophysical process that is more than the sum of its parts.

A somewhat different approach to reap the benefits of different messengers is using one type of messenger as an auxiliary to improve the quality of the information gained by another. This is especially useful to separate different possible sources for one messenger as one source might emit another type of messenger along with the first one.

This thesis contributes to such a multi messenger approach by constructing and testing an imaging atmospheric Cherenkov telescope as support for the IceCube neutrino observatory on the South Pole. IceCube detects neutrinos but cannot well distinguish (for certain incident angles) if they stem from extraterrestrial sources or from cosmic-ray induced air showers. Detecting an air shower in coincidence with an neutrino event in IceCube strongly implies a terrestrial source and can be used to veto them.

The application of multi messenger astronomy may be a third milestone in the process of gathering information about the universe. It is fundamentally different compared to gaining sensitivity or expanding the set of messengers. With the consistent use of this approach we may hold a key to unlock another part of the puzzle that is our night sky.

1.1 Cosmic Radiation

Cosmic radiation consists of highly energetic particles that originate from extraterrestrial sources and reach earth isotropically. They vast majority of cosmic radiation ($\approx 98,8\%$) is composed of charged particles and the rest are highly energetic photons (γ-rays). The charged components consist mainly of protons (90%) and alpha particles (9%). The remaining fraction consists of bigger atomic nuclei such as e.g. iron cores and of electrons. The spectrum of cosmic radiation covers roughly 14 orders of magnitude, ranging from $\sim 10^7$ eV up to the highest ever measured particle at an energy of $3 \cdot 10^{20}$ eV.

The flux of cosmic rays follows a power law where relatively low energies are much more frequent than higher energies as is shown in Fig. 1. Particles with an energy up to 10^{15} eV or the "knee" of the graph originate from sources inside our own galaxy such as e.g. supernovae shock fronts. Particles up to this energy can be efficiently confined in our galaxy due to the magnetic halo surrounding the Milky Way [16]. Particles with higher energies often escape our galaxy, explaining the steeper decrease in flux for this energy range. Particles with energies above the "ankle" at 10^{18} eV most probably stem from extra-galactic sources such as active galaxy nuclei (AGN), although their exact origin is still unknown.

Very high energy (VHE) cosmic rays are almost completely absorbed by interaction with the earth's atmosphere and it is impossible to measure them directly at ground level. A direct detection is possible in space based satellite observatories, such as e.g. Fermi Lat, but the flux of VHE cosmic rays strongly decreases with energy and the detection area of satellite based instruments is limited to the order of a few square meters for

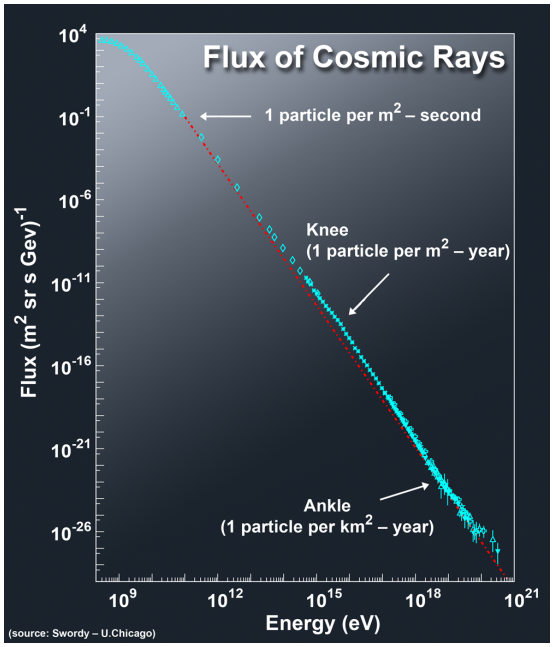

Figure 1 – The energy spectrum of cosmic rays. It covers roughly 14 orders of magnitude and decreases with a power law over the whole spectrum. Two features are visible: The "knee" at $\sim 10^{15}$ eV that marks the end of cosmic rays produced in our galaxy and the" ankle" at $\sim 10^{18}$ eV. [1]

technical and financial reasons. Therefore, the highest energies of the spectrum (above the order of 300 GeV) cannot be detected by satellites within a reasonable time scale. The most successful way to overcome this problem is by using the absorption in the earth's atmosphere to indirectly detect cosmic rays by their decay products.

1.2 Air Showers

Upon entering the earth's atmosphere cosmic radiation interacts with air molecules and decay into secondary particles. For VHE cosmic radiation these secondary particles still posses enormous energies and produce additional secondary particles themselves. This process repeats several times and leads to the formation of an "air shower" consisting of many secondary particles as is illustrated in Fig. 2. VHE γ-rays produce a very narrow shower along the trajectory of the initial particle whereas protons and heavier nuclei form a more jagged cone like structure.

1.2.1 Electromagnetic Showers

When entering the atmosphere VHE cosmic γ-rays undergo pair production in the presence of the atomic nuclei of the air. The nuclei are necessary for momentum conservation of the process. The resulting electron and positron are both scattered in the electric fields of additional nuclei along their path, thereby experiencing an effective acceleration which

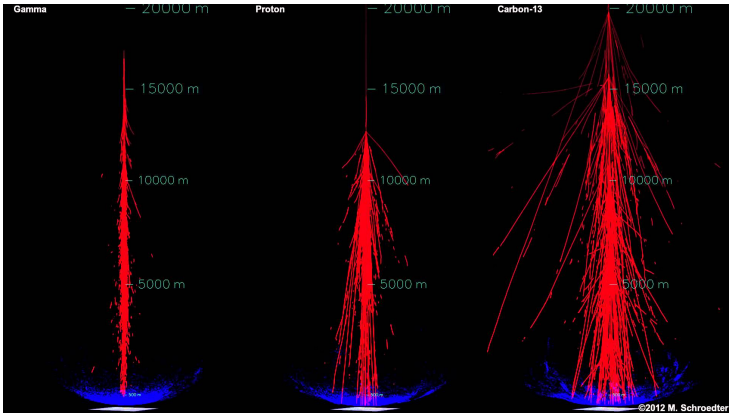

Figure 2 – Simulation of different kinds of air showers. The red lines symbolize the secondary particles and the blue elements symbolize the Cherenkov light front that is emitted by the air shower. From left to right the showers are created initially by a γ-ray, a proton and an carbon nucleus. [18]

leads to the emission of Bremsstrahlung in the form of photons. These secondary photons can produce additional electron positron pairs, if their energy is still high enough (greater than two times the electron rest mass of 511 keV). Those two processes can continue multiple times, producing an air shower of many secondary particles. A simple model of this decay mechanism is illustrated in Fig. 3.

The energy loss by Bremsstrahlung is proportional to the particle's energy and depends on the density of the medium and the distance traveled. A measure to quantify when the energy of a particle is reduced to $1/e$ of its initial energy by Bremsstrahlung is called the radiation length X_o. It is defined by the amount of matter a particles crosses and has the dimension of density times distance $X_0 = \rho \cdot d$ which corresponds to a value of $37.2\, g\, cm^{-2}$ for air at sea level. Note that X_0 is also used as a measure for the mean distance the particle travels before it has lost all but $1/e$ of its energy, which corresponds to a value of ≈ 300 m at sea level. Furthermore, it is related to the mean free path of pair production by a factor of 7/9 [7].

Some insight on the development of air showers can be gained by applying a simple model introduced by Bethe and Heitler in 1954 [2], which is illustrated in Fig. 3. They make the following assumptions:

- Decays only happen via Bremsstrahlung or pair production.
- The energy loss via ionization of air molecules is negligible for the shower development.
- The radiation length for Bremsstrahlung and the mean free path for pair production are considered to be equal.
- The total energy is assumed to be distributed equally between all secondary particles

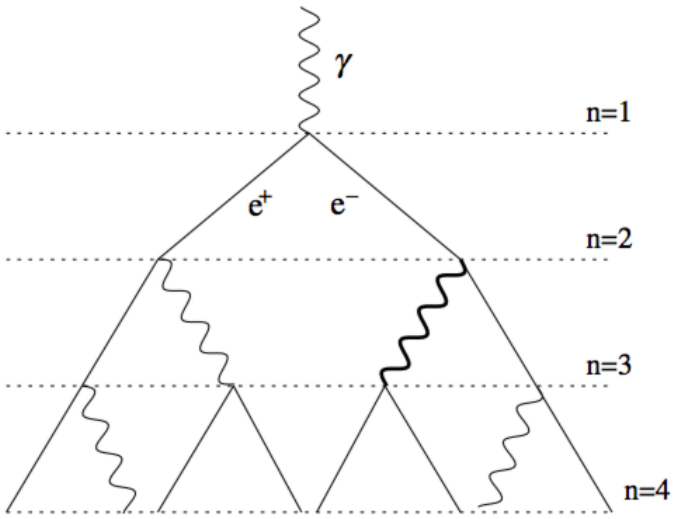

Figure 3 – Schematic of the Bethe&Heitler model of an electromagnetic air shower [4]

In this model the number of secondary particles m in the shower grows exponentially with the radiation length:

$$m = 2^n = 2^{\frac{x}{X_o}} \tag{1}$$

Thereby x is the distance from the shower origin and $n = x/X_0$ denotes the level of branchings into secondary particles or the "depth" of the shower. Each particle is assumed to have an energy of

$$E(n) = \frac{E_o}{2^n} \tag{2}$$

where E_0 denotes the initial energy of the cosmic c γ-ray.

The shower "dies out" if the energy $E(n)$ is comparable to the critical energy $E_c \approx 81\,MeV$ i.e. the energy loss by ionization during one radiation length. In this case the remaining energy of the particle is spent ionizing air molecules along its path and no further particles are generated. The depth of the shower m_{max} can be calculated by setting

$$E(n_{max}) \stackrel{!}{=} E_c \tag{3}$$

which yields:

$$n_{max} = \frac{ln(E_o/E_c)}{ln2} \tag{4}$$

A typical shower with an initial energy of $E_0 = 1\,TeV$ and an initial interaction height of $h_o \approx 25\,km$ above sea level has a maximum depth of $n = 13.6$. Such an air shower usually reaches its maximum at a typical height of $8\,km$, since the density of air depends on altitude and thus the mean distance before a branching increases with height above sea level.

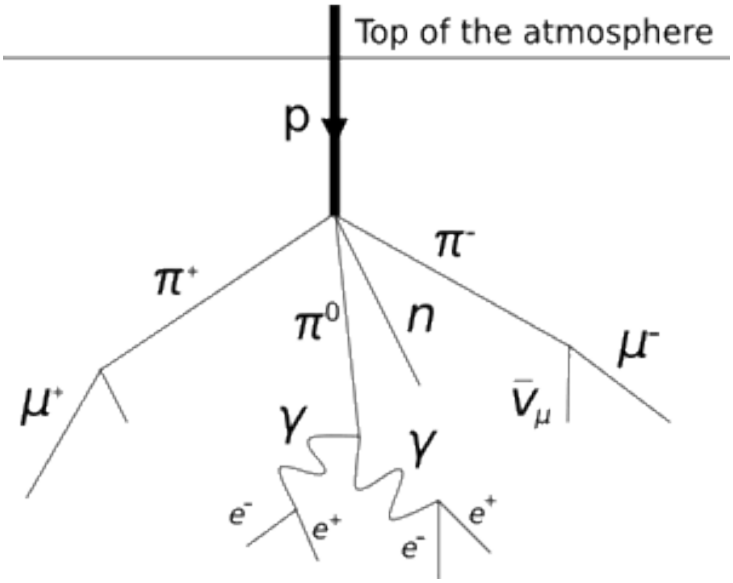

Figure 4 – Schematic of a hadronic air shower that decays into pions, muons neutrinos and an elm. component that is created by the decay of the π_0 into two photons.

1.2.2 Hadronic Showers

Hadronic showers are created by highly energetic charged particles (mostly protons) instead of γ-rays. In contrast to electromagnetic air showers, mainly complex strong-force reactions take place in a hadronic shower. Due to the higher transverse momentum that the secondary particles gain in these reactions, the shower is spread out much further than a purely electromagnetic shower.

Furthermore, the strong force reactions create many different specimens of secondary particles, such as pions or hadrons. Secondary hadrons also interact via the strong force, which causes the formation of hadronic sub-showers. The neutral pion π_0 plays a special role, as it decays into two photons after a mean lifetime of $(8.4 \pm 0.4 \cdot 10^{-17}\, s)$, which initialize an electromagnetic sub-shower. A schematic of a hadronic shower which illustrates some of the main decay mechanisms is shown in Fig. 4. Note that e.g. the charges pions can decay into muons and neutrinos, which are by themselves indistinguishable from those produced by extraterrestrial sources.

1.3 Cherenkov Radiation

An especially useful feature of air showers is that they produce Cherenkov light, which can be detected by a ground based Imaging Cherenkov Air Shower Telescope (IACT). The Cherenkov light travels in a cone along the main direction of the shower and its intensity is proportional to the energy of the initial particle.

Cherenkov light is produced due to the difference in the speed of light in vacuum (c) and in matter (c'). In a medium (e.g. the atmosphere) the phase velocity of light is reduced by a factor of $1/n$ with n the refraction index of the medium.

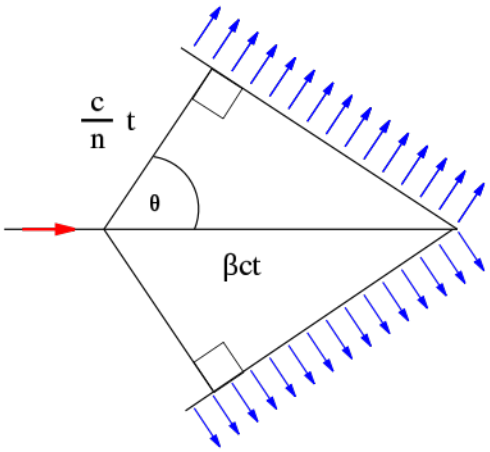

Figure 5 – Illustration of the Cherenkov cone formation[12]

Charged particles that are created in an air shower travel at a speed $v_p = c \cdot \beta$ that exceeds the phase velocity of light in the atmosphere. In a classical view the charged relativistic particle polarizes the molecules of the surrounding air and causes constructive interference of electromagnetic waves in its wake, which leads to the emission of Cherenkov light. Phenomenologically this is similar to the Mach cone of a plane flying at supersonic speed, which causes sound waves in its wake that spread spherically but cannot overtake the plane and thus create a shock front.

The formation of the Cherenkov cone is illustrated in Fig. 5. The red arrow points in the direction of the charged particle; the left corner of the triangular marks the position of the particle at a time $t = 0$, the right corner at a later time $t = t_1$. During that time the particle travels the distance $d_p = v_p \cdot t_1 = \beta \cdot c \cdot t_1$. But the emitted Cherenkov light (blue arrows) travels only a distance of $d_c = \frac{c}{n} \cdot t$. Thus, the opening angle θ of the cone is defined by:

$$cos(\theta) = \frac{1}{n \cdot \beta} \tag{5}$$

which can only be satisfied for

$$\beta \geq \frac{1}{n} \tag{6}$$

as the cosine must be smaller than 1. For $\beta < \frac{1}{n}$ no Cherenkov light is emitted.

For highly relativistic (secondary) particles created in VHE cosmic radiation $\beta \approx 1$ and the formula reduces to:

$$cos(\theta) = \frac{1}{n} \tag{7}$$

which puts a constraint on the maximum opening angle θ_{max} of the cone depending on the refraction index of the medium:

$$\theta_{max} = arccos\left(\frac{1}{n}\right) \tag{8}$$

Since the refraction index of the air grows with density, θ_{max} grows along the path of an air shower through the atmosphere. This leads to a focusing effect of the Cherenkov light, because cones that are emitted closer to the ground have a wider opening angle but less time to spread. Thus, they cover roughly the same area on the ground as cones emitted further up.

The minimal energy a particle must posses to emit Cherenkov light can be calculated using the condition given by Eq. 6. It depends on the rest mass m_0 of the charged particle and is given by:

$$E_{min}(m_0) = \gamma \cdot m_0 \cdot c^2 = \frac{m_0 \cdot c^2}{\sqrt{1 - n^{-2}}} \tag{9}$$

The minimum energy is directly proportional to the rest mass m_0 of a particle. Thus, Cherenkov light is mainly emitted by the lightest charged particles i.e. electrons and positrons and the emission from heavier particles such as muons is suppressed.

However, it is possible to distinguish different types of air showers by the pattern of the Cherenkov light they emit. Hadronic showers produce more ragged Cherenkov patterns than electromagnetic showers. The sub showers that can form in hadronic air showers, sometimes lead to smaller Cherenkov flashes that are separated from the main flash.

1.4 Imaging Cherenkov Air Shower Telescopes (IACTs)

IACTs are a tool to detect the Cherenkov radiation from air showers and reconstruct the properties of the initial cosmic radiation that produced them. An IACT is similar to an optical telescope in the sense that it collects (Cherenkov-)light via a lens or mirror and focuses it on a camera. Air shower induced flashes of Cherenkov light are very faint, however, and it is difficult to separate them from the night sky background. Since an optical telescope always measures night sky background in the same wavelength band as Cherenkov light, there is no way of distinguishing the two kinds of photons by the camera itself.

The best way to challenge this problem is by using ultra fast cameras and electronics that can take data at a rate of $\sim$1 Gigasample per second (GSA/s). Cherenkov light flashes occur within a very short time in the order of $\sim 10\,ns$ during which several Cherenkov photons are deposited in a camera pixel. The number of photons depends on the energy of the shower. The rate of night sky background induced photons, however, is constant and statistically distributed over time. Thus, if several photons are registered in a camera pixel within one time step ($\sim 1\,ns$) the probability that they originate from an air shower is high. Applying cut criteria on the number of photons allows to separate Cherenkov events from the background within a certain margin of error that is due to statistical pile-ups of background photons.

To handle the large amount of data that this method creates, it is necessary to preselect only the parts (time intervals) of the signal that contain Cherenkov photons. This is commonly done by using an analog signal buffer and a mechanism that only triggers when a certain threshold of photons per pixel is exceeded. Then only a small time interval around the trigger time is selected from the buffer and digitized to be stored for further use. The time interval is chosen so that the full waveform (signal pulse) of one event is recorded; typically this interval is in the order of $\sim 100\,ns$.

Cherenkov light peaks in the near ultraviolet at an wavelength of ~ 330 nm, so IACT optics are optimized for that wavelength. A cutoff for longer or shorter wavelengths has to be applied, because the intensity of the Cherenkov light strongly drops for other wavelengths but the night sky background does not. Thus, the signal-to-noise ratio decreases if the bandwidth of accepted light is not cut accordingly, for example by the optical properties of the lens or mirror.

The light collection areas of IACTs spans a wide range of sizes and go from $\sim 12.5\,m^2$ for the small sized Telescopes (SST) in the planned Cherenkov Telescope Array (CTA)) up to $614\,m^2$ for the High energy stereoscopic system (H.E.S.S.). The range of cosmic radiation energies that can be resolved with arrays of IACTs spans from $20\,GeV$ up to$300\,TeV$ (for CTA). Typical fields of view for IACTs range from 5° for H.E.S.S. to 9° for the small-size telescopes of CTA.

IACTs can also be combined in an array of several telescopes that operate in a joint mode. This improves the sky coverage and thus the observed volume of air which yields a higher possibility to detect rare VHE cosmic radiation events. Furthermore, the telescopes can be operated in a stereoscopic mode to better reconstruct the origin and direction of the shower by looking at it from different perspectives.

1.5 The IceAct Telescope

The so called IceActs are small scale and cost efficient imaging atmospheric Cherenkov telescopes. The acronym IceAct stems from their chief purpose as an support and veto telescope for the South Pole based IceCube experiment, as discussed in the next section. The main focus of the IceAct project is to build relatively cheap IACTs (with an estimated price of 5500 € per telescope [8]) and a large field of view of 12°, so that many telescopes can be built and operated in parallel to increase sensibility and maximize sky coverage while maintaining overall reasonable cost. Therefore, the design is simple (as described in section 2) and the camera features only 64 SiPM “pixels”. Furthermore, the telescope is quite small and light ($\sim 20\,kg$) with a lens diameter of $\sim 60\,cm$ and a resulting light collection area of only $\sim 0.3\,m^2$. The telescope is built with the South Pole as an operating environment in mind and therefore it has to withstand low temperatures and operate with low power consumption, as power is limited and expensive to generate at the South Pole.

Previous attempts to measure Cherenkov light at the South Pole have been made, e.g. the VULCAN experiment. In contrast to the SiPM based imaging IceAct the VULCAN telescope featured only a single photo multiplier tube (PMT) as photodetector and was

thus unable to image Cherenkov air showers. This was a problem because light from the Aurora Australis hitting the single pixel disturbed the whole measurement. In IceAct the camera pixels that are affected by the aurora can be detected by a continuously high trigger rate and can be excluded for the duration of the aurora. The remaining pixels and thus the majority of the telescope is still functional, which will be a great benefit in comparison with VULCAN.[13]

1.6 Possible Applications of the IceAct

The IceAct is mainly designed as veto telescope for IceCube at the South Pole, to separate extraterrestrial neutrinos from neutrinos born in air showers. However, the IceAct is still a fully operational (although small) imaging Cherenkov air shower telescope and can be applied as such. Due to the cost efficient design, several IceActs can be combined to increase sky coverage of the telescope for veto purposes or for use in a stereoscopic approach to enhance the sensitivity of other specialized cosmic radiation experiments. Furthermore, IceActs can be used as a tool to perform intensity interferometry to test this concept for large scale IACT arrays.

1.6.1 IceCube and IceTop [6]

IceCube is a neutrino observatory that uses a cubic kilometer of arctic ice as detection medium. When a neutrino interacts with the ice it creates secondary (charged) particles that in turn create Cherenkov light similar to an air shower, but with transparent ice as medium. The Cherenkov light is measured by several photo multipliers that are set into the ice in a 3-dimensional grid. From the direction and intensity of the Cherenkov light the original energy and direction of the neutrino can be calculated. To shield the detector from cosmic ray induced muons or other charged particles that would create Cherenkov light in the ice, the detector area is located deep underground with a 1450 m thick ice layer between it and the surface.

The purpose of IceCube is to measure neutrinos of extraterrestrial origin, to gather information about astrophysical processes. However, neutrinos can also be created by air showers from cosmic radiation, as discussed in section 1.2., and the detector cannot distinguish these two different origins of neutrinos as they show the same reaction in the ice.

One possibility to distinguish them is by their energy, as shower induced neutrinos have (on average) less energy than cosmic ones. Thus, an energy cutoff can be defined above which neutrino events are considered as cosmic.

Furthermore, muons can produce a neutrino-like signature in IceCube and thus these events need to be separated. Therefore, the direction of the particle track in the ice is important. When a particle enters the detector from below, it has crossed the earth before interacting with the detector ice. Since only neutrinos posses a cross section that

is small enough to pass through the earth, muons can be excluded as a possible source for registered up-going particle tracks in IceCube.

For down-going particle tracks that enter the detector, the situation is more complicated. If the particle track starts within the detector, it can be assumed to be a neutrino, as muons are absorbed in the ice layer above the IceCube detector. If, however, a particle interacts with the ice layer outside the detector volume and the cone of its Cherenkov light passes into IceCube, it is not possible to identify it as a muon or neutrino track by IceCube alone.

It is thus extremely important for the performance of IceCube to have effective means of separation, so that cosmic neutrino events can be isolated from those events that are induced by muons or air shower neutrinos.

The IceTop detector, which is located above ground on top of IceCube, has been built for this purpose. It uses 162 ice tanks to detect particles produced in air showers by the Cherenkov light they produce in the frozen water of the tanks. If an air shower event is detected by IceTop and simultaneously (within a certain time interval) IceCube also detects an event, this event is considered to be of terrestrial origin and is discarded.

However, IceTop only covers a field of view of 37° directly above IceCube and has a rather high energy threshold of $\gtrsim 300$ TeV [6]. To cover the same area with IceActs, eight arrays of seven telescopes each would be needed. One array in the very center atop IceCube and seven more arranged in a ring of $300\,m$ radius around it.[8]

Especially neutrinos that originate from the galactic center, which lies at a declination angle of $\theta = 68°$, cannot be vetoed by IceTop. But a ring of ≈ 30 IACTs (with adapted field of view) arranged 6 km from the IceCube center, as proposed in [8], would be sufficient to cover a region of 2° around the galactic center. This is illustrated in Fig. 6.

1.6.2 Intensity Interferometry

Another application possible application of the IceAct is the field of intensity interferometry. In contrast to amplitude interferometry, where the amplitudes and phases of different wave packages interfere, intensity interferometry analyses the correlation of the fluctuations of the intensity measured at different points in time and/or space. Such fluctuations always occur but in particular if star light is observed, they are correlated in time and space. For example, when the telescopes are moved gradually away from each other along a baseline, the intensities decorrelate. The shape of that decay in the correlation is ruled by the spatial characteristics of the observed star. The simplest parameter which can be determined is the angular diameter [5].

Two or more IceAct can be used to create such an intensity interferometer by correlating the electronic signal from each of them which is far easier than interfering optical signals over a long baseline. By testing this approach with the IceAct, valuable information about a possible use of big IACT arrays such as CTA as intensity interferometers can be gained.

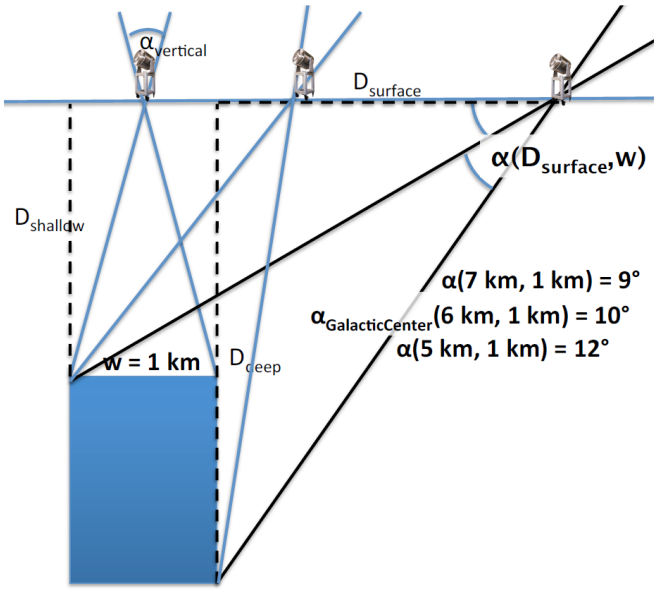

Figure 6 – Schematic of the IceCube geometry and the possible benefits in acceptance angle and detection probability by the application of a ring of IceActs surrounding the IceCube detector on the surface. Especially the galactic center, which is a main source of high energy neutrinos, can be covered by a veto method. The blue rectangle marks the approximate cylindrical shape of the ice cube detector. The full lines show the angles under which particles can reach the IceCube detector and thus the field of view a veto telescope needs to cover. [8]

1.6.3 Other Application Possibilities

Many experiments looking for cosmic radiation are strongly focusing on only one aspect of the shower, such as precise measurement of the total energy, high energy threshold or exact reconstruction of the shower origin. This often comes at the cost of accuracy in other aspects, as an experiment that is superior in all aspects would be much more expensive. However, with the addition of a few comparably cheap IceActs it might be possible to increase the performance in these "weak points" in a cost efficient manner. Thus, it will be worthwhile to consider possible experiments where IceAct can be used as a support telescope, once its final design is complete and tested. However, no detailed considerations for this have been made in the scope of this thesis.

2 Components of the IceAct Telescope

2.1 Mechanical Components

Tubus The IceAct consists of a main tubus of ∼60 cm radius and 60 cm height made out of carbon fiber. This small and lightweight design ensures good maneuverability, as the total weight of the telescopes is in the order of 20 kg. Currently, a simple aluminum mounting device enables the telescope to stand alone and point directly upwards. A more advanced version that will enable the tubus to be mounted on a standard telescope mounting with free moveability and active tracking is currently under construction. A picture of the telescope is shown in Figure 7 a). The black paper in a cone around the lens was added as a stray light shielding for a first field test in the city area of Erlangen.

The tubus has plastic flanges on the top to hold the plastic lens and the protective fused silica glass plate on top of it. The camera is located at the center at the bottom of the tubus and is also held in place by a plastic flange that covers the bottom of the tubus and shields it from stray light from below. A detailed schematic of the tubus is shown in Fig. 8.

Fresnel Lens At the upper end of the tubus sits a plastic Fresnel lens which focuses incoming light on the Camera at the bottom of the tubus. Due to its design, a Fresnel lens is much thinner than a conventional lens. It is cheaper, reduces weight and minimizes absorption of UV light in the lens material. The image quality of a Fresnel lens is inferior to that of a conventional lens, but for the application in an IceAct with 64 camera pixels it is fully sufficient. The main goal is to optimize the light intensity that arrives at the camera.

A transparent plate of fused silica glass is located above the lens to protect it from environmental impacts such as scratches or dirt that would accumulate in the rills of the lens. Due to its smooth surface it is easily cleanable and snow coverage can be wiped off.

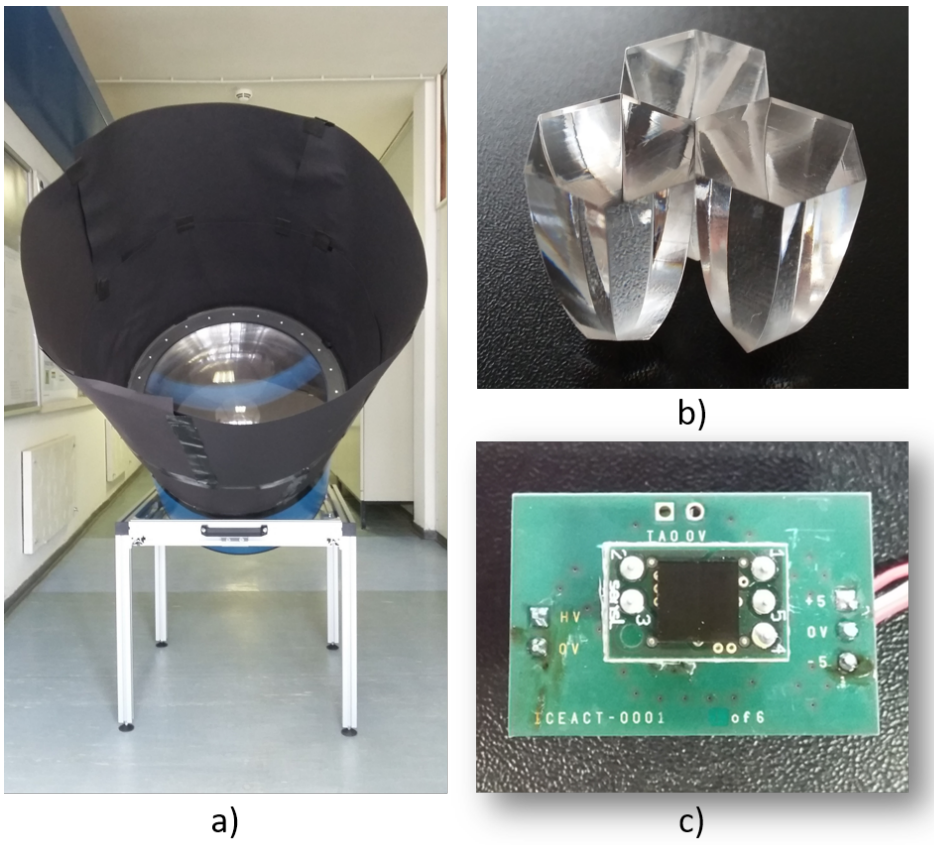

Figure 7 – Telescope tubus and lens with stray light shielding and aluminum mounting. The telescope is tilted from its mount for better visibility of the components (a). Three Winston cones (b). SiPM with underlying preamplifier board (c)

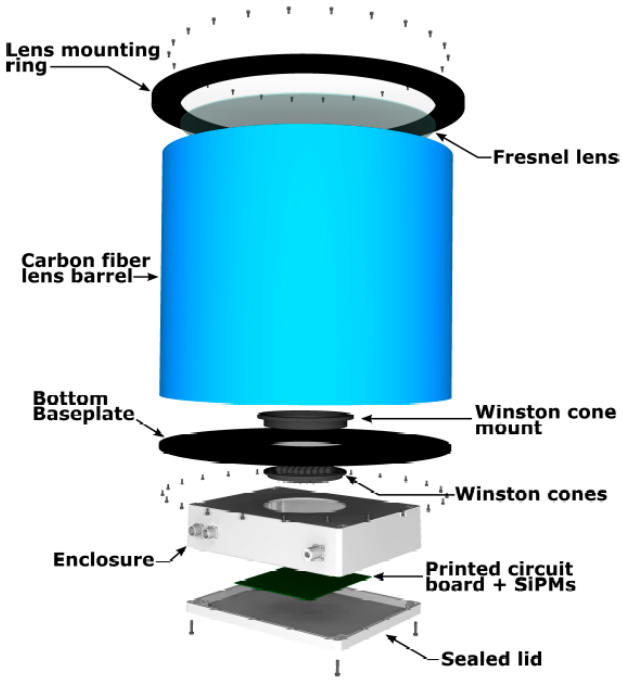

Figure 8 – Detailed schematic of the telescope tubus

Winston Cones Winston cones are "light funnels" that guide incident light from their large entry surface to their smaller exit surface. The cones used here are made from UV transparent Plexiglas which has a higher refractive index than the surrounding air. The light is guided along the cone by total reflection along its walls, similar to an optical fiber. A picture of such a Winston cone is shown in Figure 7 b).

As described in the next Paragraph the IceAct camera features a hexagonal pixel layout, but the used SiPMs are quadratic in shape and cover a smaller area than the whole pixel. In order to optimize the light yield, Winston cones are used to guide the light onto the SiPMs. Therefore one Winston cone is glued on top of each SiPM. Their entry surface is hexagonal and matches the pixel geometry of the camera; their exit surface is quadratic to match the shape of the SiPMs. Thus, the effective area of each SiPM is increased roughly by a factor of five which is determined by the ratio of entry to exit surface of the cone (not taking into account possible losses in the cone itself or the transition between air and cone or cone and SiPM).

The additional loss of image quality through the Winston cone is negligible for this application, since each SiPM functions as one pixel. It does not posses internal spacial resolution, but only detects the intensity of the incident light.

2.2 Silicon Photo-multiplier (SiPM)

A silicon photo-multiplier is a semiconductor based device to detect low intensity light down to single photons. In principle it is a p-n diode operated in reverse direction. The

applied voltage exceeds the breakdown voltage of the diode. An incident photon that is absorbed in the depletion zone will create an electron hole pair. The two charge carriers are then accelerated in different directions and will create an avalanche of secondary charge carriers until the field breaks down. This leads to a short current spike, indicating that at least one charge separation event has taken place inside the diode. However, this does not contain any information on how many photons have interacted in the SiPM, because during the avalanche, and in a short refractory period directly after it, additional photons have no effect. Furthermore, the operation above breakdown voltage also leads to a constant rate of dark counts, since thermally excited electrons inside the depletion zone trigger an avalanche as well.

The 6x6 mm SiPM (SensL MicroFJ-60035-TSV) used in this thesis is shown in Fig. 7 c) and features 22292 micro cells which are operated in parallel and are arranged in a grid formation. If several photons hit several different micro-cells, they will all produce identical output pulses which are summed up. The charge of the summed pulse is proportional to the number of fired micro-cells and thus to the number of detected photons. Note that this proportionality breaks down for a large number of photons ($\approx$ number of micro-cells) because this increases the probability that a micro-cell is hit by more than one photon, which will then not produce additional charge. However, for the operation in the IceAct this effect is negligible since the subsequent electronic components begin to saturate for signals of $\sim$240 photons and the number of incident photons cannot be reconstructed for more than $\sim$800 photons.

Advantages: The main advantage of SiPM over conventional PMTs is the lower operation voltage. The SiPM used in this thesis requires only $\sim$ 30 V for operation, compared to the order of 1 kV for PMTs. This greatly reduces the power consumption and makes it an ideal choice for remote locations such as the South Pole. Furthermore, the SiPM is very compact and robust in its design and immune to magnetic fields. A downside, however, is the higher noise due to dark counts.

Crosstalk: Neighboring micro cells are not fully isolated from each other but are connected via the coating atop the cells that protects them from environmental influences. The coating enables photons that are created during an avalanche in a micro cell to cross the boundary and cause an avalanche in the adjacent micro cells. This phenomenon is called crosstalk. Thus, every fired micro cell (due to an incident photon or a dark count) has a certain probability to cause another micro cell to fire as well. This is negligible for high amplitudes ($\geq$ 10photon events) but reduces the charge resolution for small numbers of photon events (p.e.), since a single incident photon has a probability to be counted as two or more photons. Thus, one cannot say with certainty if a two p.e. signal is caused by two incident photons or by one incident photon plus crosstalk.

2.3 Electronics

2.3.1 Preamplifier

A preamplifier (model LHM6714 from Linear Technologies) is located directly behind the SiPM to minimize the influence of noise on the weak signal of the SiPM. It is shown together with the SiPM in Figure 7 and will be denoted as "preamp" from now on. It consists of an operational amplifier in trans impedance mode. The opamp amplification is not equal over the frequency range and increases for higher frequencies. Thus, a capacitor is added in the feedback loop that dampens the amplification for high frequencies and acts as compensation.

2.3.2 Shaper

The signal pulse of the SiPM features a long decay time - the "tail"of the pulse - in the order of 100 ns. This feature is still present after the preamp and can cause a "pile up" of the signal for high data rates. A pile up occurs when a second signal pulse is emitted before the tail of the first one has completely subsided. If this takes place multiple times, a significant offset can be added to the signals causing them to hit the edge of the dynamic range of the electronics. In this case, valuable information is lost since parts of the pulse can no longer be detected by the readout electronics.

In order to avoid a pile up of the signal, a shaper is deployed after the preamp. The main purpose of the shaper is to shorten the pulse without loosing any information. Furthermore, the shaper amplifies the signal amplitude by an additional factor of $\sim$2. The shaper consists of two operational amplifiers with a pole zero cancellation between them. It consists of a parallel capacitor and resistor. The capacitor acts as a high pass filter that shapes the edges of the signal with a sharper rise and fall time. However, this produces a large undershoot of the signal directly after the peak. To compensate for that, the parallel resistor supplies a positive current that mitigates this effect to a certain extend. More detailed examinations of the shaper behavior are given in section 4.3.

Modified Version and Comparison to Standard Version Throughout this thesis two different configurations for the shaper have been evaluated. They differ in their gain and in the exact way they shape the tail of the pulse. One configuration is the standard issue shaper as used in the compact high energy camera (CHEC) designed for small and medium sizes telescopes of the planned Cherenkov Telescope Array (CTA). The other channel has slightly modified values for the capacitors and resistors of the operational amplifier and a high pass filter to deal with the longer tail of the SensL SiPM. This yields a higher gain and shortens the pulse further, but comes at the cost of a larger undershoot after the pulse, as the stronger shaping pulls the signal value below the baseline directly after the pulse, as discussed in sections 3 and 4.

2.4 TARGET C/T5TEA Module

TARGET is a family of application specific integrated circuits (ASICs) used for processing the photodetector signal in IACTs.

In the most recent version Target is split into two ASICs: The Target C which samples the photodetector signals, stores it in a buffer and digitizes it on demand, and the T5TEA (Target 5 Trigger Extension Asic) which takes care of triggering and features an adjustable trigger threshold. This significantly improves the trigger performance, while retaining good charge resolution and a high dynamic range by limiting the crosstalk between the sampling and the triggering path [10].

TARGET C/T5TEA was designed for the Compact High Energy Camera (CHEC) that is used in prototypes for the small size telescopes of the Cherenkov telescope array (CTA) and is also planned to be used for one proposed mid size telescope [10]. The requirements of data processing in those telescopes are very similar to those of an IceAct, which makes Target a very suitable and available choice for the signal processing in IceActs.

The Target ASICs are mounted on a compact Target module that also features a Field Programmable Gate Array (FPGA) that controls the ASICs and serializes the data stream. The Target module features 64 input channels; one for each SiPM photodetector pixel. There are four groups of TARGET C/T5TEA pairs which process 16 channels each. This allows a very compact and cost efficient design, as the total number of printed circuit boards is small. The digitized data is packaged and send to a computer via an optical cable.

A schematic overview of the Target signal paths is given in Fig. 9. The photodetector signal for each channel first arrives at the 64 cell sampling array. This switched capacitor array is divided into two 32 cell blocks which operate in a “ping pong” fashion. During one half cycle the first 32 cells sample data by sequentially connecting and disconnecting the signal to the capacitors, while the second 32 write them into the analog buffer array. In the second half cycle the roles are reversed. Note that the 32nd cell of each sampling block has a slightly different behavior than the others due to the manufacturing process of the ASIC board. Thus, every 32nd entry in the storage array has a different value than the others, which must be compensated by calibration (as discussed in section 6). The analog buffer array consists of 16384 capacitors that enable a storage time of ∼16 µs and are arranged in 512 blocks of 32 cells each. They form an array of eight rows and 64 columns. A storage buffer of this length is necessary for the time correlation of the signals of a big Cherenkov telescope array with long distances between the telescopes. However, this feature is not needed to its full extend for the current stage of testing of the IceAct. Thus, only the first 4096 blocks of the buffer are used throughout this thesis.

Triggering is handled by the T5TEA, and is arranged in four trigger groups of four channels for each ASIC. The trigger compares the analog sum of the four channels to an adjustable threshold voltage. The highest possible trigger rate of the T5TEA is roughly $\sim 50\,MHz$. However, the highest possible event rate is determined by the digitization time of $\sim 12\,\mu s$ per read out block which limits the maximal event rate to $\sim 16.6\,kHz$ for five read out blocks. The reference voltage of the summing amplifier that performs

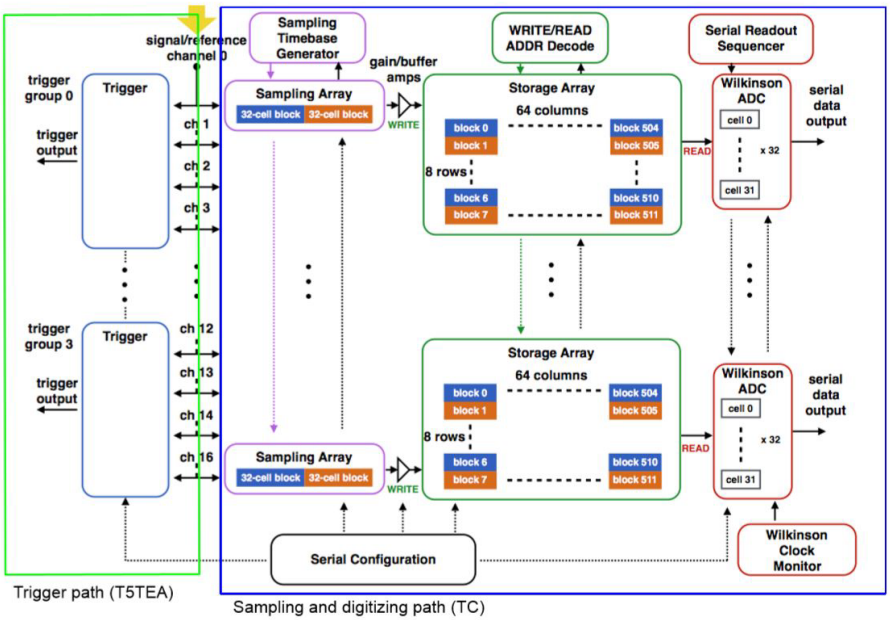

Figure 9 – Schematic of the Target module trigger (T5TEA) and sampling (TC) path. For each channel a sampling array of 64 cells operates in a "ping pong" mode where 32 cells sample incoming data while the other 32 write their content to the storage array. After one half cycle they switch their roles. The sample array contains 16384 cells which store ~ 16 µs at a sample rate of 1 GHz. The trigger compare the signal of in the sampling cells of a trigger group of four channels with a threshold value. If they surpass this value the information is send to a Wilkinson ADC with a time stamp. The storage array entries that corresponds to the sampled values are selected and digitized. [19]

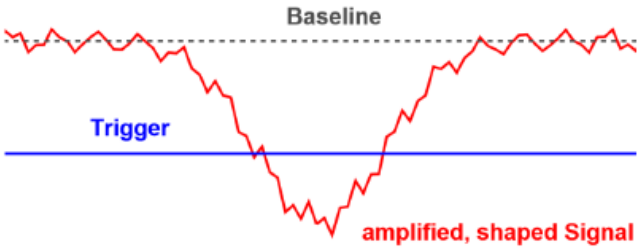

Figure 10 – Illustration of the signal with respect to the trigger threshold of the T5TEA ASIC. Increasing the parameter PMTRef4 shifts the signal baseline away from the trigger. Increasing Thresh shifts the trigger towards the signal. [17]

the analog sum can be adjusted by the parameter PMTref4 which can be set by the user. Increasing PMTref4 shifts the signal relative to the comparator threshold of the trigger ASIC. Its counterpart is the parameter Thresh which adjusts the comparator threshold. This is illustrated in Fig. 10. If the threshold is surpassed, a trigger event is initiated and causes the readout and digitization of all 64 channels from the buffer array in a window of selectable size. In this thesis a window length of 128 data points, corresponding to $128\,ns$ (or four blocks) is chosen as it covers the full waveform of a signal.

The data in the storage array can be accessed and digitized on demand by Wilkinson analog to digital converters (ADCs). The ADCs apply a voltage ramps to all channels and compare it to the voltage of the storage capacitor. Simultaneously, a clock runs that measures the time until the two signals match. From the time stamp, the voltage value of the capacitor can be calculated. Digitization is controlled by the FPGA which can be set to an external or internal (T5TEA) trigger. An adjustable trigger delay ($370\,ns$ for external trigger and $440\,ns$ for internal trigger) compensates the internal run time of the trigger process and ensures that the correct part of the buffer array (that contains the triggered upon waveform) is read out and digitized.

2.5 Evaluation Board

In this thesis, however, an evaluation board was used. It contains 16 channels but features the same Target C and T5TEA ASIC and FPGA as on the Target module. A main difference is that the shaper is not integrated, but a shaper test board can be connected via MMCX cable. This allows to easily test different versions of the shaper as discussed above. Since only a single SiPM photodetector and thus only one channel was used in this thesis, the evaluation board was sufficient for all purposes. 14 of the other 15 channels on the board have been used for common mode corrections of the signal as discussed in section 6.1.2.

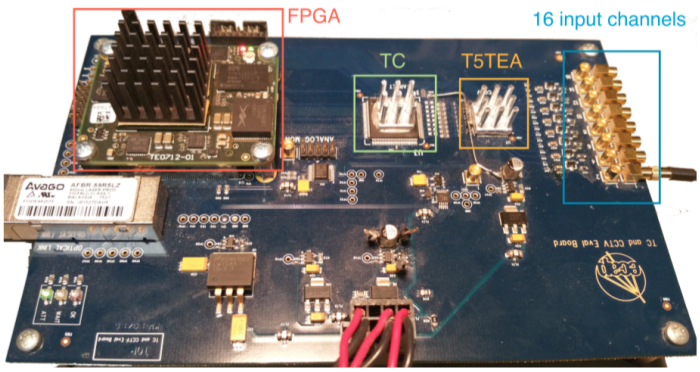

Figure 11 – Photo of the evaluation board used throughout this thesis. In its key components it is similar to the Target module, but it contains only 16 instead of 64 channels.

3 Signal Stages

This section gives an overview over the shape of the signal pulse along the different stages in the electronic and digital signal path. It covers the SiPM and preamp output pulse as well as the shape of the waveform after digitization with Target and the application of further calibrations. The exact methods of measurement and calibration are discussed in section 5.

SiPM and Preamp: Since the preamp is directly attached to the SiPM, the signal can only be measured after the preamp. The shape of a typical signal pulse, measured with the oscilloscope, is shown in Fig. 12 in yellow. The preamp inverts the signal and the long tail of the SensL SiPM pulse is visible. The full width half maximum (FWHM) of the pulse is $\sim 50\,ns$.

Shaper: After the shaper the signal pulse is shortened in time with much steeper rising and falling edges and a higher peak amplitude. This comes at the cost of an undershoot directly after the pulse which is created by the down-shaping of the falling edge. The shaping is necessary to avoid a pile up of pulses that are created in close succession, because otherwise the signal would shift across the trigger threshold and eventually hit the upper end of the dynamic range of Target over time. A typical signal pulse after the (modified) shaper is shown in Fig. 12 in blue. The shaped pulse has a FWHM of $\sim 20\,ns$ which shows the strong contraction in time compared to the preamp pulse.

Digitized Waveform Recorded with Target C: When a signal crosses the trigger threshold of the T5TEA, Target C digitizes a $128\,ns$ long segment of the storage array that contains the full waveform of the signal. These digital waveforms are transmitted via an optical cable to a computer for long time storage. Target adds an adjustable pedestal voltage (set to $+700\,mV$ here) to the signal in order to shift the signal into the optimal

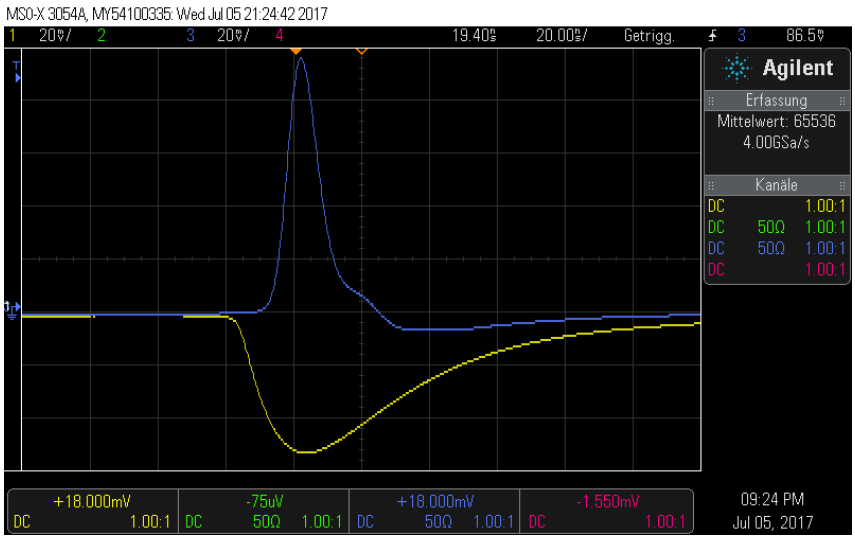

Figure 12 – Oscilloscope picture of the preamp output pulse (yellow) and the pulse after the modified shaper (blue). The depicted signal shape is averaged over 65536 pulses. The small bump after the main peak of the shaper pulse is not a real feature but a trigger artifact caused by the oscilloscope.

working regime of the comparators and to avoid cutting of negative signal values caused by the undershoot. Furthermore, all sampling and storage cells in Target show small differences in their sensitivity to the amplitude of the input signal and in their saturation behavior. Thus, this "raw" Target output signal is rather messy and it is hard to identify the signal waveforms for low signal pulses that are caused by only a few (photon) events in the SiPM. A typical waveform at this stage is shown in Fig. 13. The vertical axis shows the ADC counts of the storage cells and the horizontal axis marks the cell number that corresponds to the time in 1 ns steps. The signal pulse is barely visible in the center of the plot at roughly 70 ns. The negative spikes that occur every 32 ns are caused by the 32nd cells of the sampling array that show a different behavior, as discussed in section 2.4.

Pedestal Calibration: The general offset of Target C and the individual offset of each storage cell is removed from the waveform by a pedestal calibration. As specific storage cells are always supplied by the same sampling cells, offsets due to differences of the sampling cells are also correctly removed by the pedestal calibration. This also takes care of the pedestal offset of the 32nd cells.

For the pedestal calibration the baseline of the inactive SiPM (operated well below breakdown voltage) is used as input signal for the shaper and Target. The digital Target output is measured and thus the offset of each cell is determined. A typical signal shape after pedestal calibration is shown in Fig. 14 on the left. The depicted pulse shows a three p.e. pulse and was produced by illumination with low intensity laser light. The vertical axis is still in units of ADC counts, as no transfer function is applied yet.

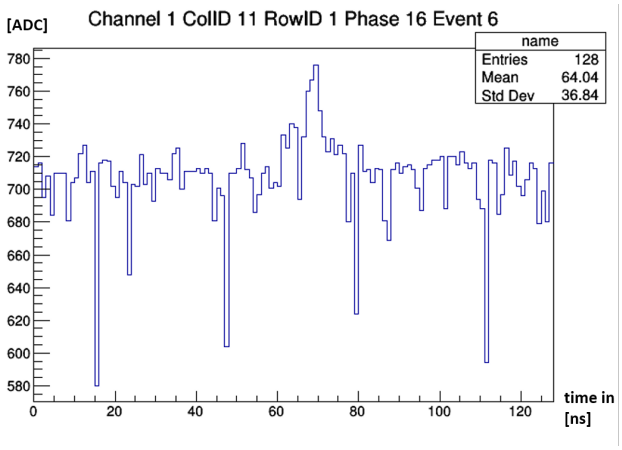

Figure 13 – A digitized but not yet calibrated waveform recorded with Target. The signal pulse is barley visible near the center with the peak at roughly 70 ns. The negatives spikes that occur every 32 ns mark the 32nd cells of the sampling array that have a slightly different performance than the others.

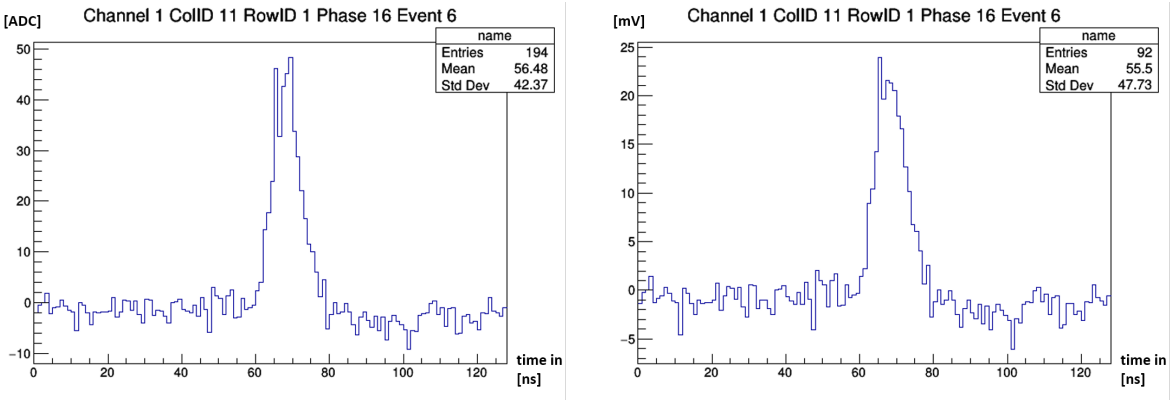

Figure 14 – A waveform measured with Target for low intensity laser light. The headline specifies the input channel, the position in the storage array (CollID,RowID, Phase) and the number of the recorded event during the measurement (Event). This waveform corresponds to a three p.e. pulse. On the left: Pedestal calibrated waveform with the y-axis in ADC counts. On the right: Transfer function calibrated waveform with the y-axis in mV.

Transfer Function: At the final stage of signal calibration, a transfer function (TF) is applied to the pedestal calibrated waveforms. Therefore the software packages TargetDriver, TargetIO and TargetCalib have been used. The TF translates the ADC count value of the Target C output into a voltage value. The transfer function originally only considered the sampling cells but, has been adapted over the course of this thesis to take storage cells into account as well. It determines the ratio of ADC counts to applied signal amplitude for each of the storage and sampling array cells and thus compensates differences between them. A transfer function and pedestal calibrated waveform is shown on the right plot in Fig. 14. The vertical axis is now in mV and represents the amplitude of the signal directly after the preamp.

4 Simulation of the Electronics with LTSpice

A simulation of the signal path from the SiPM to the Target module is performed with the open source program LTSpice from Linear Technologies. SPICE (Simulation Program with Integrated Circuit Emphasis) is a general purpose analog electronic circuit simulator. It is used in integrated circuit and board-level design to check the integrity of circuit designs and to predict circuit behavior [15]. It models the signal with sub nanosecond precision at any point of the SiPM, preamp and shaper. This allows to quickly check the effect that alterations of component values such as capacitors or resistors have on the signal. The simulated signal pulses can be compared to the actual waveforms measured with an oscilloscope or the evaluation board. Furthermore, the saturation behavior of the preamp and shaper can be studied.

Any number of p.e. and the corresponding signal pulses can be simulated by setting the number of fired micro cells in the SiPM model. This ranges from one single photon up to the completely saturated regime (>800 photo events).

A schematic of the complete simulation for the adjusted shaper version is shown in Fig. 15. The red frame marks the SiPM, the green frame the preamp and the blue frame the shaper. The four white components are models of the voltage supplies for the operation amplifiers of the shaper and preamp. The yellow frame denotes the output path of the simulation after the Shaper and the signal offset added by Target. This corresponds to the signal that is stored and digitized with the Target ASIC.

4.1 Comparison of the Simulation with Oscilloscope Measurements

To test the validity of the simulation the simulated pulses are first compared to shaper output pulses measured with the oscilloscope. The SiPM overvoltage is set to +5.9 V (30.4 V applied high voltage) and it is illuminated with laser pulses of different intensities. A comparison of simulated and measured data for the intensities of four p.e. (top left), 14 p.e. (top right), 191 p.e. (bottom left) and ca. 345 p.e. (bottom right) is shown in Fig. 16.

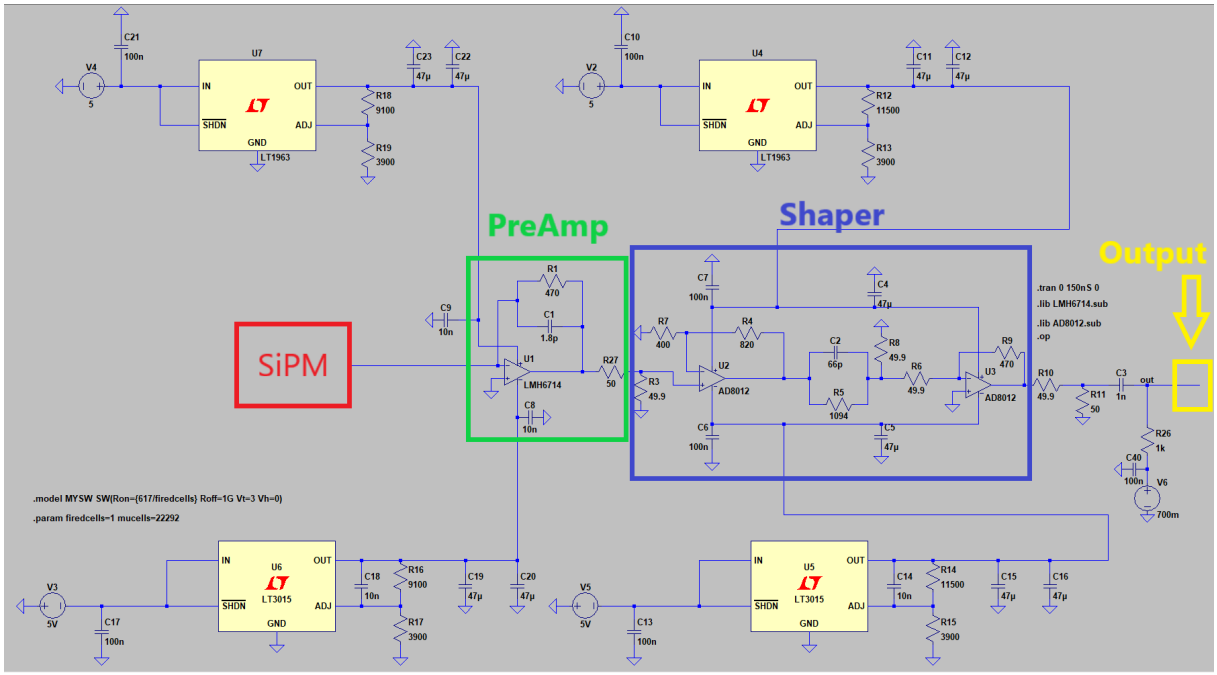

Figure 15 – LTSpice simulation of the signal path of the IceAct; from the SiPM (red) to the preamp (green) and the shaper (blue). The white elements are voltage supplies for the opamps. The 700 mV signal offset voltage is applied near the output. The signal output is on the far right marked in yellow. Due to a confidentiality agreement with SensL it is not possible to show the SiPM model here.

The oscilloscope signals are single, laser induced pulses and their amplitude is subject to the Poisson distributed variances in p.e. per laser pulse (which are discussed in section 6.4.3). Thus, for low amplitudes the measured number of p.e. can deviate significantly from the average number of p.e. expected for this laser intensity. The amplitudes of the two low intensity plots (top) are well within the spread of the Poisson distribution.

The simulated intensities correspond to the mean number of p.e. (including crosstalk) for the corresponding laser intensities. The only exception is the top right event in Fig. 16 for which the mean laser intensity is 11 p.e. but the oscilloscope signal shows a higher amplitude due to the Poisson spread. In this case, the simulated pulse is adjusted to 14 p.e. to match the signal amplitude and show the similarity in pulse shape more clearly.

These measurements with the oscilloscope were performed at the beginning of the illuminated measurements in order to assess a laser intensity that could be used as a starting point for the measurements with Target. The SiPM has been removed and reinstalled in the laser box (described in section 6.3) between the oscilloscope measurements and all other measurements with Target. The laser intensity strongly depends on the exact position of the SiPM in the test box. Apparently, the SiPM was positioned a little farther from the laser source for the oscilloscope measurements and the laser intensity at a given setting is thus slightly smaller than for later measurements with Target. This is evident from the two plots on the bottom of Fig. 16 as the oscilloscope signal is smaller in amplitude than the simulated signal for the 191 p.e. plot. Furthermore, the simulated signal in

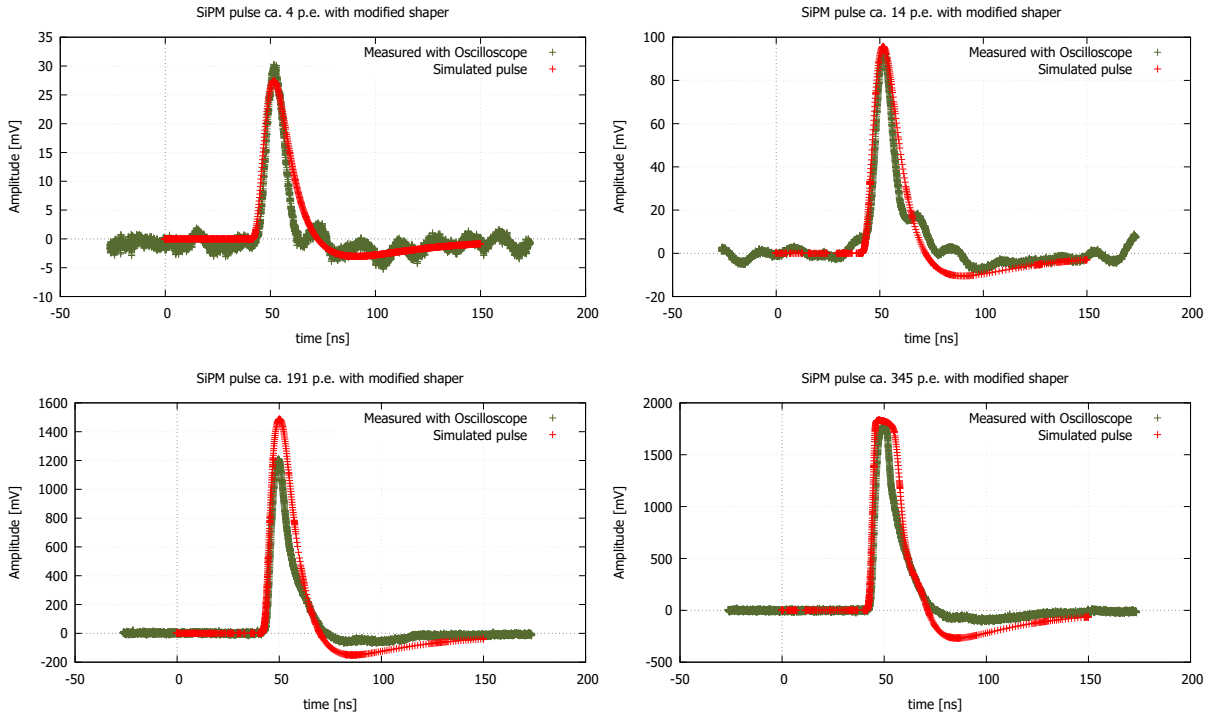

Figure 16 – Comparison of simulated pulses (red) and pulses measured with the oscilloscope (green) after the modified shaper. Top left: a small pulse with an amplitude of four p.e. that matches the simulated pulse closely. Top right: A medium height pulse of 14 p.e. that is slightly above the expected average of 11.23 photon events. Bottom left: A larger pulse with an amplitude of $\sim$ 191 p.e. which is smaller than the simulated pulse. Bottom right: The simulated pulse is already saturated while the oscilloscope signal is still below saturation. Overall the form of simulated and measured pulses matches closely; especially for the rising edges. However, the falling edges of the measured pulses are sharper and the undershoots are smaller than in the simulation.

the 345 p.e. plot (right) already starts to saturate but the oscilloscope measured signal is still (slightly) below saturation.

To compare the signal amplitudes with certainty, the oscilloscope measurements would have to be averaged over a large number of pulses. This would cancel the Poisson fluctuations of the number of p.e. per laser pulse.

For the measured pulses, the falling edge is steeper and the undershoot after the main peak is less pronounced than in the simulations. This indicates that the undershoot is overestimated in the simulation. It is, in fact, smaller than expected for the real measurements. The medium height pulse (14 p.e.) also matches the shape of the simulated pulse quite well, which indicates that the agreement ranges over different pulse heights up to the saturation. The reason for the oscillations in the oscilloscope signal is electronic noise.

4.2 Comparison of the Simulation with Target Measurements

Fully calibrated signals measured with Target are compared to simulated pulses. This allows to isolate effects that are created by the measurement and digitization procedure with Target. Fig. 17 shows a comparison of simulated pulses (red) with Target measured pulses (blue) for different amplitudes while the modified shaper was used.

The signal measured with Target is shifted slightly below the baseline at zero by $\sim 1\,mV$, which is especially visible for the lowest amplitude on the top left. This shift is caused by temperature fluctuations during the pedestal measurements which are discussed in section 6.1.2.

The signals measured with Target all show a lower amplitude than the simulated pulses. This was expected because the transfer function (that converts Target ADC counts to voltage values in mV) recovers the amplitude of the signal after the preamp but before the shaper. Target measures the signal waveform after the shaper but the transfer function then scales the measured amplitude to the amplitude of the signal before the shaper. This is done purposely to compensate the non-linearity of the shaper gain for different signal amplitudes which is discussed in more detail in section 6.1.3. Furthermore, the relevant quantity is not the amplitude but the charge of the signal in units of photon events. A later calibration of charge per p.e. compensates the scaling effect of the transfer function. The simulation, however, yields the signal amplitude after the shaper. The shaper gain (and thus the relative difference in amplitude between simulated and measured signal) is linear over a wide range of signal amplitudes, but decreases near the saturation amplitude of the shaper. This effect is visible in the plots of Fig. 17 where the relative difference in amplitude is much smaller for the 230 p.e. graph (top right) than for the four p.e. graph (top left).

For the non saturated cases, the width of the simulated pulses is larger than that of the measured pulses. The rising edge is in good agreement with the measurement but the falling edge is sharper for the real signal. This effect is present for both, the Target and the oscilloscope measured signals, which indicates that it is a real effect of the signal and the simulation does not reproduce the falling edge correctly.

The two pulses on the bottom of Fig. 17 are at the beginning of saturation (left) and at the fully saturated state (right) and show a fixed difference in amplitude of $\sim 200\,mV$. This is expected, because the simulation yields the maximum amplitude after the shaper, which is $\sim 1800\,mV$. The maximum amplitude measured with Target, however, corresponds to the amplitude of the preamp output signal and is at $\sim 1600\,mV$.

As discussed in section 4.3, the simulation predicts the maximum output amplitude of the preamp to be at $\sim 1425\,mV$. The difference between the maximum amplitude of the simulated preamp and the maximum amplitude that can be reconstructed with the transfer function is probably due to effects of the artificial preamp signal used to generate the TF data. The artificial preamp signal does not saturate and thus affects the maximum input amplitude for the saturation of the transfer function.

The bottom right graph in Fig 17 depicts a fully saturated pulse at the highest measured light intensity of 1580 photon events. The tail of the pulses show strong discrepancies

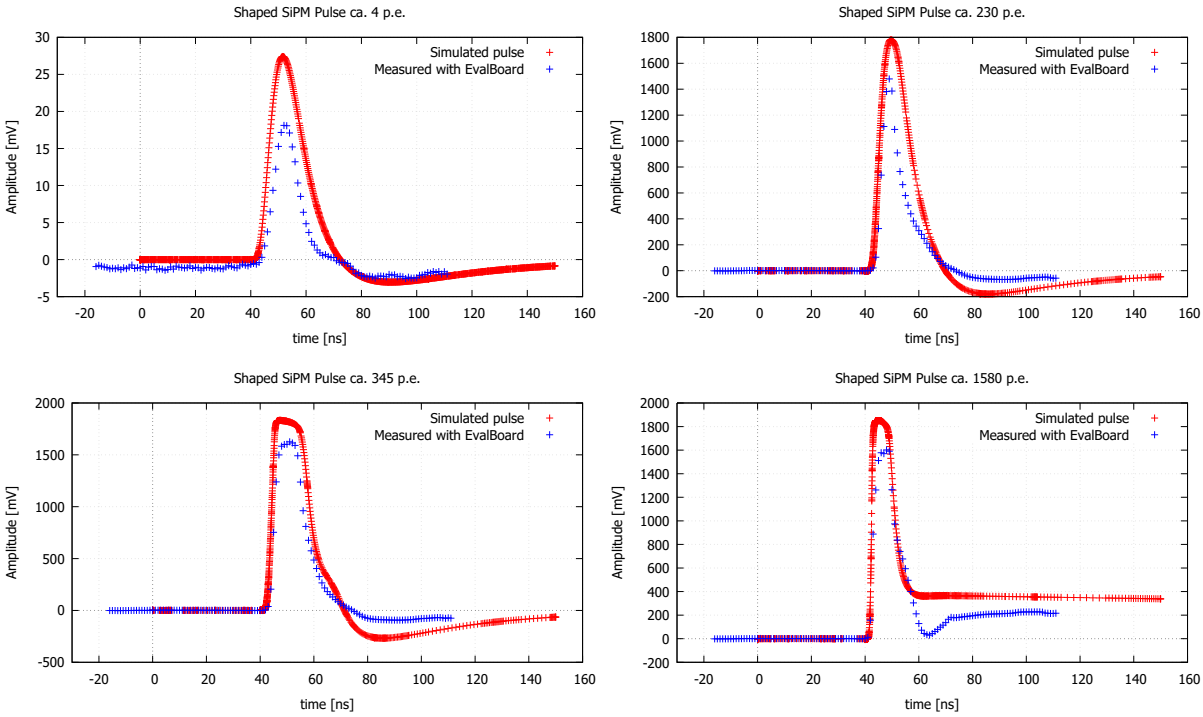

trigger

Figure 17 – Comparison of simulated signal pulses after the shaper (red) and pulses measured with Target (blue). The measured pulses are averaged over 100 events to compensate individual fluctuations.

between the measured and the simulated pulse. The tail is produced by the saturation of the preamp/shaper as is discussed in section 4.3. The simulation predicts a smooth transition of the peak into a long tail of constant height. The measurement, however, shows a sharp drop directly after the peak and then a climb to a relatively constant tail. This sharp drop cannot be reproduced by the simulation. An oscilloscope measurement of a saturated pulse was taken in the course of the linearity measurement of the shaper (section 6.3.3) and is depicted in Fig. 39. It does show this dip after the main pulse as well, which strongly indicates that it is a real feature of the electronics and is not caused by Target. Furthermore, it shows that the saturation amplitude of the signal after the real shaper is indeed at $\sim 1800\ mV$, as predicted by the simulation.

A possible reason why the simulation does not correctly reproduce the tail of the saturated pulse, is that it assumes idealized electrical components. The real components, however, have tolerances that can alter the exact behavior of the signal. Furthermore, the idealized models of the opamps used in the simulation do not take signal distortion (or noise) into account.

This problem has been partly engaged by modeling the voltage supplies in detail to reproduce a more realistic behavior of the supply voltage over the course of a signal pulse and those detailed models have already been used to produce the simulation results in this thesis. A simulation with more realistic models of the opamps (that include signal distortion) is possible, but considerably more complex.

A possible next step to improve the simulation would be to exclude the effects of tolerances of the electronic components (e.g. capacitors and resistors) that are used for the measurement setup. Therefor their exact values would have to be measured and implemented into the simulation.

Nevertheless, the simulation already reproduces many of the main features of the signal pulse and can be used to quickly check the effects that a change of (the value of) the electrical components or alterations of the measurement parameters (overvoltage, number of p.e., supply voltage, etc.) will have on the signal.

4.3 Saturation Behavior of the Components

The simulation allows to check the saturation behavior of the preamp and the shaper. Therefore, different numbers of fired cells are simulated and the amplitude of the signal is observed at four different points:

- The preamp output (blue)
- The pole zero cancellation:
  - Shaping resistor R5 in Fig. 15 (orange)
  - Shaping capacitor C2 in Fig. 15 (red)
- The shaper output (green)

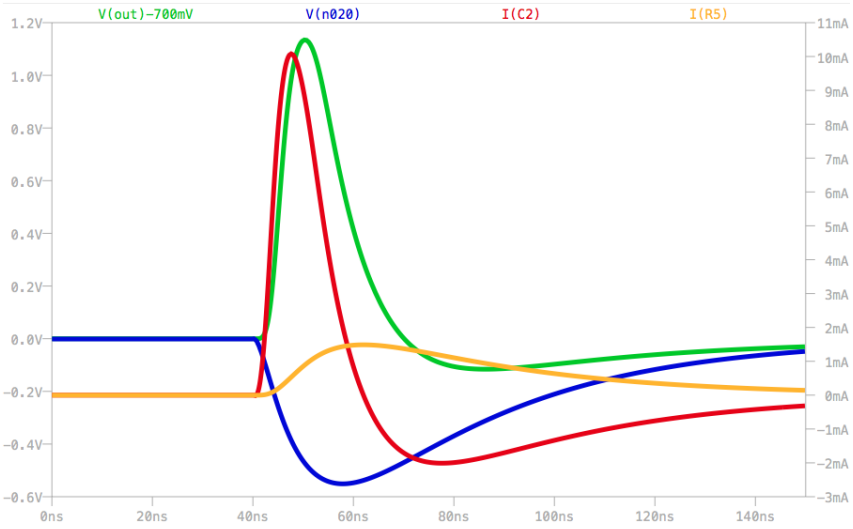

Figure 18 – LTSpice plot of the signal amplitudes over the simulation time at different points in the data path. The blue line marks the preamp output signal. The green line is the shaper output signal. They are measured in [V] given by the left axis. The capacitor (red) and resistor (orange) together form the pole zero cancellation that is responsible for the signal shaping. They are measured in [mA] given by the right axis.

The shape and amplitude of the signal at each of these points is illustrated in Fig. 18, which shows the amplitudes for a non saturated pulse (150 p.e.). The capacitor (red) reacts on the derivative of the preamp output signal (blue) and creates the sharp edges of the output pulse (green). The resistor (orange) that is parallel to the capacitor allows a current that is proportional (but inverted) to the preamp signal. Together, the capacitor and resistor form a pole zero cancellation that is responsible for the shaping of the signal. The resistor current acts against the undershoot created by the capacitor and in an ideal case would negate it completely. The resistor and capacitor current are measured in [mA]; the preamp and shaper voltage is measured in [V].

For higher amplitudes the signal begins to saturate, and with the simulation it is possible to examine which components saturate first and how they affect each other. Therefore, the amount of fired cells is increased in several steps and the signal amplitude at the four, above mentioned points is observed. A mildly saturated signal pulse of 310 fired cells (p.e.) is shown in Fig. 19 on the left. The preamp signal (blue) is not yet saturated but the shaper output (green) already is, which is evident in its flattened, plateau like peak. Thus, the shaper saturates before the preamp.

On the right side of Fig. 19 the shaper output signal (green) is strongly saturated, which is indicated by the long, plateau like tail after the main peak. At this intensity the preamp also saturates (flat part in the blue pulse) at $\sim 1425\,mV$. During the time of saturation the amplitude of the preamp signal does not change and thus there is no current flow through the capacitor (red). This is marked by the flat part of the red curve directly after the peak. The current through the resistor is also constant during this time. In sum, this produces the elongated, plateau like tail of the shaper output pulse. When

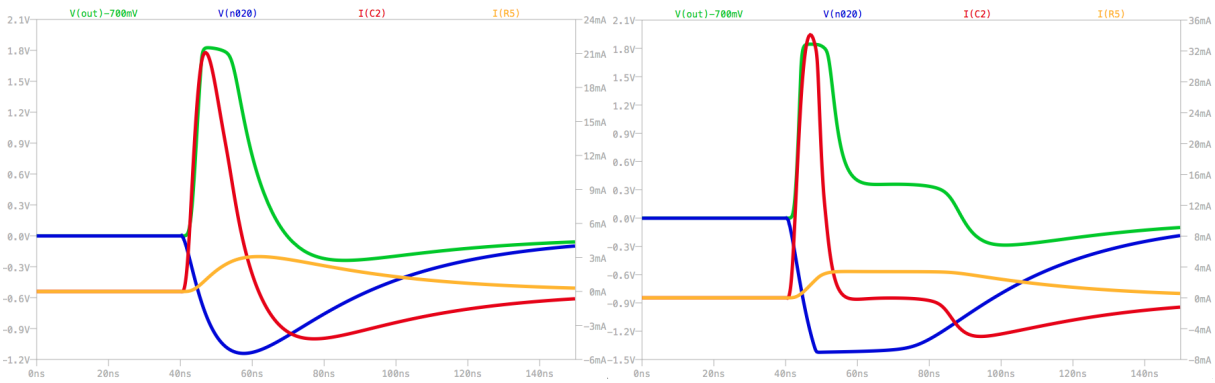

Figure 19 – Left: LTSpice plot of a mildly saturated signal pulse (310 p.e.). The preamp signal (blue) is not yet saturated but the shaper (green) already is. Right: A fully saturated pulse (500 p.e.). At this intensity the preamp saturates too.

the preamp leaves saturation the capacitor generates a negative current that produces a small undershoot after the plateau like tail that is in part compensated by the slowly declining resistor current. This model explains the saturation behavior of the electronics well. However, it does not reproduce the sharp dip in the signal directly after the peak, as seen with Target in Fig. 17 in the bottom graph.

5 Characterization of the Electronics

The next sections (5 and 6) describe the measurements and analysis performed during this thesis. They are arranged roughly in chronological order and the methods and settings that were used have been developed and refined over time.

During the first months of this thesis the electronics (SiPM, shaper and preamp) were characterized with an oscilloscope to gain a precise understanding of how the signal looks at each step before the evaluation board. The measurements in this section were taken for SiPM dark counts without illumination. The oscilloscope measurements on illuminated SiPM signals that are shown in section 4 were taken at a later time.

The dark count measurements were also done to get familiar with the setup and to provide a reference to the measurements with the evaluation board. An InfiniiVision MSO-X 3054A oscilloscope from Aglient Technologies with500 MHz bandwidth and 4 GSa/s (in two channel mode) was used. The measurements with the oscilloscope are more precise than with Target although it features only a 8 bit resolution whereas Target features a 12 bit resolution. This is, because the dynamic range of the oscilloscope is adjustable to the height of the measured pulses, whereas the dynamic range of Target is fixed to an interval of 2.5 V, as it must cover all signal amplitudes. Furthermore, the oscilloscope has a higher sampling rate, is fully calibrated and uses components with a smaller tolerance. Thus, the measurements with the scope are closer to the actual signal, as delivered by the SiPM, preamp and shaper.

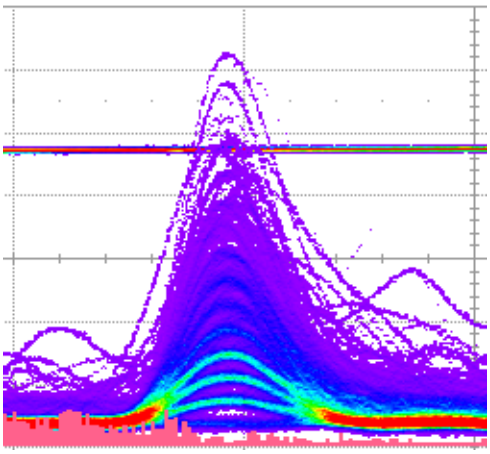

Figure 20 – An Oscilloscope screenshot of the SiPM signal after the modified shaper which shows overlapping pulses of different amplitudes. The strong lines mark the signal amplitude caused by integer numbers of p.e., the fainter lines in between are due to signal noise. The count rate decreases with higher amplitude.

The SiPM produces dark counts with a temperature dependent rate. Due to crosstalk between the micro cells (see section 2.2) each dark count can be counted as two or more p.e. with decreasing probability. By measuring SiPM dark counts with an oscilloscope, this becomes apparent as different pulse heights overlap with a regular gap in between them. This is shown in Fig. 20. The more prominent curves mark pulses for integer numbers of p.e. and the fainter lines between them are fluctuations in the pulse height due to electronic noise and SiPM excess noise.

A p.e.is defined here as the signal produced by one fired micro cell, regardless of its origin. It may be produced by a primary incident photon, a dark count or crosstalk. If a micro cell is fired because of an primary (laser- or shower induced) photon, the term "incident photon" is used for specification.

5.1 Trigger Rate Scan

By gradually increasing the trigger threshold and counting the trigger rate, a trigger rate scan of the dark count signal can be measured. The trigger rate scan (TRS) falls monotonously because the probability of a (dark count induced) p.e. to produce more p.e. via crosstalk is smaller than one, and thus higher pulses are less likely than smaller ones. An example of such a trigger rate scan, measured for the modified shaper, with an overvoltage of $5.75\,V$ is shown in Fig. 21.

The high peak to the very left of the spectrum is caused by the baseline, because for very low trigger thresholds random fluctuations of the baseline lead to a count. The sections with steeper slope appear every time the trigger threshold crosses the pulse with an integer number of photon events. The steep decline at roughly $6\,mV$ e.g. marks the transition from signals caused by at least one p.e. to signals caused by at least two. The more shallow sections mark the region in between these transitions.

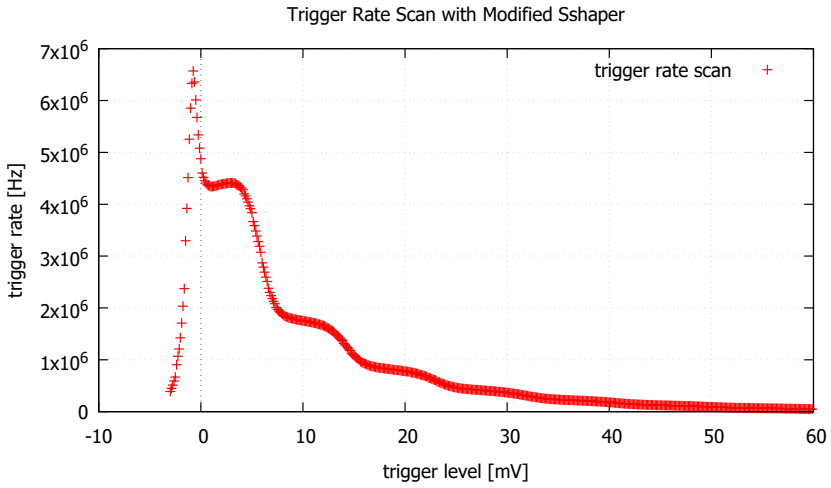

Figure 21 – Trigger rate scan with the modified shaper. The horizontal axis denotes the trigger threshold and the vertical axis the frequency at which dark counts above this threshold are registered. The high peak on the left represents the baseline. The sections with steep slopes mark the amplitude of pulses with integer numbers of p.e.; the plateau like features mark the intervals between them.

5.2 Gain Factor

The gain factor determines the increase in signal amplitude per photon event. It depends on the overvoltage that is applied to the SiPM but also on the amplification factor and exact design of the preamp and the shaper.

It is possible to determine the gain factor of the electronics (including SiPM, preamp and shaper) from the TRS by applying the derivative, which was taken numerically. Every time the trigger threshold crosses a steep section in the TRS, the derivative shows a peak. An example of this (inverted) derivative is shown for the standard shaper at an SiPM overvoltage of $6.75\,V$ in Fig. 22. The pedestal peak (far left) marks the baseline, the next peaks each mark an increasing, integer number of photon events. The derivative of the TRS is similar to a pulse height spectrum, but has the advantage that a large statistic can be acquired in a short time, even from dark counts.

The distance between two adjacent peaks marks the difference in amplitude between two signal pulses that differ by one photon event. By fitting the peak position of two neighboring peaks one can determine the gain per p.e. in the SiPM. This method was used to determine the gain factor of the signal after the preamp and after the two versions of the shaper for different overvoltages

As the overvoltage of a SiPM increases, the number of secondary electrons that are created in an avalanche (and thus the gain per p.e.) increases linearly. The applied overvoltages ranged from $\sim 3\,V$ to $7.5\,V$ in steps of $0.25\,V$. To gain better statistics the first three peaks (excluding the pedestal peak of the baseline) have been fitted and the average distance between two neighboring peaks was determined. All measurements were taken at a constant temperature of $20°\,C$. With decreasing overvoltage the rate of dark counts

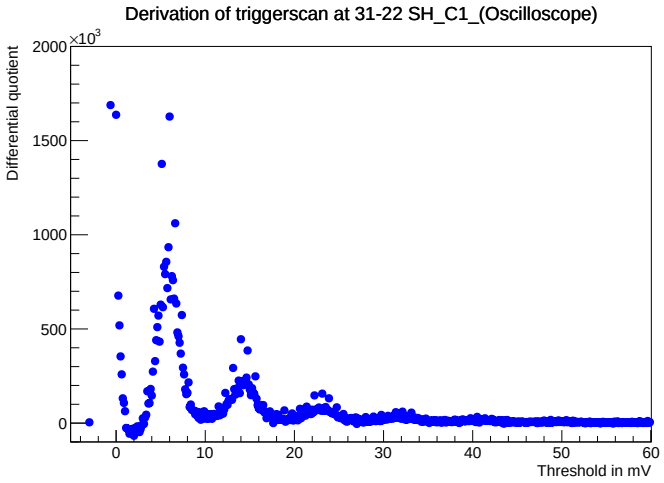

Figure 22 – Inverted derivative of the TRS scan for the standard shaper at a SiPM overvoltage of $5.75\,V$. The baseline peak is visible slightly left of the zero on the horizontal axis. The next peak (at roughly 6 mV) corresponds to one p.e., the second to two etc.

and thus the peaks in the derivative become smaller until they are no longer recognizable. Thus, the lowest overvoltages that have been taken into account are $3.5\,V$ for the modified shaper, $3.75\,V$ for the unmodified shaper and $3\,V$ for the preamp alone.

The gain is assumed to grow linear with increasing overvoltage and thus a linear fit was performed to the three data sets, which is shown for the two shaper versions in Fig. 23. From the slope of the fit the gain per applied overvoltage was determined. The values are shown in Tab. 1.

	gain [mV/V]
preamp	0.66
std. shaper	0.74
mod shaper	1.41

Table 1 – Increase of the gain per overvoltage for the preamp on its own and in combination with the standard CHEC shaper version or the modified shaper version.

The gain per overvoltage of the modified shaper is roughly a factor of two higher than that of the standard version. This allows a better resolution for low intensity light, which causes only a few p.e., because the differences in signal amplitude and pulse area per p.e. are greater. However, this comes at the cost of a smaller dynamic range of the readout electronics, as saturation is caused by a lower number of detected events.

Furthermore, this relation of change of gain per overvoltage can be used to stabilize the gain against temperature changes in the IceAct camera. The breakdown voltage is temperature dependent and therefore the gain changes with temperature. This can be compensated by changing the applied high voltage accordingly.

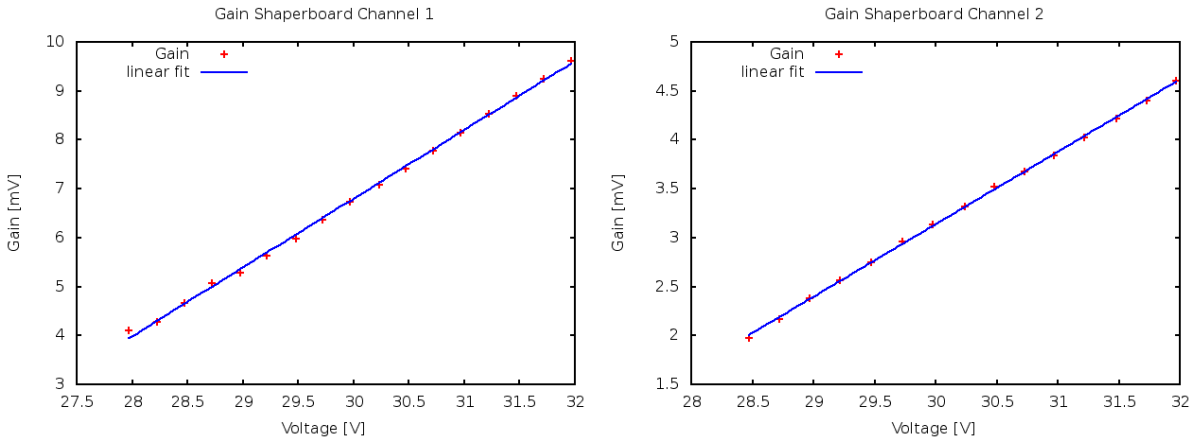

Figure 23 – Gain of the two shaper versions over applied SiPM voltage. The blue line is a linear fit that matches the data very well in both cases. Left: Gain of the modified shaper. Right: Gain of the standard version. The gain of the modified version is higher than that of the standard version by a factor of ~ 2.

5.3 Charge Measurements via Pulse Area

Measuring the area underneath a signal pulse is the best method to determine the number of detected photons/fired micro cells of the SiPM. It is better suited and more precise than the using the amplitude of the signal, because the whole signal pulse is considered and not only the single value of the maximal amplitude. Thus, signal fluctuations or measurement errors can cancel themselves out to some degree.

The SiPM emits a current pulse over a certain time. The area underneath that pulse has the unit of charge and it is directly proportional to the number of fired micro cells. As the preamp is a transimpedance amplifier, the signal is changed from a current signal to a voltage signal, but the area underneath the signal pulse is transformed proportionally and still contains the information about the number of photon events. It is thus still called the "charge" of the signal.

The area of SiPM dark count signals was measured with the oscilloscope for both versions of the shaper and for different overvoltages of the SiPM from $+2\,V$ to $+6.5\,V$ in steps of $0.25\,V$. For each voltage 40000 events have been recorded and their area was plotted in a histogram. An exemplary area spectrum is shown in Fig. 24. The biggest peak to the left is the pedestal; the peaks next to it are caused by an increasing number of photon events. The peaks are Gaussian in shape and their width is due to noise of the electronics and the SiPM excess noise. The better one can separate the individual peaks, the easier it is to determine how many micro cells of the SiPM fired, which is related to the number of incident photons. The peaks become more distinguishable if they are farther away from one another (higher gain) or their width is smaller (less noise). This measurement is done in order to provide a reference for the later charge resolution measurement with Target.

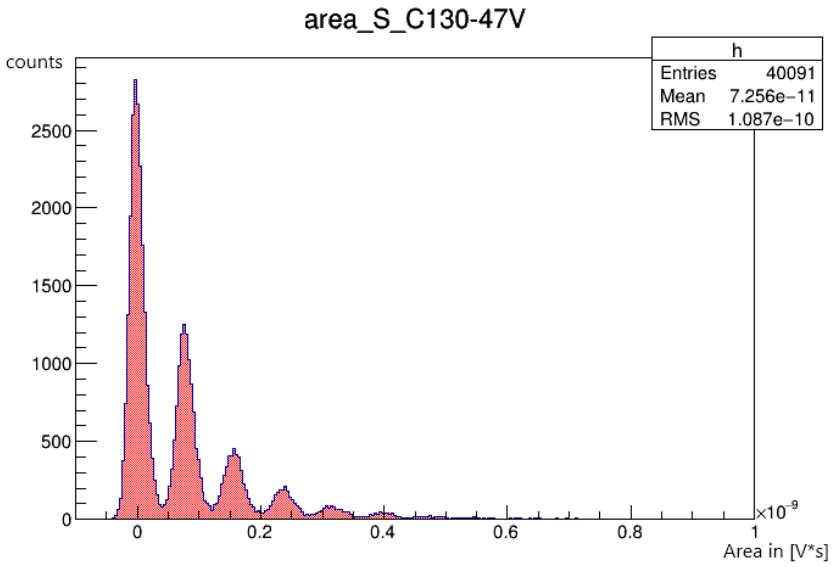

Figure 24 – Area spectrum of SiPM dark counts with the modified shaper and an overvoltage of $5\,V$; measured with the oscilloscope. The horizontal axis is the area in units of V*ns; the vertical axis denotes the number of counts per area bin. The biggest peak on the left is the pedestal (zero p.e.), the peak next to it denotes one p.e., the next two etc. The peaks are of Gaussian shape and their width is determined by the noise of the electronics and the SiPM.

6 Measurements with Target C Evaluation Board

The output of the shaper is now connected to the first input channel of the evaluation board instead of the oscilloscope. The other 15 input channels are unconnected (terminated with 50 Ω to ground) and can be used for a common mode correction of the signal.

6.1 Calibration and Transfer Function

To gain useful data from the evaluation board it has to be calibrated first. All storage cells need to be pedestal calibrated for the general offset and their individual offset. Furthermore, each individual sampling and storage cell's exact conversion factor from internal ADC counts to voltage must be determined via a transfer function. As the long time storage array of 16384 cells is not currently needed for the purpose of the IceAct, only a quarter of the storage buffer of the evaluation board is used throughout this thesis. The remaining storage cells are simply ignored/skipped for writing and reading by the Target firmware.

6.1.1 Pedestal Calibration

For the pedestal calibration the high voltage supply of the SiPM is set to $+5\,V$ (which is $19.5\,V$ below breakdown voltage) to assure that no dark count events take place and it only outputs its baseline. The high voltage supply is not completely turned off, because the electronic noise level of the SiPM is different for zero applied high voltage. The noise depends on the load, but should be constant for all non zero high voltages.

The output of the SiPM and preamp is connected to the shaper and then to the evaluation board. Separate pedestals are taken for the two shaper versions. The trigger mode of the board is set to "external" and a trigger signal with $3\,kHz$ is supplied by a waveform generator. The external trigger rate is not a multiple of the $4096\,ns$ long storage buffer and the internal clocks of the waveform generator and Target are not synchronized, which ensures that all storage cells are used with equal probability. As only the baseline is applied and no signal pulses occur within the digitized waveform, all 128 data points of every waveform are used as pedestal values for the according storage cells. A pedestal measurement takes $\sim 4 \cdot 10^6$ data points, so that every storage cell has an average of roughly a thousand pedestal values as statistic.

The mean value is calculated for each cell and stored in a pedestal file. It can later be used to calibrate data files of measured events by subtracting the mean pedestal value of each cell. This calibration is performed by the program TargetCalib, which is used for the pedestal and transfer function calibration of Target measurements and was written at the University of Oxford.

6.1.2 Common Mode Correction and Temperature Dependency

Only channel 1 of the 16 input channels of the evaluation board contains an SiPM signal. Channel 0 is not working, but the other 14 channels can be used for a common mode correction. A trigger event leads to the digitization of all 16 channels and their digitized waveforms are packaged and send to a computer. Thus, the information of all channels at the time of a trigger event is available and can be used to correct disturbances of the signal that apply to all channels, such as from the switched dc-dc converters of the FPGA. The common mode correction is performed by subtracting the mean value of the 14 free channels from the signal channel for each time bin of the waveform during the analysis.

This can also be used to correct for a common offset, but it is not equal to a pedestal calibration because the differences of individual storage cells are not taken into account. A huge benefit of the common mode correction, is that a temperature induced shift of the baseline can be compensated by it. It was found out during this thesis that the evaluation board is heating up significantly over the first one to two minutes of a measurement run, even though a continuously running fan is placed directly next to the ASICs and FPGA. This leads to a shift of the signal baseline and thus to a shift of the amplitude and area over the course of a measurement. As typical measurement runs take one or two minutes, the temperature shifts are severely influencing the outcome of the measurements. Furthermore, between measurements, the temperature drops down

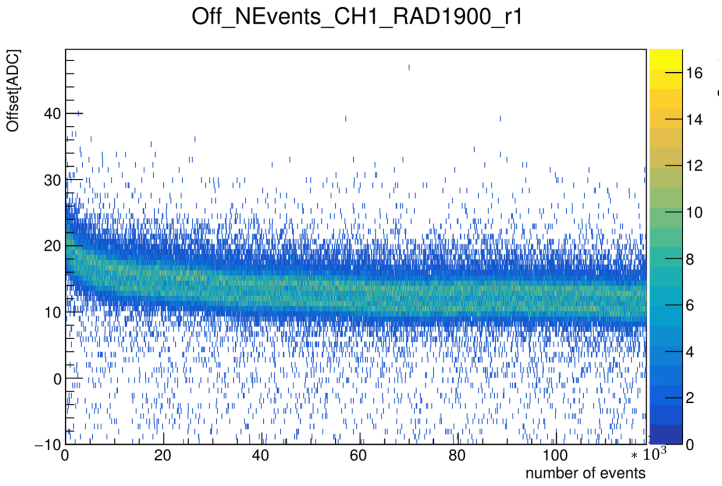

Figure 25 – 2D histogram of signal offset over event number measured with Target for illumination with low intensity laser light. The color scheme marks the density of the points and the greenish band signifies the majority of all events. The measurement was taken over the time of one minute with a trigger rate of $\sim 2\,kHz$. The offset shifts strongly downwards for the first 10 to 20 seconds (20 to 40 thousand events) and experiences a slower decay over the remaining time.

in a timescale of minutes and thus the temperature shifts affects all measurements. The common mode correction compensates these shifts and makes the measurement results much more precise. It is, however, advised to let the evaluation board (or Target module) heat up with a dummy measurement for at least two minutes before starting an actual measurement.

An example of this baseline shift is shown in Fig. 25. It depicts a 2D histogram of the signal offset over the number of recorded events (and thus the measurement time). The measurement was taken under illumination with low intensity laser light over one minute and with a trigger rate of $\sim 2\,kHz$. A clear shift of the offset is visible in the first part off the graph up to 20 to 40 thousand events corresponding to 10 to 20 seconds of measurement time. After that, the decay becomes slower and asymptotically vanishes as the temperature becomes stable.

6.1.3 Transfer Function

The transfer function translates Target internal ADC counts into voltage values and corrects for differences between the individual Target C storage cells. As specific storage cells are always supplied by the same sampling cells, the storage cell based TF accounts for any differences in the sampling cells as well.

Due to tolerances of the capacitors of the sampling and storage cells, individual cells react differently (with different amplitudes in ADC counts) to the same signal input. Furthermore, each cell reaches its individual saturation for slightly different signal amplitudes. To digitize the voltage value of a storage capacitor it is compared with a steadily growing

voltage ramp applied by a Wilkinson ADC. When the voltages are equal, the value of a counter that started at the beginning of the ramp is written into a shift out register and yields the digital value of the capacitor voltage in the form of ADC counts.

The transfer function is generated by applying standardized, SiPM-like pulses of exactly known amplitude to the shaper via a KEYSIGHT 33600A Series waveform generator and measuring the ADC counts of the output signal of Target.

First, however, another pedestal calibration has to be performed, to compensate temperature shifts that may have occurred before the measurement of the TF events. Therefore the output of the waveform generator is switched of, so that the wavegenerator only outputs its baseline. All other steps of the pedestal calibration of the TF data are performed the exact same way as the pedestal calibration of the SiPM data.

The artificial preamp output signal was designed according to the real output signal of the preamp (connected to the SiPM at 30 V) that was measured with the oscilloscope for SiPM dark counts. The preamp pulse measured with the oscilloscope is shown in Fig. 26 on the left; the waveform of the artificial pulse is shown in on the right.

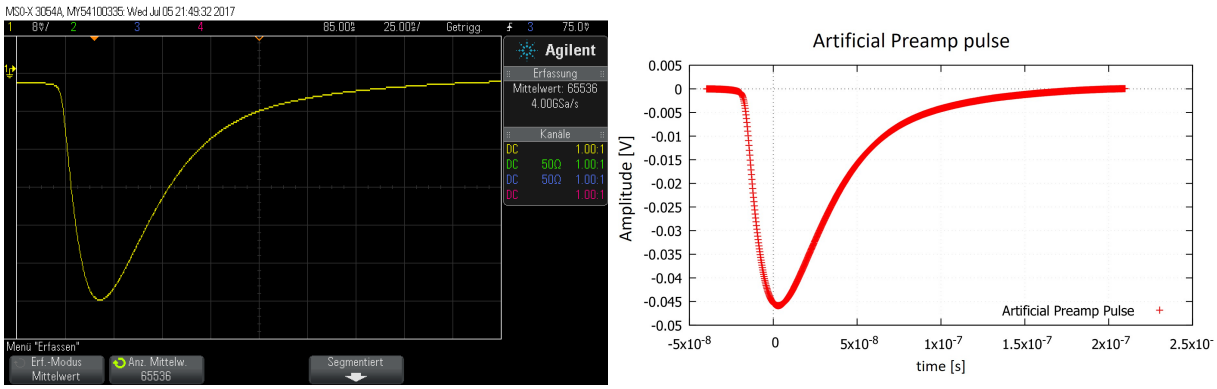

Figure 26 – On the left: An Oscilloscope measurement of the dark count SiPM and preamp output pulse (averaged over 65536 pulses) with an SiPM voltage of 30 V from which the artificial preamp pulse is modeled. On the right: The artificial preamp output pulse for the waveform generator. It is used as reference input to the shaper and evaluation board in order to generate the transfer function.

To create the necessary data for the TF the artificial preamp pulses are scaled in their amplitude from $-100\,mV$ to $+2500\,mV$ in steps of $4\,mV$ and are applied to the evaluation board via the shaper. The negative input amplitudes are necessary to handle the pulse undershoot that is created by the shaper. Transfer functions have been created for both shaper versions separately. The trigger was set to external and provided by the wavegenerator; in sync with the signal pulses. For each input amplitude $\sim 1.2 \cdot 10^5$ events were recorded and stored as digital waveforms. Then the pedestal calibration was applied to all of them.

In a next step, the amplitude of the signal peak in each event for each input amplitude has to be determined. This is done by the C++ script "generate_ac_tf_neg.cc" that was written by David Jankowsky at ECAP for the calibration of the Target modules for the

CHEC camera. It has been modified to also accept negative input values that are needed for the IceAct. For CHEC, the undershoot of the pulse is used as negative value for the TF. The undershoot of the IceAct signal is smaller, however, and is not so well suited for this task.

The script first determines the exact position of a signal peak in the waveform for each event. The signal position should be constant, as the trigger delay is constant, but the trigger point is only determined with a precision of $1\,ns$ and there is a jitter of $\sim 350\,ps$ between the trigger out and the signal out of the waveform generator. Thus small fluctuations are possible and it is necessary to determine the peak position exactly in order to measure the full amplitude of the peak. Even a delay of one time bin can decrease the amplitude and the transfer function would underestimate the output amplitude systematically. The performed fit is a double landau fit; one positive for the main pulse, and a second negative one for the negative tail. The double Landau fit is optimized for the waveforms for CHEC, but works very well for the IceAct setup as well. Plots of this fit are shown exemplary for a low, medium and high intensity pulse in Fig. 27. The fits match the pulse quite well for non saturated signals (left and mid). For saturated signals, the peak of the pulse is cut off due to saturation of the readout electronics and a plateau is left that marks the maximum amplitude of the corresponding sampling/storage cells. The double Landau fit deviates from the measured pulses for these saturated signals but the peak position of the fit still lies above the plateau of the signal pulse. Thus even an error in the time bin leads only to a small error of the amplitude as the plateau is flat. The ADC count of the cell that corresponds to the peak position of the fit is read out and gives information about the saturation amplitude of this cell.

The mean value of all events for each input voltage is taken and stored in a file (TF_file). The transfer function in this TF file is plotted for all cells and a graph of it is shown in Fig. 28 for the modified shaper version (left) and the standard shaper version (right).

The transfer function relates the measured ADC counts of the signal after the shaper to the input amplitude of the artificial preamp signal before the shaper. Thus, the pulse height in [mV] that the transfer function delivers represents the amplitude of the preamp signal. To obtain the amplitude of the signal after the shaper (at the Target input), the amplitude of the TF would have to be multiplied by the gain of the shaper. However, the gain of the shaper is not linear over the full range of signal amplitudes, as is discussed in section 6.3.3. Especially near the saturation it deviates strongly from linearity. This effect is absorbed by the transfer function. The ratio of additional ADC counts per additional mV of input amplitude decreases near the saturation. When calculating the amplitude of a real measured signal in mV from the measured ADC counts this change in slope of the TF exactly compensated the non-linearity of the shaper gain.

As described in section 5.2 the gain of the modified shaper is a factor of ~ 2 higher than for the standard version and thus the signal amplitude (for a given artificial preamp input pulse) is twice as high after the shaper. This affects the transfer function. The increase of ADC counts per applied input voltage is twice as high, but the cells also saturate earlier. The saturation of the shaper begins at $\sim 1100\,mV$, which is marked by the change of slope in the transfer function of the modified shaper. At an input voltage of ~ 1500 to

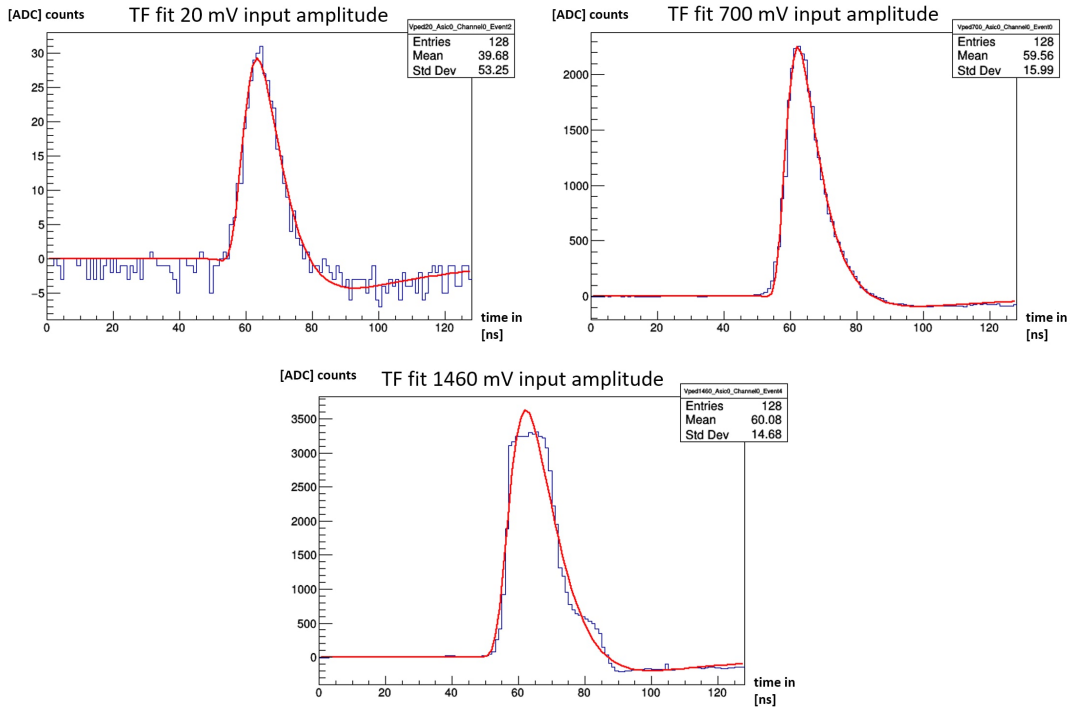

Figure 27 – Double Landau fits on measured events for different amplitudes of the artificial preamp pulse that were used to generate the TF for the modified shaper. The vertical axis is in mV and the horizontal axis in ns. Top left: Small pulse with20 mV input. Top right: High, but not saturated pulse for 700 mV input. Bottom: Well saturated pulse for 1460 mV input. The top of the peak is cut off due to saturation and the fit deviates from the signal.

$\sim$ 1600 mV most cells reach their full saturation. For the standard shaper the saturation only occurs at an artificial preamp pulse amplitude of $\sim 2400\,mV$.

But as is discussed in section 4.3 the real preamp saturates already at $\sim 1425\,mV$. Thus, for any real measurement with the SiPM the preamp cannot deliver more than 1400 mV and the dynamic range between $\sim 1400\,mV$ and $\sim 2400\,mV$ (corresponding to ADC values above 1900) would go unused for the standard shaper. This is one argument to prefer the modified shaper for the IceAct readout electronics.

In both cases, the transfer function reconstructs the amplitude of the (SiPM produced) signal after the preamp from the ADC counts of the Target output.

Finally, the transfer function calibration can be applied to measured data with the program "TargetCalib" that is also used to perform the pedestal calibration.

Throughout this thesis the transfer function was updated several times, as new software versions of TargetCalib became available and previous bugs in it or the script "generate_ac_tf_neg" were fixed. The change with the greatest effect was switching from a sampling cell based transfer function to a storage cell based one. The former only took into account the 64 sampling cells and their differences, while the storage cells were assumed to be uniform in their performance. The storage array is successively filled by the

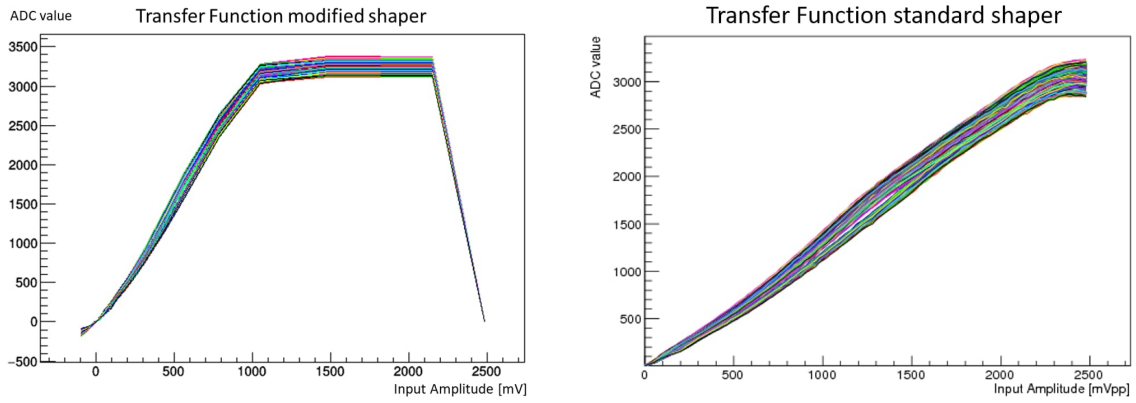

Figure 28 – On the left: Plot of the transfer function for the modified shaper version for every cell. The horizontal axis denotes the amplitude of the artificial preamp input signals. The vertical axis denotes the mean ADC counts that each cell has for this input voltage. The cells are not uniform but show a slightly different slope and different saturation. The saturation of the shaper begins at $\sim 1100\,mV$, which is marked by the change of slope. Most cells reach their full saturation at ~ 1500 to $\sim 1600\,mV$. For the last data point at $2.5\,V$ an error in the plot occurred, but is not relevant for the use of the TF later on. On the right: TF for the standard shaper. The slope is much lower and the cells reach saturation at $\sim 2400\,mV$. Note that due to a bug in the script the automatic plot for this TF failed to include the part for negative voltages. It is, however, included in the TF data file.

sampling cells, so every 64th storage cell is filled by the same sampling cell. In the later versions the individual differences of the storage cells are taken into account, too, and a transfer function is made for every single one of them.

To perform the transfer function calibration, TargetCalib takes only a few input amplitude values and interpolates with a coarse spacing in between them. The used resolution of input amplitudes in TargetCalib was thus much sparser than the measurement (in steps of 4 mV) would allow. This coarse interpolation was found to be too wide to yield transfer functions with optimal precision near the end of the research for this thesis. A new version of TargetCalib that features smaller steps for the TF calibration was under construction at the end of the end of the research phase, but could not be implemented for the measurements. Better performance in the transfer function will improve the charge resolution of the Target module/evaluation board as the signal waveforms can be calibrated more precisely and distortions of the amplitude and pulse area will become smaller.

6.2 Dark Count Measurements

6.2.1 Trigger Rate Scan to Determine the Trigger Threshold in p.e.

The gain of the SiPM was set to $4\,mV$ per p.e. during the first measurements with the evaluation board. This is the same value as is planned to be used for CTA and it offers a good compromise between charge resolution at low intensities and dynamic range. This

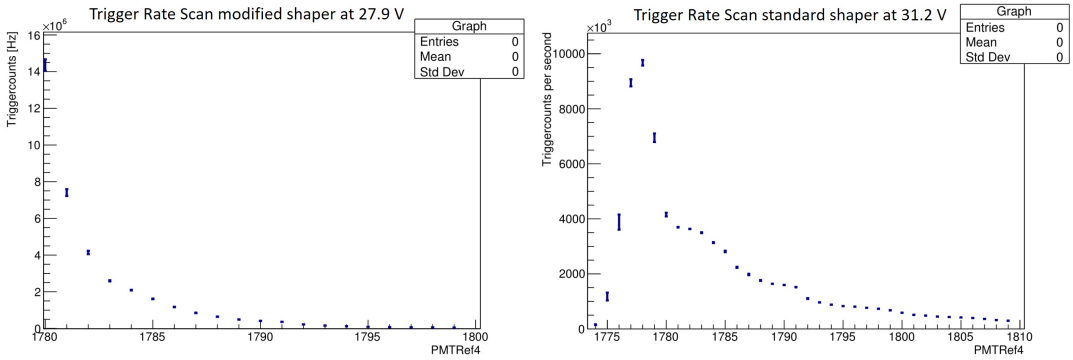

Figure 29 – Trigger rate scan measured with the evaluation board for dark count measurements. On the left: Taken with the modified shaper version with an SiPM voltage of $27.9\,V$ corresponding to a gain of $4\,mV$ per photon event. On the right: Taken with the standard shaper version with a SiPM voltage of$31.2\,V$ also corresponding to a gain of 4 mV per photon event.

corresponds to an SiPM high voltage of $27.9\,V$ for the modified shaper and $31.2\,V$ for the standard CHEC version, as was determined in section 5.2. The pulse height measurements and all measurements with the evaluation board but without illumination of light have been performed with this setting.

The trigger threshold of the evaluation board should be set close to the amplitude of one p.e. (id est $4\,mV$), as the general goal is to find parameters that make individual p.e. peaks visible in the area spectrum so that the charge per p.e. can be determined in the illuminated measurements that are performed later.

Higher thresholds would cut off most of the events produced by a single fired micro cell in the SiPM. Lower thresholds, on the other hand, would trigger on too much noise from the baseline. The trigger threshold of the Target module/evaluation board can be set via the parameters Thresh (fine) and PMTref4 (coarse), as described in section 2.4. In order to determine the desired trigger position near $4\,mV$ a trigger rate scan of dark count signals is performed with the evaluation board. Thresh is set to a value of 1802 and Vped to 1100, which has been found out to be a good value in previous work by Manuel Loos ([14]). PMTref4 is scanned in a range of 1770 to 1820 to increase the trigger threshold. This is done for both shaper versions and is shown in Fig. 29. For the standard shaper (on the right) the spectrum is much clearer and one can easily see the first few steps. The first strong decrease that marks amplitude of one p.e. is at a PMTref4 value of 1785. For the modified shaper the spectrum is harder to read, because there are less dark counts due to the smaller applied voltage to the SiPM. The lower voltage also reduces the cross talk probability and thus further reduces the number of events with more than one photon. Nevertheless, the first steep decrease seems to be also at 1785 PMTref4, which should be the case as the SiPM voltage is adjusted to keep the gain equal for both shaper versions. The PMTref4 value is thus set to 1784 for both shaper versions, so that it is slightly below one photon event.

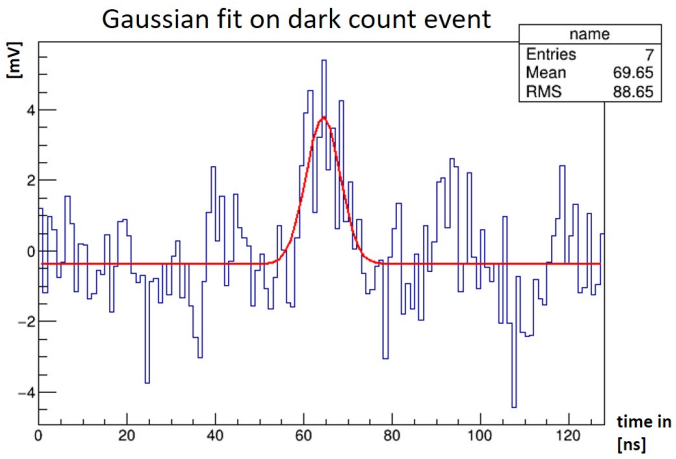

Figure 30 – Gaussian fit on a dark count event measured with Target. An early version of the transfer function was used for all dark count measurements.

6.2.2 Area and Amplitude Measurements

SiPM dark count events are measured for both shaper versions with a gain of $4\,mV$ per p.e. ($27.9\,V$ for the modified shaper and $31.2\,V$ for the standard shaper) with internal trigger mode. The raw events are pedestal calibrated and TF calibrated. The data is then analyzed for all stages of calibration (only pedestal, pedestal+TF and with/without common mode correction). The amplitude, area, offset and the position of the signal peak in waveform are determined and plotted in histograms with the C++ based data analysis program "root".

The waveform of each event is fitted with a Gaussian function that matches the pulse form sufficiently well and is much faster than the double Landau fit used for the transfer function. The trigger delay is set so that the peak of the signal pulse lies in time bin 66 of the waveform. Some waveforms, however, have their peak at $72\,ns$. This delay of $8\,ns$ was caused by a bug in the Target firmware and was fixed later.

Not all waveforms are clearly visible and easily fitable. Sometimes the evaluation board triggered at noise or the waveform is distorted by electronic noise or imperfections in the calibration. To separate the "good" events from the "bad", certain cut criteria were applied to the fit and their effect on the area and amplitude spectrum of a measurement run was analyzed. An example of such a fitted event is shown in Fig. 30. The strong deviations of individual cells is due to the early version of the TF that was used at this stage of the thesis. Furthermore, dark count events have on average a low number of p.e. (one for the example shown in Fig. 30) and thus the signal-to-noise ratio is very low.

The fit is necessary because individual time bins of the waveform (cells) show "runaways" or spikes due to imperfect calibration. If one only took the bin at the position of $66\,ns$ and this bin was to contain a spike, the determined amplitude would be significantly distorted. Fitting the peak can compensate spikes in the waveform, as their effect is mitigated by the neighboring time bins. Furthermore, allowing the fit to vary its peak position from

the expected position can compensate shifts in the position of the peak. The Gaussian fit is not an exact match to the waveform as it cannot reproduce the undershoot after the main peak (which is less pronounced for real data than for simulated data, as is discussed in section 4.2). However, it matches the pulse form produced by the IceAct SensL SiPM quite well and all necessary parameters (especially the position of the peak) are obtained with good precision.

The offset, the peak position (pp) and the event number are stored for every fit. Furthermore, the amplitude of the waveform is determined from the value of the bin that represents the peak position of the fit. To determine the area of each event the values of all bins in the interval of pp-9 to pp+7 are summed up. The borders of the interval are chosen to contain the full extent of the pulse and take into account the sharp falling edge of the pulses measured with the modified shaper. The values that are used here, are only an initial (but well-working) guess, however. The optimal integration window is determined methodically in section 6.4.1 and used from there on. The area underneath the pulse is proportional to the registered number of fired micro cells of the SiPM and the main purpose of the fit is to enable its measurement via the determination of the peak position.

A example of the area spectrum that was created with the dark count measurement is shown in Fig. 31. For both versions of the shaper no finger spectrum with different area peaks is visible, although the trigger threshold was increased to a PMTref4 value of 1786 to exclude more of the baseline events. The mean area was larger for the setup with the standard shaper because the applied voltage to the SiPM was higher, which led to more crosstalk and thus a higher average number of photon events.

Different cut criteria on the position of the peak, its amplitude and its standard deviation have been applied to improve the spectrum, but did not prove successful. An even higher trigger threshold with a PMTref4 value of 1796 was used to select only events with a larger number of p.e. and less noise, but no finger spectrum was visible for any of the shaper versions with this setting, either. This is probably due to the early version of the TF that was used for the dark count measurements and the low crosstalk due to the low SiPM voltage that was applied for the setup with the modified shaper.

To increase the gain and crosstalk, the SiPM voltage for the modified shaper setup was increased from $27.9\,V$ to $31.2\,V$, which more than doubles the gain per p.e. to $\sim 8.6\,mV$. The trigger threshold was set back to a PMTRef4 value of 1786. The overvoltage for the setup with the standard version of the shaper has not been increased, since it was already at a high value of at $31.2\,V$. With this high gain setting and the modified shaper, different p.e. peaks could be resolved in the area spectrum. This is shown in Fig. 32. The data used for this spectrum is only pedestal calibrated and no TF has been applied. The presence of individual area peaks for each number of p.e. shows that the SiPM works as expected and that single photons can be recorded and resolved. It is, however, difficult to achieve this with only dark count signals and was only possible due to the high gain of the modified shaper.

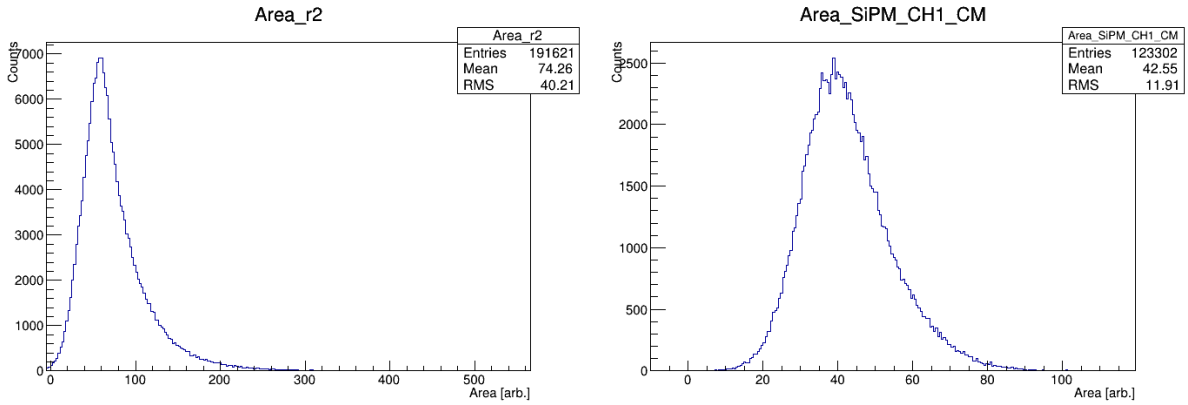

Figure 31 – Area spectrum for SiPM dark counts events for the standard shaper at$31.2\,V$ (left) and the modified shaper at $27.9\,V$ (right). Both spectra are taken with a PMTref4 value of 1786.

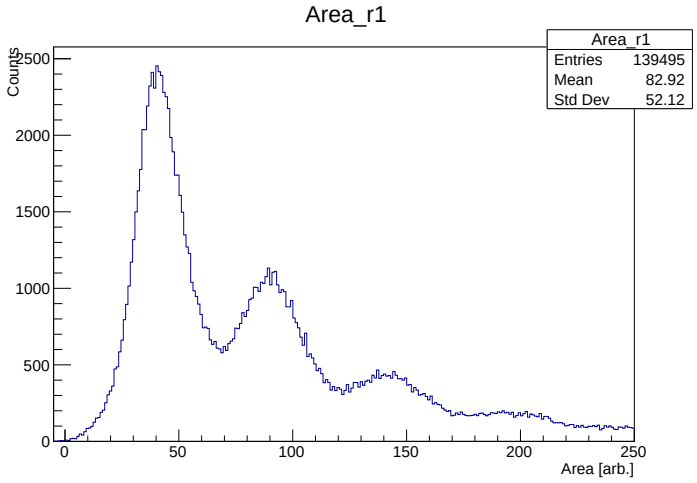

Figure 32 – Dark count area spectrum for the modified shaper at a high gain with an SiPM voltage of 31.2 V. It shows distinct peaks for different numbers of photon events.

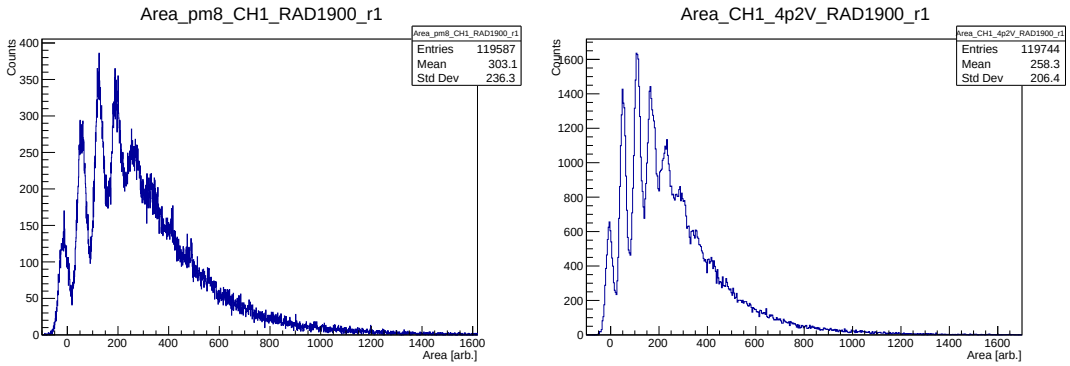

Figure 33 – Comparison of the two area histograms taken with a preamp supply voltage of $4.8\,V$ (left) and $4.2\,V$ (right). The two cases look very similar and this proves that the shaper also works with the Target supply voltage of $4.2\,V$ (at least for low intensities).

6.2.3 Comparison Preamp Supply Voltage 4.8 V and 4.2 V

The preamp has a supply voltage of$4.8\,V$, which was used for all measurements in this thesis. The Target module, however, has a supply voltage of $4.2\,V$. If the preamp can also be supplied by $4.2\,V$, no additional voltage source is needed for operation of the IceAct telescope, which will make the electronics cheaper, more compact and more resilient as fewer components are needed. In a remote environment such as the South Pole this can be a significant advantage. Thus, it is tested if the preamp can also operate with $4.2\,V$ supply voltage. The setup is tested for a SiPM voltage of $30.4\,V$

This was done only as a quick check and not a detailed study. Therefor the area spectrum for illumination of the SiPM with low intensity laser light (mean number of p.e. of ≈ 3) was taken for $4.2\,V$ and $4.8\,V$ preamp supply voltage and the two were compared. Both area histograms contain only pedestal calibrated data and are shown in Fig. 33.

The two histograms are very similar, which is proof that the preamp can work with $4.2\,V$ supply voltage. However, for higher illumination (and saturated pulses) the behavior of the preamp might be different with the lower supply voltage. Especially its saturation voltage might decrease.

6.3 Illumination Measurements

The next step is to illuminate the SiPM and to analyze the performance of the setup when real photons are present.

For the illumination measurements the SiPM was put in a light-tight laser box that is shown in Fig. 34. The box features a pulsed laser with a wavelength of $402.9\,nm$ and a pulse length of max. ~ 3 ns that is designed to simulate Cherenkov light. The intensity of the laser, which can be regulated by a tuneable filter wheel, covers the full dynamic range that the readout electronics can accept up to complete saturation. The intensity is measured by an integrated photo diode. The box is designed to test the performance

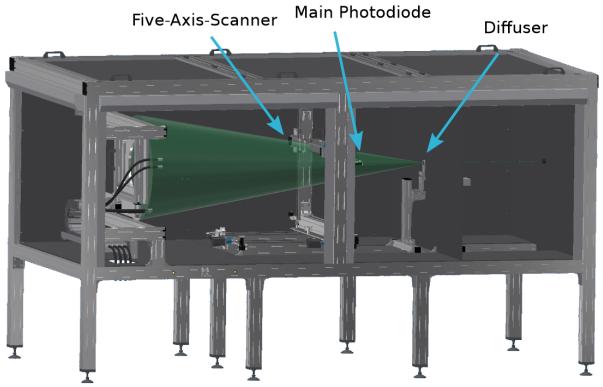

Figure 34 – Schematic of the laser test box used in the illumination experiments. The laser pulse is created on the right and attenuated by a filter wheel before it is distributed at the diffusor. A photodiode measures the intensity of the laser beam. [11]

of the CHEC camera for CTA but is equally well suited to test a single SiPM for IceAct, the full IceAct camera or even the full IceAct telescope as it will fit into the box. The laser beam is distributed by a diffusor to homogeneously illuminate a surface on the left of the box that is designed to map the CHEC camera. The SiPM for the IceAct is placed next to the Camera mount on this part of the box and is thus homogeneously lit. The intensity of the laser at the SiPM is determined later in units of registered photons. The conversion is performed via the ratio of the internal photo diode current (in the box) to the number of p.e. recorded with the SiPM. Thus, geometric factors for the intensity of the laser at the SiPM can be neglected as long as the distance of the SiPM to the diffusor is constant during all experiments.

For low intensity laser light the photons in a laser pulse are Poisson distributed and the statistical error on the photon number n is given by $\sqrt{n}$. For higher intensities ($\gtrsim 100$ p.e.) the distribution is Gaussian like. Thus, one cannot with certainty determine the number of photons in the pulse, which adds an uncertainty to the measured charge resolution with this setup.

The charge resolution determines how well one can reconstruct the exact number of registered photons that created an SiPM signal pulse. The uncertainty of the photon number in a laser pulse can later be subtracted from the measured total uncertainty of the charge to determine the uncertainty of the electronics (and the SiPM) alone.

The laser repetition rate is set to 2 kHz for all illumination measurements. Every time a pulse is fired the laser also emits a signal that is connected to the evaluation board and can be used as external trigger. This signal can even be emitted when the laser is turned off and serves as external trigger for pedestal measurements for the illuminated experiments.

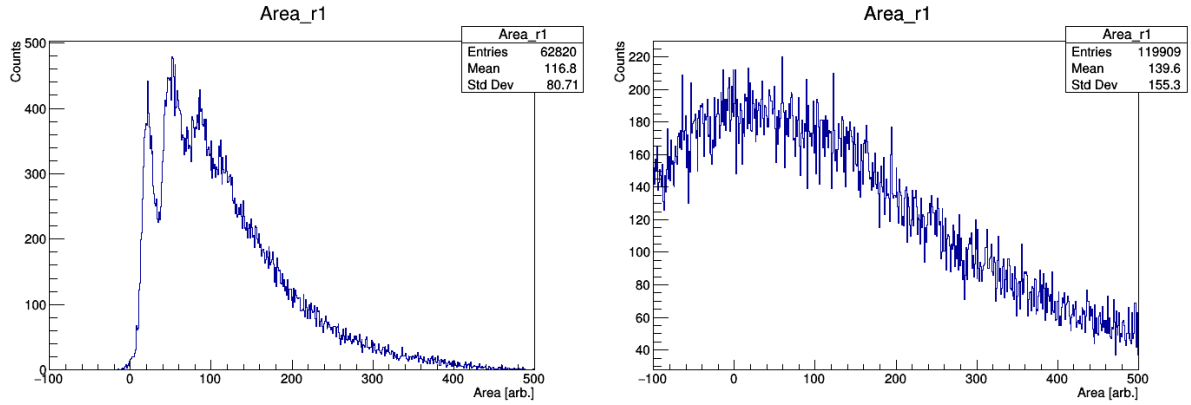

Figure 35 – Area spectra for the standard shaper at low laser intensity (mean $N_{p.e.} \approx 3$). On the left: spectrum for an SiPM voltage of 31.2 V. On the right: Spectrum for 33.9 V (corresponding to a gain of $\sim 6\,mV$ per p.e.)

6.3.1 Overvoltage Dependency

For the measurements of the overvoltage dependency a low intensity was chosen that corresponds to 2.95 ± 0.15 p.e. (Filter wheel position 1900). How this value is determined is discussed in this section 6.4.3.

The dependency of the signal attributes (such as e.g. amplitude, area, peak position, etc.) on the applied SiPM overvoltage is examined. For the modified shaper overvoltages of $27.9\,V$, $30.0\,V$, $30.4\,V$, $30.8\,V$ and $32.0\,V$ were tested; for the standard shaper $31.2\,V$ and$33.9\,V$. This measurement is used to determine the optimal overvoltage to get the best "finger spectrum" of the area histogram and thus the best charge resolution.

For the standard shaper at $31.2\,V$ the area spectrum does show peaks for zero, one and two p.e. but they are not very clear. This is probably due to the relatively low gain of the standard shaper which makes it difficult to separate individual peaks even for a low number of photon events.

If the voltage is increased to $33.9\,V$, which corresponds to a gain of $6\,mV$ per p.e., the spectrum loses all peak features and even shows a large extension into negative areas. This is probably due to the very high dark count rate at this SiPM voltage that causes strong signal pile up. The two area spectra for the standard shaper are shown in Fig. 35. Both spectra are shown in only pedestal calibrated form. The TF calibration held no significant improvement for the spectrum at $31.2\,V$.

Different cut criteria have again been applied to the fits of the SiPM events in order to optimize the area spectrum with regard to the visibility of individual peaks. All graphs that are shown here represent the best possible area spectrum that was achieved with certain cut criteria.

For the modified shaper the best SiPM voltage was determined to be $30.4\,V$. It has sufficient gain ($7.5\,mV$ per p.e.) and sufficiently low noise to yield a good finger spectrum for low intensities, as dark counts and crosstalk are not too high for this SiPM voltage.

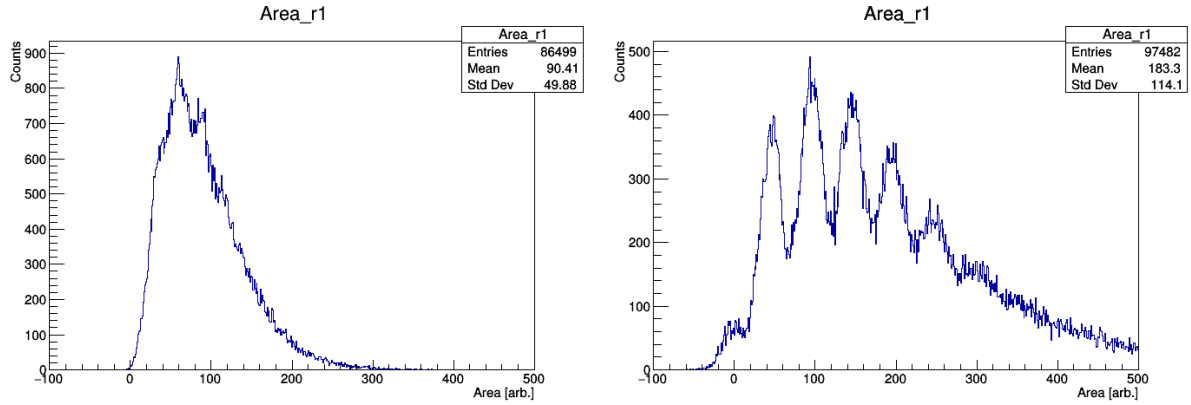

Figure 36 – Comparison of the area spectra of the modified shaper at a at low laser intensity (mean $N_{p.e.} \approx 3$) for an SiPM voltage of$27.9\,V$ (left) and $30.4\,V$ (right). The right spectrum shows a much better separation between individual peaks.

A comparison between the area spectra of the modified shaper at $27.9\,V$ and $30.4\,V$ SiPM voltage is shown in Fig. 36. Both spectra are taken from only pedestal calibrated data, because the TF did not improve the area spectrum significantly or even made it worse at this stage.

All in all the modified shaper shows a much better performance in terms of the resolution of individual peaks in the area spectrum.

6.3.2 VPED Dependency

In order to get a higher quality of the TF calibration the VPED of the signal was altered from 1100 to 1200 and 1300. The VPED shifts the signal by a constant offset. This shifts the signal into a region of the TF where the slope is less steep and the ratio of ADC counts per mV input amplitude is larger. Thus, the TF has a higher resolution at this working point. This comes at the price of a reduced dynamic range as the upwards shifted signal causes the cells of the Target ASIC to saturate earlier.

For the data taken with the standard shaper the higher VPED did improve the spectrum only marginally.

For the modified shaper, however, increasing VPED greatly improves the area spectrum. The effect is strongest for a VPED of 1300 but also considerable for a VPED of 1200. Thus, as a good compromise between possible charge resolution and dynamic range, a VPED value of 1200 was chosen for all following measurements. A comparison of the area spectrum of the modified shaper for a VPED value of 1100 and 1200 is shown in Fig. 37.

The quality of the area spectrum and thus the possible charge resolution of the modified shaper proved superior to the standard shaper. For this reason (and because the dynamic range of the modified shaper is still acceptable) it has been decided to use the modified shaper for the IceAct. The final parameters for all future measurements are a VPED of

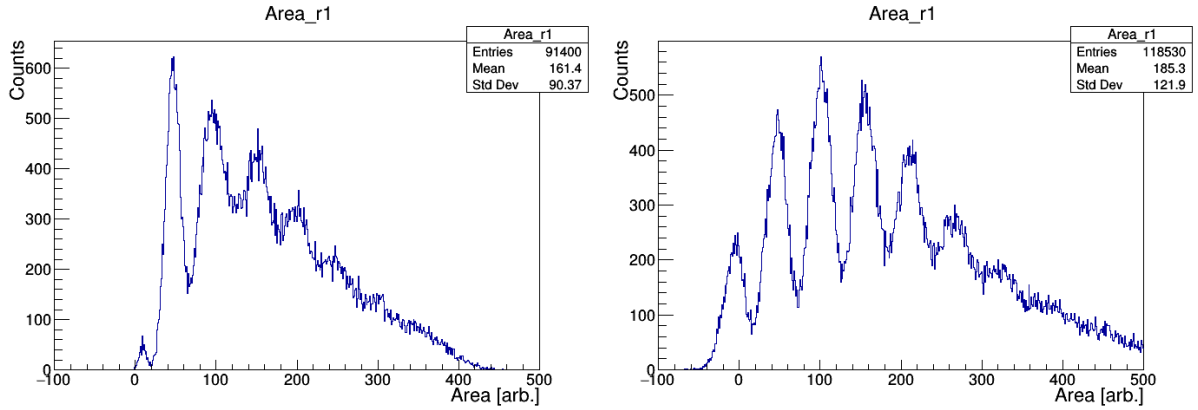

Figure 37 – Comparison of the area spectra of the modified shaper at a at low laser intensity (mean $N_{p.e.} \approx 3$) and an SiPM voltage of 30.0 V with a VPED value of 1100 (left) and 1200 (right).

1200, a SiPM overvoltage of 5.9 V (30.4 V applied high voltage), a Thresh value of 1802 and an PMTref4 value of 1786.

6.3.3 Shaper Gain and Linearity Measurement

For the modified shaper version the amplification factor and its linearity over different signal intensities have been measured. The input signal to the shaper was produced with the frequency generator and was the same as used for the recording of the transfer function. Input pulses in the range of $-100\,mV$ up to $+2000\,mV$ were applied to the shaper. The output signal of the shaper was recorded with an oscilloscope and averaged over 128 pulses for each input voltage. The amplitude of the output signal pulses over the input signal pulses is shown in Fig. 38 for the non-saturated regime. The red crosses mark the measured data and the blue line is a linear fit to the data with a slope of 1.66 ± 0.03 that represents the gain of the shaper. The fit matches the data quite well up to $\approx 500\,mV$. A slight decrease ($\sim 6\%$) of the measured output amplitude from the fit is visible for the input amplitude of $1000\,mV$ that marks the beginning of the shaper saturation.

An additional measurement at $+2000\,mV$ input amplitude was well in the saturated regime of the shaper, which yields a maximum output of $+1900\,mV$. The gain of the shaper slowly drops near the saturation until the shaper reaches its maximum output amplitude of $1900\,mV$. The oscilloscope picture of such a saturated shaper output pulse is shown in Fig. 39. The distinct dip between the main peak and the tail of the pulse is clearly visible on this picture and is thus definitively a feature of the shaper and not of Target.

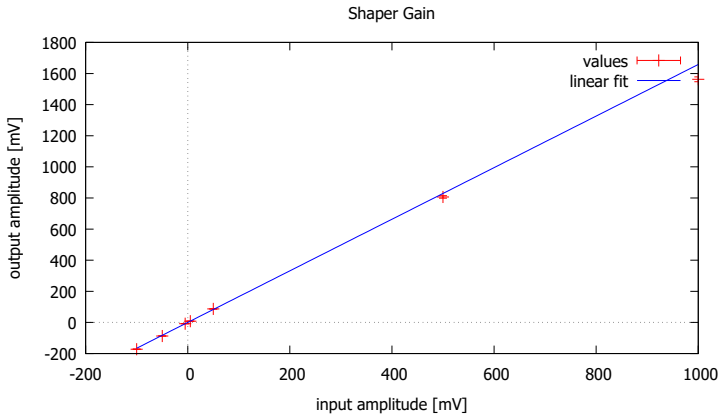

Figure 38 – Plot of the measured gain of the modified shaper for different amplitudes of the modified preamp signal. The blue line is a linear fit to the data with a slope of 1.66 ± 0.03 that equals the gain of the shaper. It is very linear over the regime of $-100\,mV$ up to $+500\,mV$, but shows a slight decrease already for $1000\,mV$ which marks the beginning of the saturated regime.

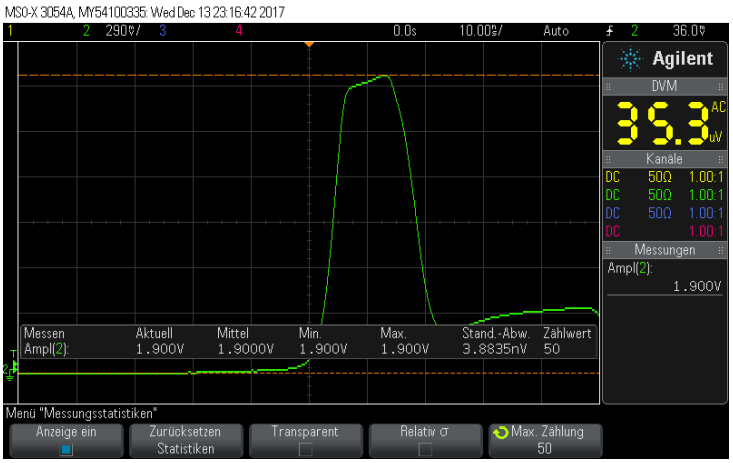

Figure 39 – Oscilloscope picture of a fully saturated shaper output pulse. The distinct dip between the main peak and the tail is (at least partly) visible.

6.4 Charge Resolution and Saturation Behavior

The charge resolution determines how well the number of incident photons that are recorded with the SiPM can be reconstructed from measured data. The number of incident photons is proportional to the amount of Cherenkov light in an air shower and thus to the total energy of the incident cosmic particle. The better the charge resolution the better the energy resolution of the camera.

As already briefly mentioned in section 5.3, the charge is a measure for the amount of fired micro-cells in the SiPM and thus the number of registered photon events. When one or more microcells in the SiPM fire, they emit an electrical current pulse. The area of that pulse is proportional to the number of registered p.e. and is determined by its amplitude $I(t)$ and the duration time of the pulse. Thus, the area is given in the unit of electrical charge ($Q = I \cdot t$). The current signal is changed to a voltage signal in the preamp and the pulse form is altered in the shaper, which causes a change of the absolute value of the area. However, the ratio between the area of signals with different number of p.e. is retained. Thus, the area of the signal pulse after the shaper is still a good measure for the amount of photon events. Its unit is $[mV \cdot ns]$ which is not the physical unit of charge anymore, nonetheless the name is kept. From a histogram of the area of the events one can determine the relation between p.e. and measured charge.

6.4.1 Selection of the Integration Interval for Area Measurements

To achieve the best possible charge resolution the area of the event signals must be determined as exactly as possible. At this point a systematical examination of the best method to determine the area was performed. The resulting optimal fit window is applied for all following measurements, in particular the determination of the charge resolution and the saturation behavior.

The area for each event is calculated by detecting the position of the signal peak for every measured event with a Gaussian fit and then summing up the entries in a certain interval of time bins around this position. The so determined area depends, of course, on the width of this interval. In an ideal, noise free case, one could just sum over the whole waveform to determine the area of the peak. The baseline of the waveform would be exactly zero before and after the event peak and would not have any effect on the area off the peak. In reality, however, noise is always present and a too wide integration window also catches more noise that distorts the area measurement and blurs the separation between different peaks in the area histogram. A too narrow window, on the other hand, fails to contain all available information about the signal peak as the edges of the peak are cut off.

The selection of the optimal fit window is not obvious and has to be determined experimentally. Therefore, different fit windows have been tried out and their noise level was compared. In order to get a measure for the noise the one p.e. peak is analyzed and its width (σ_1) is determined via a Gaussian fit. The effective noise depends on how good one can separate different p.e. peaks in the area histogram. The gain determines how far two peaks with a consecutive number of p.e. are from another. Thus, the ratio $\frac{\sigma_1}{gain}$

determines the effective noise. The gain is measured by fitting the two p.e. peak with a Gaussian fit and determine the distance between the mean values of the one p.e. and two p.e. peak.

As the signal peaks are not symmetrical (sharp rise time, followed by an undershoot or a plateau like tail for higher intensities) the interval to determine the area is set asymmetrically around the peak position (pp). The initial guess was to take an interval from pp-9 to pp+7 which yields an effective noise of 0.272. A systematic analysis was started by varying both the upper and lower boundary of the interval around the initial guess. The lower boundary was varied between pp-2 and pp-14 and the upper boundary between pp+2 and pp+14.

An automation of the Gaussian fits (to determine σ_1 and the gain) of the peaks in the area histogram proves tricky because their positions are shifting for different intervals and good start values for the fits could not be determined. Thus, the fits were performed by hand for a selection of possible intervals and a gradient method was used to find the optimal interval. Starting from the initial guess the upper and lower boundary of the fit interval was varied by ± 1. If the noise was smaller than before for any of these changes, the method is repeated for this new value until a local minimum of the noise is found. To ensure that this is not only a local but a global minimum, several other intervals were chosen at random and their noise was evaluated. The lowest effective noise of0.255 was found for the interval of pp-8 to pp+6. This interval has been chosen to determine the area for the charge resolution measurement and the saturation measurements in section 6.4.5.

6.4.2 Relation of Charge to the Number of p.e.

To recover the number of p.e. from the area/charge in $[mV \cdot ns]$ of an event, the area that is produced per p.e. must be determined. The charge per p.e. is exactly equal to the gain per p.e. and is measured the same way as mentioned above (in section 6.4.1).

Therefore the area spectrum of the SiPM signal for low intensity illumination (mean photon number per pulse ≈ 3) and the modified shaper is considered. A graph of this spectrum is shown in Fig. 40 on the right. Only the mean values of the one p.e. and two p.e. peaks are considered as the area spectrum grows blurrier with increasing number of photon events. The mean values of further peaks exhibit greater errors and would not improve the accuracy of the value. The charge per p.e. is given by:

$$\frac{charge[mV \cdot ns]}{p.e.} = 40.79 \pm 0.22 \tag{10}$$

The error stems from the fit uncertainty of the mean values of the Gaussian fits. As the charge grows linear with the number of p.e. over the full range of light intensities this relation holds for any number of p.e. up to the saturation. For saturated pulses the area/charge can no longer grow with light intensity and this relation breaks down.

6.4.3 Calculation of the Laser Intensity in Units of p.e.

The laser intensity can be set via a filter wheel (FW) that attenuates the laser beam depending on its rotational position. The FW positions used here range from 1900 (weakest intensity) up to 300 (strongest intensity) in steps of 100. The relation of laser intensity to filter wheel position is not linear and has been measured by Benedikt Herrmann at ECAP via a photo diode module in the laser box. The voltage output of the photo diode module rises linear with intensity.

The important unit of intensity for the IceAct is the number of p.e. that are registered in the SiPM. It is thus necessary to determine the (mean) number of p.e. that are registered in the SiPM for any given laser intensity. Note that the number of registered photons in the SiPM is not the number of photons that are contained in a laser pulse. Some photons are lost in the coating or the grid between the microcells and the quantum efficiency of the SiPM is smaller than one. However, the fraction of "lost" photons stays constant for any number of photons contained in the laser pulse. A relation of filter wheel position to (mean) registered p.e. is determined in the following.

The mean number of p.e. detected by the SiPM rises linearly with the light intensity over the full range of intensities measured here, as discussed in section 2.2. The exact light intensity in units of W/m^2 is not determined as it is not needed.

The number of photons per laser pulse follows a Poisson statistic which is especially pronounced for low intensities (i.e. only a few photons per pulse). The discrete Poisson distribution is given by:

$$P(k) = \frac{e^{-\lambda}\lambda^k}{k!} \tag{11}$$

for $k \in \mathbb{N}^+$ and λ the mean value of the distribution. This means that for a mean number of p.e. of e.g. $\lambda = 3$ the laser pulse can contain any number of photons, even zero.

The area histogram of a measurement, run with external trigger under illumination with low intensity laser light, represents such a Poisson statistic. The different peaks mark different number of photon events. The leftmost peak around zero contains events with zero p.e., the following peaks mark events with an increasing number of photon events. A comparison of the area histogram and a Poisson statistic is shown in Fig. 40. On the left a plot of a discrete Poisson distribution for $\lambda = 3$ is shown; on the right the area spectrum of the modified shaper for illumination with low intensity light (filter wheel position 1900) is shown for an SiPM voltage of $30.4\,V$.

One can determine the mean number λ of a Poisson distribution by looking at the probability for $k = 0$. It is given by:

$$P(0) = \frac{e^{-\lambda}\lambda^0}{0!} = e^{-\lambda} \tag{12}$$

Thus λ is given by:

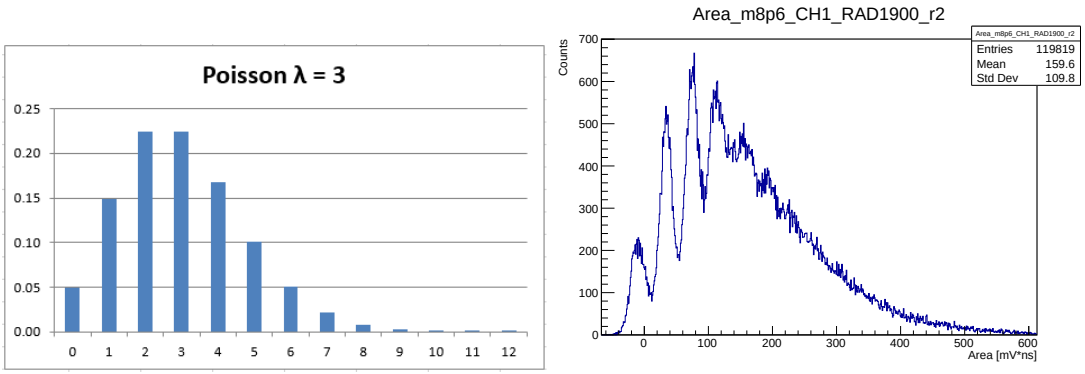

Figure 40 – On the left: Plot of a discrete Poisson distribution for $\lambda = 3$. On the right: Area histogram of the modified shaper for illumination with low intensity light (filter wheel position 1900) and for an SiPM voltage of $30.4\,V$.

$$\lambda = -ln(P(0)) \tag{13}$$

In the area spectrum λ represents the mean number of p.e. ($N_{p.e.}$) and $P(0)$ is the probability that no photon was registered by the SiPM. It is represented by the pedestal peak. $P(0)$ can be calculated by dividing the number of events that contained zero photons (N_0) by the total number of events N_{events} that were recorded:

$$P(0) = \frac{N_0}{N_{events}} \tag{14}$$

There are two different methods to determine N_0 from the area histogram. One can make a cut in the valley between the pedestal peak and the first peak. This is simple, but the exact position at which the cut is performed is somewhat arbitrary. A different method is to perform a Gaussian fit of the pedestal peak and calculate the integral. Both methods have been applied and compared to obtain a mean value and an estimation of systematic errors.

The cut method yields $N_0 = 6402$. For an estimation of the statistical error $\sqrt{N_0}$ is assumed as uncertainty. This gives a value of

$$N_{0,cut} = (6.40 \pm 0.08) \cdot 10^3$$

for the cut method.

The integral of a Gaussian with amplitude A and standard derivation σ is given by:

$$\int_{-\infty}^{+\infty} A \cdot exp(-\frac{1}{2} \cdot \frac{x^2}{\sigma^2}) = \sqrt{2\pi}\sigma A \tag{15}$$

With $A = 216 \pm 4$ and $\sigma = 11,39 \pm 0,24$ this yields:

$$N_{0,fit} = (6.17 \pm 0.17) \cdot 10^3$$

Thus the final value for $N_0$is given by:

$$N_0 = \frac{N_{0,cut} + N_{0,fit}}{2} = (6.29 \pm 0.16 \pm 0.13) \cdot 10^3 \tag{16}$$

Where the first error is the systematic error of the two different methods, and the second errors stems from the combined statistical errors of the two methods. The value for N_0 with the combined errors is given by:

$$N_0 = (6.3 \pm 0.3) \cdot 10^3 \tag{17}$$

With error propagation and according to Eq. 13 the mean number of p.e. for illumination with laser light at a filter wheel position of 1900 is given by:

$$N_{p.e.}(1900) = -ln(\frac{N_0}{N_{events}}) = 2.95 \pm 0.15 \tag{18}$$

Then the mean number of p.e. $N_{p.e.}(x)$ for any position x of the filter wheel can be determined via the relation of filter wheel position and photo diode current $I_{ph}(x)$ and the linear relation between intensity (in p.e.) and photo diode current:

$$N_{p.e.}(x) = I_{p.h}(x) \cdot \frac{N_{p.e}(1900)}{I_{ph}(1900)} \tag{19}$$

The intensity in p.e. for all used filter wheel positions is listed in tab. 2 and ranges from ~ 3 to 1580.

Note that this method yields the number of registered incident photons in the SiPM without crosstalk. Events, that contain no photons (N_0) are not affected, since at least one photon must be present to create crosstalk. The total number of events N_{events} is also not affected, because crosstalk changes the number of photons in an event, but not the number of events itself. Thus, this method of reconstructing the intensity in p.e. yields the distribution of incident photons that are registered by the SiPM without counting those which are crated by crosstalk.

In order to take crosstalk into account, the heights of individual area peaks and their deviation from an ideal Poisson statistic would have to be considered. A method to asses the crosstalk via a multi Gauss fit exists and was implemented at ECAP by Oleg Kalekin but could not be applied to the data in the scope of this thesis.

FW pos.	mean, incident $N_{p.e.}$
1900	2.95 ± 0.15
1800	4.19 ± 0.20
1700	5.99 ± 0.29
1600	8.7 ± 0.5
1500	12.6 ± 0.6
1400	18.0 ± 0.9
1300	26.5 ± 1.3
1200	38.3 ± 1.9
1100	55.2 ± 2.7
1000	79 ± 4
900	115 ± 6
800	166 ± 8
700	239 ± 12
600	341 ± 17
500	501 ± 24
400	$(7.5 \pm 0.4) \cdot 10^2$
300	$(15.8 \pm 0.8) \cdot 10^2$

Table 2 – Table of light intensities in units of mean, incident p.e. in the SiPM and the corresponding filter wheel positions.

6.4.4 Extension of the Integration Interval to Cover the Tail of Saturated Pulses

Saturated pluses show not only the main peak but a long, plateau like tail after this peak. The tail has a near constant height but its length depends on the extent of the saturation. The more saturated the pulse, the longer the tail. A comparison of a non saturated ($N_{p.e.} \approx 4$) and a saturated pulse ($N_{p.e.} \approx 341$) is shown in Fig. 41. The saturated pulse is shown on the right; the elongated, plateau like tail is clearly visible. The saturated pulse was truncated to a height of1300 in order to eradicate of effects caused by different saturation behavior of different cells.

This makes it possible to measure, to some extent, the level of saturation via the length of the tail and to extend the saturation limits of the electronics. The limit of this method is reached when the pulse tail is longer than the readout window. To optimize the yield of this method the trigger delay could be adjusted, so that the pulse appears earlier in the window or the digitization window could be elongated.

To take the tail into account one has to adjust the integration window and extend it from pp-8 to the end of the digitized waveform (i.e. bin 127). This, however, enables more noise to enter into the determination of the area and worsens the resolution for low intensity light.. A comparison of the area spectra for the two different integration intervals is shown in Fig. 44. Note that no individual area peaks are recognizable in the area spectrum of the long integration window, as the higher noise level blurs out the peaks. Therefore the

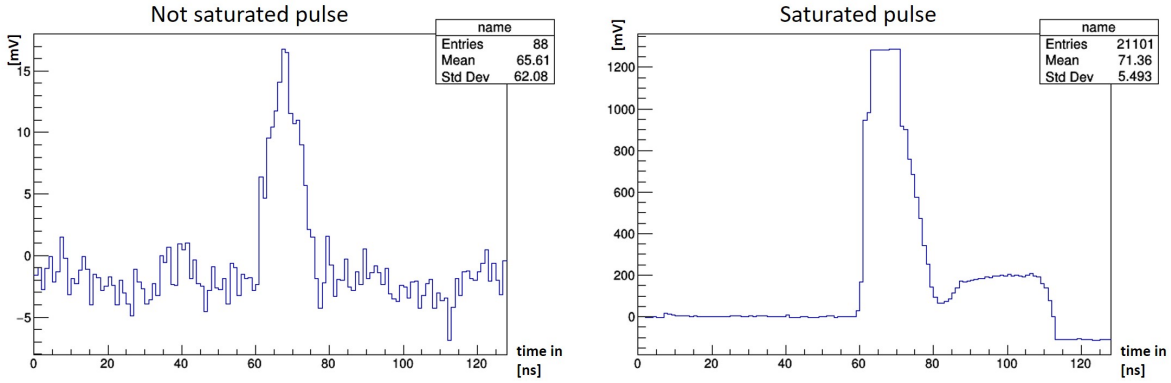

Figure 41 – Comparison of a non saturated pulse at FW pos. 1900 (left) and a saturated pulse at FW pos. 600 (right). For the saturated pulse the elongated, plateau like tail is clearly visible.

same value of charge per p.e. that was determined for the short integration window (in section 6.4.2) has to be assumed for the long integration window. The values should, however, be equal since the long integration window does not change the shape of the peak and both integration windows cover the full peak for low light intensities.

6.4.5 Saturation Behavior

The (integration window dependent) saturation behavior of the electronics and Target determines the maximum number of p.e. that can be resolved. Thus, when the full camera will be operated to measure air showers, it will determine the maximum energy that the IceAct can resolve.

To measure the saturation behavior the laser intensity is increased in several steps until the full saturation is reached. For each laser intensity $\sim 1.2 \cdot 10^5$ events were taken and their mean area is determined from the area histograms.

The saturation behavior of the readout electronics and Target is then determined by plotting the mean charge over the laser intensity in [p.e.] for both the short and the long integration interval. The plot is shown in Fig. 42. Note that both axes are in units of p.e. but the charge was calculated via the area per p.e. and the laser intensity via the Poisson statistic of the incident laser. The blue markers show the long integration interval, the red ones the short. The measured charge rises with increasing intensity until the signals saturate. The saturation in pulse height is reached for intensities greater than 239 p.e., which is evident by the stagnation of the charge measured with the short integration interval after this point. The short interval does not include the pulse tail and is thus only sensible to the height and width of the main peak.

The maximum number of p.e. that is reconstructable with the long integration interval is ≈ 800. The inclusion of the long pulse tail thus enables the reconstruction of a much higher number of photon events. The error bars in the plot show the standard deviation of the charge that is produced by the electronics alone. The effects of the Poisson spread

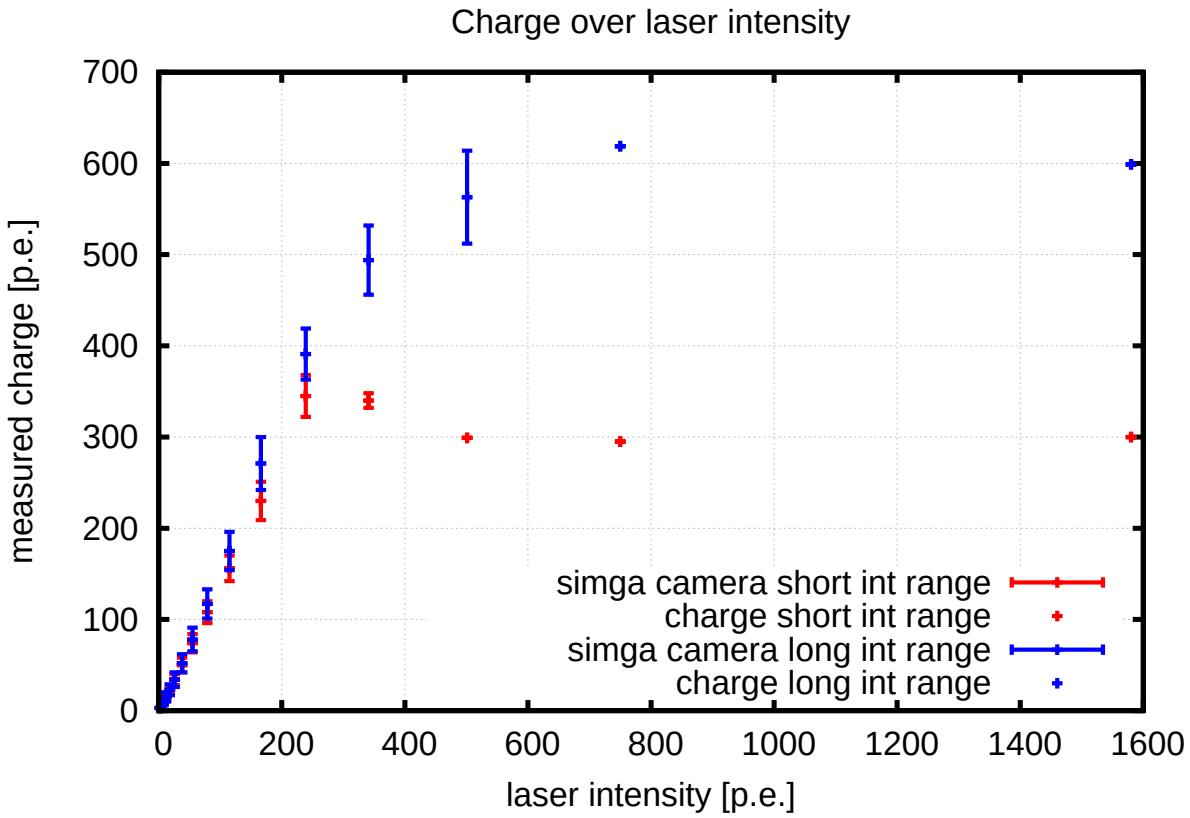

Figure 42 – Saturation behavior of the readout electronics including Target. The measured charge in [p.e.] is plotted over the incident laser intensity in [p.e.]. The saturation is reached when the slope of the graph becomes negligible. The blue symbols mark the long integration interval, the red ones the short interval. The short interval saturates earlier. The error bars mark the purely electronic error in charge reconstruction without the uncertainty added by the Poisson distribution of the photon number in a laser pulse.

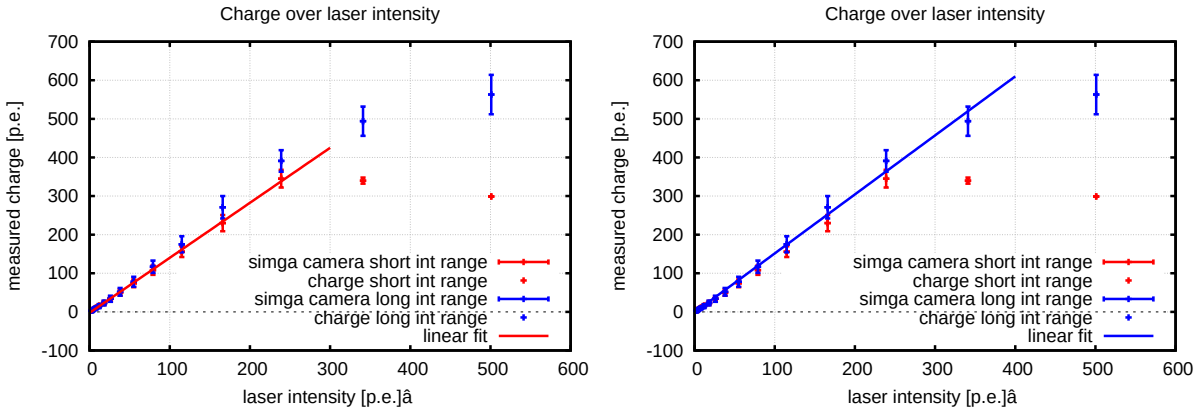

Figure 43 – Zoomed in view of the charge over intensity graph. The graph on the left shows a linear fit for the short int. interval; the one on the right shows a linear fit for the long int. interval.

of the laser are excluded. The error appears to grow smaller near the saturation, but this is only an apparent effect that is caused by a narrowing of the area spectrum for saturated pulses that does not allow to determine the real error of the measured charge anymore. The error of the charge reconstruction is discussed in more detail in section 6.4.6.

Fig. 43 shows a zoomed in view on the low intensity part with a linear fit of the data. The graph on the left contains the short int. interval with a slope of 1.43 ± 0.02 and the one on the right shows the long int. interval with a slope of 1.53 ± 0.04.

The reconstructed charge deviates between the two integration interval. For small numbers of p.e. the long integration interval systematically underestimated the charge by $\sim 20\%$. With increasing number of p.e. the deviation decreases until both methods yield roughly the same value at 26.5 photon events. For higher number of p.e. the long integration interval starts to overestimate the charge increasingly up to $\sim 20\%$ at a number of p.e. of 166. For even higher number so p.e. the short integration window starts to saturate and the charge of the two methods can no longer be compared directly.

A possible explanation for this is, that the undershoot is fully taken into account by the long integration interval. The undershoot is present for all pulses but does not grow linear with pulse height. For low pulses the effect of the undershoot is large and decreases the measured charge for the long integration interval. For large pulses, however, the undershoot is less pronounced in comparison to the pulse height and thus has a smaller effect. Furthermore for the long integration window more bins are summed up (which includes e.g. dark count events in the tail) and thus the charge in p.e. is systematically overestimated. For large (but not yet saturated) pulses this effects dominate the effects of the undershoot and the overall charge is overestimated.Thus, the slope of the fit on the data points of the long integration interval is higher. For saturated pulses the long integration window yields, of course a higher charge, as the plateau in the pulse tail is taken into account.

The reason why the slope is greater than one in both cases is crosstalk. The charge

on the vertical axis is reconstructed from the area per p.e. and was determined from the one and two p.e. peaks in the area spectrum. Thus, it is sensible to crosstalk, as more fired microcells cause a greater signal area and thus more charge in units of p.e. is reconstructed.

The horizontal axis is determined via the Poisson statistics of the laser and does not include crosstalk as discussed at the end of section 6.4.3. The slope of the linear fits is thus a measure for the ratio of total extra charge created by crosstalk to the charge created by primary photons.

A method to check this is calculating the total extra charge created by crosstalk via the crosstalk probability. According to the data sheet of the SiPM the crosstalk probability is 25% for an overvoltage of $6\,V$. The SiPM is operated at $5.9\,V$ here but it can be assumed that the value still holds. This means that the probability to get at least one extra photon ($p(\geq 1)$) per primary photon is $\frac{1}{4}$. The probability to get at least two extra photons ($p(\geq 2)$) is $(\frac{1}{4})^2$ and so on. However, the probability to have exactly one extra photon ($p(1)$) is given by:

$$p(1) = p(\geq 1) - p(\geq 2) \tag{20}$$

The same formula holds for any other number of extra photons. The total extra charge created by crosstalk (Q_{ct}) is then given by:

$$Q_{ct} = \sum_{n=0}^{\infty} n \cdot Q \cdot p(n) \tag{21}$$

Where Q is the charge created by one photon. Numerically calculating this up to a high order (arbitrarily chosen to the 26th order) yields a total ratio of extra charge due to crosstalk (Q_{ct}) to charge created by primary photons (Q_{prim}) of :

$$\frac{Q_{ct}}{Q_{prim}} = 0.3422 \tag{22}$$

This is below the slope that the linear fit on the data with the short integration interval in Fig. 43 predicts. In order to fulfill this value the crosstalk probability would have to be 30%. This can, however, be the case as the crosstalk probability from the data sheet is only a mean value for this type of SiPM and individual SiPMs can deviate from that. Furthermore, the crosstalk probability increases with SiPM temperature which probably rises above the $20°\,C$ assumed in the data sheet during a measurement. Crosstalk is thus a plausible explanation for this discrepancy between measured number of p.e. via charge and predicted number of p.e. via the Poisson statistic of the laser. To precisely determine the cross talk, an analysis of the full Poisson like distribution of the area spectrum would have to be made, as briefly discussed in section 6.4.3.

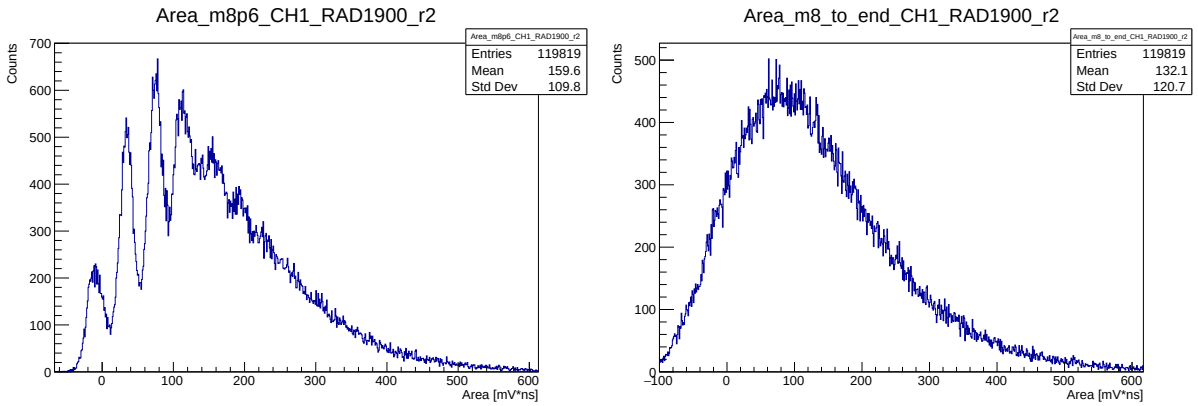

Figure 44 – Comparison of the area spectrum for the long and the short integration interval. Measured with the modified shaper at an SiPM voltage of 30.4 V with illumination of low intensity laser light ($N_{p.e.} \approx 3$). On the left: The short integration interval spectrum. On the right: The spectrum for the long integration range. The short integration interval shows a far better charge resolution and individual peaks are visible for the different number of photons in the peak.

6.4.6 Charge Resolution

The measurement error of the charge is given by the standard deviation of the whole area spectrum (σ_A) and can be easily be calculated from the area histogram. For low intensity light with the short integration interval an area spectrum with individual p.e. peaks is visible. This is illustrated in Fig. 44, which shows a comparison of the area spectra taken with the long and the short integration interval for low intensity light ($N_{p.e.} \approx 3$).

In both cases the overall mean of the area distribution is taken and its overall standard deviation is calculated with the program "root" (independent of the presence of individual peaks). The error of the area (σ_A) is composed of four parts:

- The Poisson fluctuation of the laser pulse σ_L
- The error in the transformation of area to units of p.e.
- The electronic- and SiPM induced uncertainty and calibration uncertainty in measuring the area
- The probabilistic shifts of $N_{p.e.}$ due to the quantum efficiency of the SiPM and the crosstalk

The fluctuation of the number of photons n that are contained in a laser pulse is given by the standard deviation of the Poisson distribution and is simply $\sigma_L = \sqrt{n}$. Furthermore, n itself has an error Δn that stems from the uncertainty in the determination of the number of events in the pedestal peak (see section 6.4.3) and is listed in Tab. 2. Thus, σ_L also contains an error which is given by:

$$\Delta\sigma_L = \frac{1}{2\sqrt{n}} \cdot \Delta n \tag{23}$$

σ_L can be separated from the other errors and be subtracted. The other three parts together form the error that is produced by the SiPM and readout electronics (or the "camera") and is thus called σ_C. It is given by:

$$\sigma_c = \sqrt{\sigma_A^2 - \sigma_L^2} \cdot 10^3 \tag{24}$$

When extracted from the area histogram σ_A has the unit $[mV \cdot ns]$ and has to be transformed to the unit $[p.e.]$ by the conversion factor of 40.79 ± 0.22, as described in section 6.4.2. Thus, also σ_A in [p.e.] contains an error.

The full error calculation for σ_C is given by:

$$\Delta\sigma_C = \left|\frac{\partial\sigma_C}{\partial\sigma_A}\right| \Delta\sigma_A + \left|\frac{\partial\sigma_C}{\partial\sigma_L}\right| \Delta\sigma_L \tag{25}$$

The values for $\sigma_C \pm \Delta\sigma_C$ for the short integration interval are given in tab. 3 for all intensities. The values for the long integration interval are shown in tab. 4.

Additional to the measured error of the charge, the night sky background (NSB) will also influence the charge resolution in a real environment. To take this effect into account a typical rate of NSB photons of 125 MHz is taken into account. The mean number of NSB photons ($\#NSB$) that would enter into the charge measurement under real conditions is given by the NSB rate times the length of the integration window and calculates to 1.875 photons for the short integration window (15 ns) and 8.75 photons for the long integration window ($\sim$ 70 ns). The exact length of the long integration window depends on the peak position and can thus vary by a few nanoseconds. For measurements under real conditions, the mean number of NSB photons would be subtracted from the total measured charge of each event. Therefore, it does not enter the calculation of the charge here. However, the NSB photons are statistically distributed and therefore they cause an additional error (σ_{NSB}) in the measurement of the charge. In order to make the error of the charge measurement that was determined from the illuminated experiment comparable to real measurements of air showers, σ_{NSB} must be taken into account. It is given by:

$$\sigma_{NSB} = \sqrt{\#NSB} \tag{26}$$

Thus the total error of the charge under real conditions (σ_{real}), including NSB but excluding the Poisson statistics of the laser is given by:

$$\sigma_{real} = \sqrt{\sigma_c^2 + \sigma_{NSB}^2} \tag{27}$$

mean $N_{p.e.}$	charge $[p.e.]$	σ_C $[p.e.]$	σ_{real} $[p.e.]$	$\frac{\sigma_{real}}{charge}$ in [%
2.95 ± 0.15	3.94 ± 0.03	2.17 ± 0.06	2.57 ± 0.06	65.2 ± 1.8
4.19 ± 0.20	5.62 ± 0.03	$2.55 \pm 0,07$	$2.89 \pm 0,07$	51.4 ± 1.4
5.99 ± 0.29	7.89 ± 0.05	3.00 ± 0.08	3.30 ± 0.08	41.8 ± 1.2
8.7 ± 0.5	11.23 ± 0.07	3.62 ± 0.11	3.87 ± 0.11	34.5 ± 1.2
12.6 ± 0.6	16.44 ± 0.09	4.45 ± 0.12	4.66 ± 0.12	28.3 ± 0.9
18.0 ± 0.9	23.59 ± 0.13	5.35 ± 0.14	5.52 ± 0.14	23.4 ± 0.7
26.5 ± 1.3	34.76 ± 0.19	6.66 ± 0.16	6.80 ± 0.16	19.6 ± 0.6
38.3 ± 1.9	50.8 ± 0.28	8.29 ± 0.19	8.40 ± 0.19	16.5 ± 0.5
55.2 ± 2.7	74.3 ± 0.4	10.47 ± 0.22	10.56 ± 0.22	14.2 ± 0.4
79 ± 4	108.6 ± 0.6	12.80 ± 0.27	12.87 ± 0.27	11.9 ± 0.4
115 ± 6	156.8 ± 0.9	14.9 ± 0.4	15.0 ± 0.4	9.57 ± 0.26
166 ± 8	230.0 ± 1.3	21.2 ± 0.4	21.2 ± 0.4	9.22 ± 0.23
239 ± 12	345.4 ± 1.9	23.5 ± 0.5	23.5 ± 0.5	6.80 ± 0.17
341 ± 17	(340.0 ± 1.9)	(8.3 ± 1.3)	(8.4 ± 1.3)	$(2.5) \pm 0.4$
501 ± 24	(299 ± 1.7)	-		-
$(7.5 \pm 0.4) \cdot 10^2$	(295 ± 1.6)	-		-
$(15.8 \pm 0.8) \cdot 10^2$	(300 ± 1.7)	-		-

Table 3 – Table listing the intensity in p.e., the corresponding charge, its error σ_C, its realistic error σ_{real} (including NSB) and its fractional charge resolution for the short integration interval.

The tables (tab. 4 and tab. 3) also contain this realistic error of the charge and the fractional charge resolution that was determined from it. As the NSB rate is not measured, but a reasonable value is assumed, σ_{NSB} does not have an error of its own. Therefore it doe not contribute to the error of σ_{real} , which thus stays the same as the error on $\sigma_c$that is discussed above.

The effect of the NSB is stronger for the long integration window, since there are more NSB photons within it. Furthermore, it is stronger for low intensities, since then the additional error is bigger relative to the total amount of measured charge.

When the signal saturates, the area can no longer grow. The maximum of the possible area is given by the saturation amplitude of the signal and the width of the integration interval. For saturated signals the area spectrum becomes a sharp peak at the end of the spectrum. Its width decreases and the measured σ_A becomes smaller. The laser uncertainty σ_L, on the other hand, grows continuously with the intensity. When the laser intensity is high enough for the signal to reach saturation, σ_L eventually becomes larger than σ_A and the calculation of σ_C does not make sense anymore. The values for the charge and its error σ_C, which encounter this problem, are marked with brackets in tab. 3.

By taking only the mean value of the area spectrum even when individual area peaks for different number of p.e. are visible, this method takes into account the uncertainties due to crosstalk and the SiPM quantum efficiency. The quantum efficiency and crosstalk

$N_{p.e.}$	charge $[p.e.]$	σ_C $[p.e.]$	σ_{real} $[p.e.]$	$\frac{\sigma_{real}}{charge[p.e.]}$ in [%
2.95 ± 0.15	3.30 ± 0.02	3.10 ± 0.02	4.28 ± 0.02	129.7 ± 2.1
4.19 ± 0.20	4.75 ± 0.03	3.66 ± 0.02	4.71 ± 0.02	99.2 ± 1.6
5.99 ± 0.29	7.26 ± 0.04	4.25 ± 0.03	5.18 ± 0.03	71.3 ± 1.3
8.7 ± 0.5	10.56 ± 0.06	5.10 ± 0.03	5.89 ± 0.03	55.8 ± 1.2
12.6 ± 0.6	15.67 ± 0.09	6.34 ± 0.04	7.00 ± 0.04	44.7 ± 0.9
18.0 ± 0.9	23.0 ± 0.13	7.64 ± 0.05	8.19 ± 0.05	35.6 ± 0.7
26.5 ± 1.3	34.74 ± 0.19	9.55 ± 0.06	10.00 ± 0.06	28.8 ± 0.6
38.3 ± 1.9	52.00 ± 0.29	12.10 ± 0.09	12.46 ± 0.09	24.3 ± 0.5
55.2 ± 2.7	78.4 ± 0.5	15.29 ± 0.08	15.57 ± 0.08	19.9 ± 0.4
79 ± 4	117.8 ± 0.7	19.01 ± 0.11	19.24 ± 0.11	16.33 ± 0.28
115 ± 6	175.9 ± 1.0	23.6 ± 0.13	23.78 ± 0.13	13.52 ± 0.23
166 ± 8	271.7 ± 1.5	32.49 ± 0.18	32.62 ± 0.18	12.01 ± 0.20
239 ± 12	391.3 ± 2.2	32.08 ± 0.18	32.21 ± 0.18	8.23 ± 0.15
341 ± 17	494.2 ± 2.7	42.56 ± 0.23	42.66 ± 0.23	8.63 ± 0.15
501 ± 24	564 ± 4	55.9 ± 0.4	56.0 ± 0.4	9.93 ± 0.16
$(7.5 \pm 0.4) \cdot 10^2$	620 ± 4	(13.36 ± 0.08)	(13.68 ± 0.08)	-
$(15.8 \pm 0.8) \cdot 10^2$	599 ± 4	(13.44 ± 0.08)	(13.76 ± 0.08)	-

Table 4 – Table listing the intensity in p.e., the corresponding charge, its error σ_C, its realistic error σ_{real} (including NSB) and its fractional charge resolution for the long integration interval.

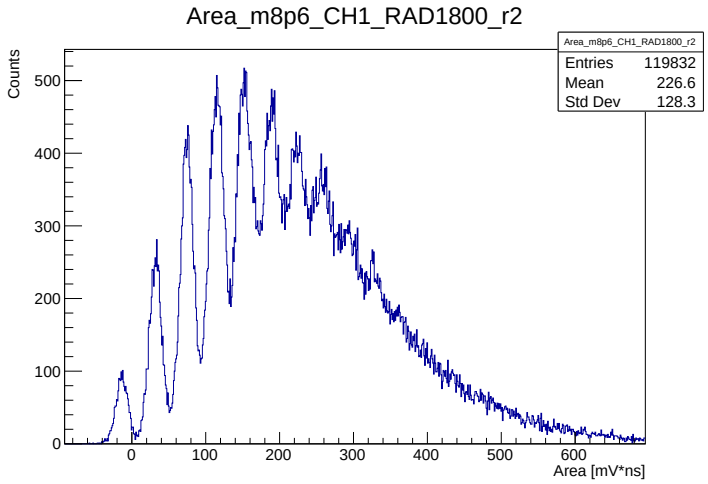

Figure 45 – Area spectrum for the short integration interval at an illumination with a mean number of p.e. of $N_{p.e.} = 4.19 \pm 0.20$. The individual area peaks are clearly recognizable and fitable up to the seven p.e. peak.

both change the number of registered photons in a probabilistic fashion and one cannot with certainty correlate the measured number of photons to the actual number of photons hitting the SiPM; especially not for small events. There might e.g. be 11 photons that hit the SiPM of which only three or four are registered due to the quantum efficiency and then another one or two could be added by crosstalk.

When looking at an area peak created by a certain number of p.e. in a finger spectrum, however, the number of photons is exactly given and these effects are excluded. Thus, the noise that is created by the electronics, the SiPM and the calibration uncertainty, can be estimated by measuring the width of the individual peaks in a low intensity finger spectrum. Such an area spectrum for the short integration range for an illumination intensity of $N_{p.e.} = 4.19 \pm 0.20$ is shown in Fig. 45. This particular spectrum shows individual peaks that are fitable with a Gaussian function until the seven p.e. peak.

By performing a Gaussian fit on individual peaks their charge is given by their mean value and their charge resolution (σ_C) is given by their width. The values determined with this method for the are shown in tab. 5.

For the long integration interval no individual area spikes are not recognizable for any illumination intensity and the method cannot be applied. For higher illumination intensities than shown in Fig. 45 even the short integration interval does not show individual peaks anymore. Thus, this method of high quality charge reconstruction is limited to $N_{p.e.} \leq 7$.

The fact that the first peak in tab. 5 has an absolute charge smaller than one is due to an offset of the area spectrum (pedestal peak is left of the zero). However, the charge per p.e. seems to shrink with increasing number of p.e., which is evident from the table. This trend can not be explained by the errors in the Gaussian fit of the peak positions. The Poisson statistic of the laser was not used here as the number of p.e. was simply inferred

$N_{p.e.}$	charge [$p.e.$]	difference in [p.e.]	σ_C [$p.e.$]	$\frac{\sigma_C}{charge}$ in [%
1	0.79 ± 0.01	-	0.22 ± 0.01	28.1 ± 0.9
2	1.84 ± 0.02	1.05 ± 0.03	0.23 ± 0.01	12.6 ± 0.4
3	2.83 ± 0.02	0.99 ± 0.04	0.28 ± 0.02	9.9 ± 0.4
4	3.76 ± 0.03	0.93 ± 0.05	0.34 ± 0.01	9.1 ± 0.4
5	4.63 ± 0.04	0.87 ± 0.07	0.34 ± 0.2	7.4 ± 0.5
6	5.49 ± 0.05	0.86 ± 0.09	0.44 ± 0.4	8.1 ± 0.8
7	6.27 ± 0.06	0.76 ± 0.11	0.63 ± 0.08	10.2 ± 1.4

Table 5 – Charge and (fractional) charge resolution for the first seven p.e. determined with the short integration interval by fits on individual peaks in the area spectrum.

from the number of the peak. This strongly hints that the area or charge of a measured pulse is in fact not a linear measure for the number of p.e. (at least for small numbers of p.e.). This is a problem, since the relation of charge to p.e. was determined from the differences between the one p.e. peak and the two p.e. peak in the area spectrum. Thus the amount of charge that one p.e. produces is overestimated in high amplitude pulses that consist of many photon events. This leads to an underestimation of the number of registered p.e. from the determined charge. A possible explanation for this behavior might be that the pulse form is slightly different for pulses with a low number of photon events.

The linear fits in Fig. 43, however, indicate that the ratio of charge per p.e. becomes stable above a certain number of p.e. and only the first few p.e. produce more charge than the rest. The fractional charge resolution is affected by this only in a minor fashion. Both the total charge and the error of the charge σ_C are converted from area to p.e. with the same ratio and the error cancels out. However, σ_A is converted to units of p.e. to enable the subtraction of the laser uncertainty σ_L (Eq. 25). As σ_C is overestimated due to the wrong charge reconstruction (but σ_L is not), the effect of the laser is underestimated. Thus, the fractional charge resolution will be slightly better than calculated here.

There are no official requirements for the charge resolution of the IceAct. To gain some measure of the performance of the IceAct electronics its fractional charge resolution is compared to the requirements of CHEC. Fig. 46 shows a plot with the CHEC requirements and the IceAct performance that was determined with the different methods described above. The fractional charge resolution of the short integration interval is better than required for CHEC for all $N_{p.e.}$ for which it could be determined. However, the charge resolution can only be determined (meaningfully) up to a number of photons of $N_{p.e.} \approx 239$ with this method.

When the error of the NSB is taken into account, the fractional charge resolution of the long integration window does not lie below the requirement for CHEC for low intensities below 79 photon events. For higher intensities, however, the long integration window shows a better charge resolution than required and it increases the highest possible number of p.e. for which a charge resolution can be defined to $N_{p.e.} \approx 500$. Therefore it makes sense to use a combination of both methods, where the short integration window is used

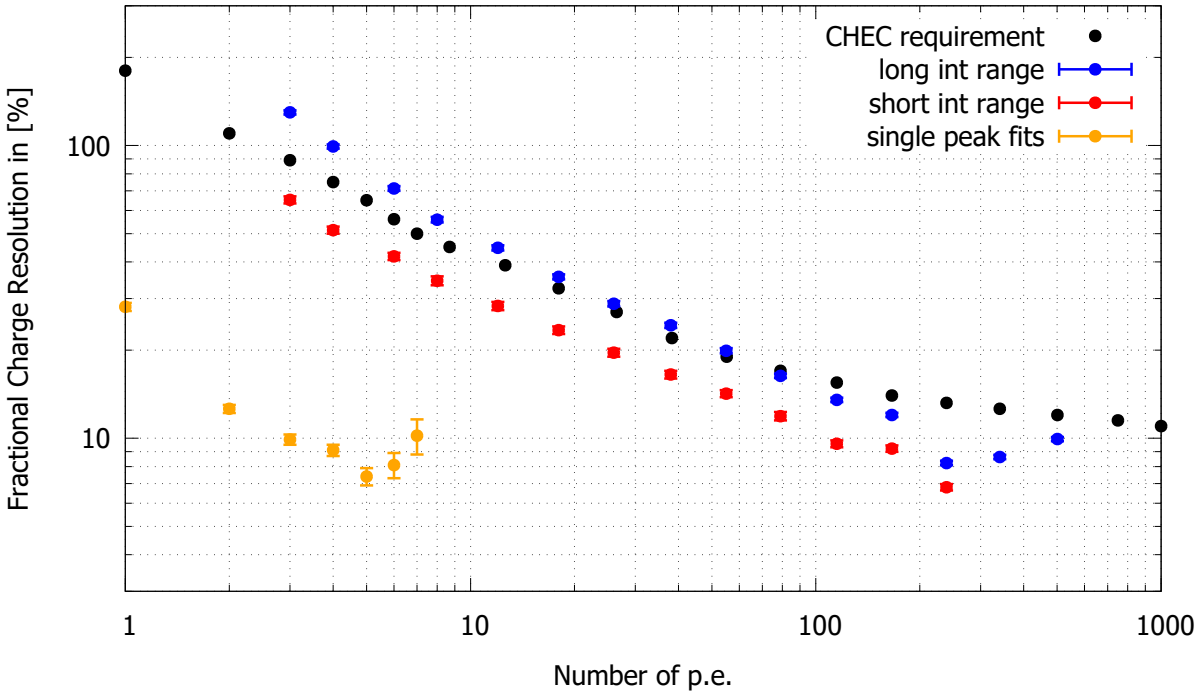

Figure 46 – Comparison of the fractional charge resolution of the IceAct SiPM (determined for the short and long interval and for the fit of individual peaks) with the CHEC requirements. For the short interval the charge resolution of the IceAct SiPM is better than required for CHEC. For the long interval it does not meet the requirement for low intensities below 79 p.e., due to the error induced by the NSB. For higher intensities it surpasses the requirements and increases the intensity for which a well defined charge resolution can be determined to $N_{p.e.} \approx 500$. The charge resolution for the individual peak fits is almost an order of magnitude better than the requirement and thus the electronic noise and SiPM excess noise are negligible.

for precise measurements for low intensities and the long integration window is used to extend the saturation range to higher numbers of photon events.

The single peak fits show the charge resolution that would be possible if only the electronic noise of the measurement setup with the Target ASIC was the limiting factor. They are almost an order of magnitude below the actual possible charge resolution. Thus, the contribution of electronic noise and SiPM excess noise is negligible.

6.5 Outdoor Measurements with the Telescope

The single SiPM was put in the telescope tubus to measure the night sky outside the ECAP building in the city area of Erlangen. For this purpose, a mount to hold the single pixel SiPM in the telescope at the place of the camera has been constructed. The telescope was pointed straight up and a cone of black cardboard was applied around the lens to shield it from stray light. The average temperature was roughly $-5^\circ C$ during the measurement time and the sky was clear.

First, a trigger scan over the night sky background was performed, which is shown in Fig. 47. The Thresh value was set to 2000 and the PMTRef4 value was varied from 1800 to 2200. The green curve marks the first trigger scan from PMTRef4 1800 to 2100 with a step size of one and a measurement time of $100\,ms$. The red curve marks a second trigger scan with a longer measurement time of 1 s from PMTRef4 2060 to 2200.

The sudden jump in the curve at a PMTref4 value of 2048 is due to the binary resistor system that is used to set the PMTref4 value. An array of eight resistors is used to set the threshold value; similar to the bits in a binary number. At the transition value the resistor array jumps from a state of 01111111 to 10000000 and the value is determined mainly by the single most significant resistor. Due to the tolerances in the exact value of this resistor the PMTref4 setting jumps at this point.

The trigger scan of the night sky background looks as expected. At low thresholds the number of events is large ($16\,MHz$) and it decreases for higher thresholds. If only night sky background was present, this decay would continue with roughly the same slope.

In the presence of cosmic rays one would expect to see a change of slope in the graph when the cosmic rays spectrum becomes dominant for higher thresholds. This is not visible in the measured data, however. With only a single active pixel, and without Winston cones, the telescope does not detect cosmic events with a sufficient rate to dominate the background. However, in the full telescope four pixels will each form a trigger group that has to surpass a certain threshold to issue a trigger command. Only if the threshold of two trigger groups is surpassed a camera wide readout event will be triggered. This greatly suppresses the background because the probability that two trigger groups will receive enough night sky background photons to trigger at the same time is much lower than for a single pixel. The single SiPM cannot profit from this and thus the rate of observed night sky background events is much higher.

Nevertheless, even with only a single pixel, the telescope can detect cosmic ray events. First a pedestal file was taken and then the night sky was observed for 1000 seconds.

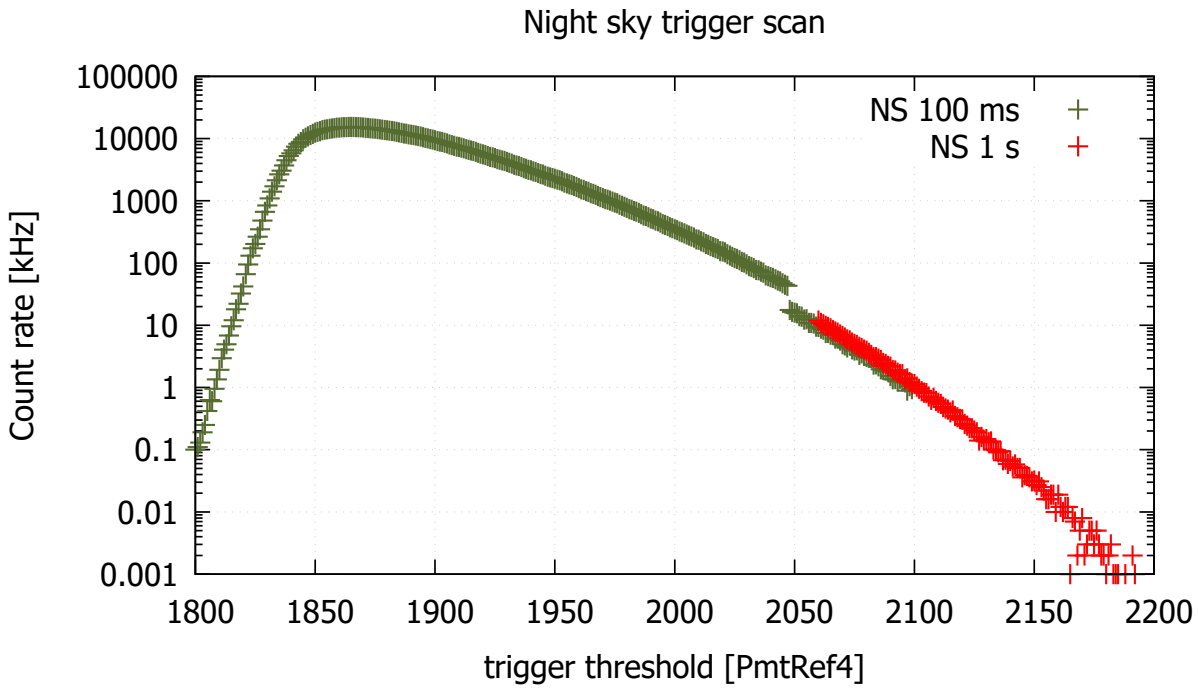

Figure 47 – Trigger scan over night sky background with the single pixel telescope.

Pedestal calibrated events that exceed an amplitude of 400 ADC counts are shown in Fig. 48. The transition between night sky background and cosmic ray events is fluent but the events with the highest amplitudes are almost certainly produced by cosmic rays.

7 Future Perspectives

7.1 Test of the Full Camera

After the research phase for this thesis ended, the full camera board with 64 SiPM pixels was finished by the manufacturer and it will be available for testing in the near future. In principle, the same steps as for the one Pixel SiPM and evaluation board can be repeated with the full camera board and the Target module. Furthermore, a test of the camera in the homogeneous laser field of the testing box is needed to calibrate all pixels. In a next step, the Winston cones can be applied to the camera which will greatly boost the light acceptance of the SiPM pixels (up to factor of five).

After that, the full telescope, including the camera, can be tested in the laser box to determine the properties of the lens and optics and to examine the telescope's response to the incident angle of the light.

Finally a field test of the telescope with the full camera can be conducted. Due to the 64 SiPM pixels and Winston cones, the sensitivity of the telescope is expected to be two

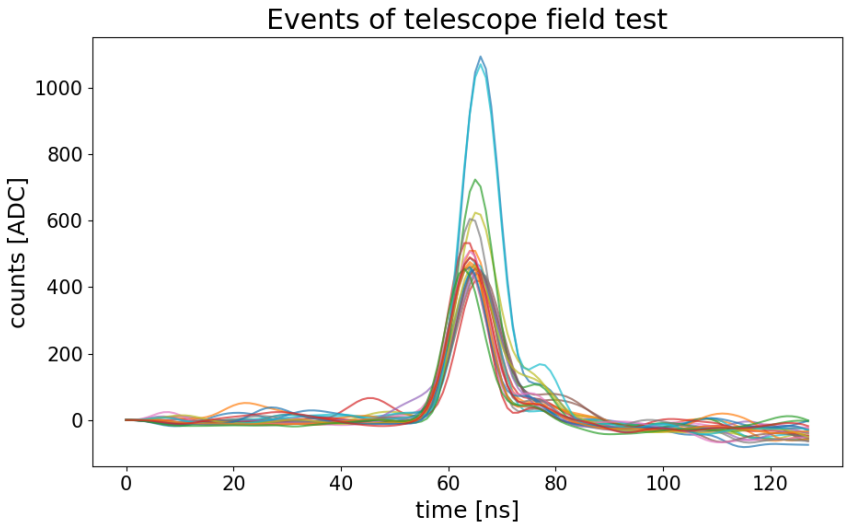

Figure 48 – Plot of cosmic events and night sky background events with an amplitude above 400 ADC counts. The two cases are not very well separable for low amplitudes. The few events with the highest amplitude are almost certainly cosmic ray events, however.

orders of magnitude higher than with the single pixel SiPM. Furthermore, several pixels can then be combined to trigger groups of four pixels each. The electronic will only trigger a readout event when at least two of the these trigger groups exceed a certain threshold. This greatly suppresses triggering on night sky background or on dark counts, because the probability that such events surpass the trigger threshold of two such four pixel trigger groups is very small.

7.2 ICE ACT Prototype at South Pole

A first prototype of the IceAct with the TARGET C/T5TEA electronics may be ready to be sent to the South Pole in the (southern) summer of 2018/2019. There, the system can be set up and tested under real (environmental) conditions over the following southern winter 2019.

8 Summary

The TARGET C/T5TEA based electronics of the newest version of IceAct are tested and characterized with a single silicon photo multiplier (SiPM) as photo detector. The data stream is examined at all points of the analog and digital data path. A short summary of the main steps and the chief results is given in the following:

Simulation with LTSpice: Simulations of the readout electronics of the IceAct have been conducted with the program LTSpice. The performance of the simulated compo-

nents, such as the SiPM, preamplifier and shaper, has been examined for different overvoltages and numbers of photon events (p.e.) in the SiPM. The results of the simulation have been compared to measurements with Target and with an oscilloscope for reference. Except for a slightly broader falling edge and the lack of a dip between the main pulse and the tail for saturated events, the simulation shows good agreement with the signal measured with the oscilloscope and is thus valid. The measurements with Target additionally show a higher than expected output that is probably due to the creation of the transfer function with a artificial preamp pulse that does not saturate, but otherwise show good agreement with the simulation. Nevertheless, the simulation reproduces many of the main features of the signal pulse and can be used to quickly check the effects that a change of (the value of) the electrical components or alterations of the measurement parameters (overvoltage, number of p.e., supply voltage, etc.) will have on the signal.

Additionally, the saturation behavior of the preamplifier and the shaper is simulated and a clear understanding of the processes that lead to the elongated pulse tail for saturated pulses is achieved. The dip in the signal between the main peak and the saturated pulse can, however, not be reproduced. From the simulation, it is evident that the preamplifier saturates first, even for the modified shaper version and thus no dynamic range is lost when using the modified shaper version.

Calibration: The performance of the SiPM, the electronics (preamplifier and shaper) and the Target C/T5TEA evaluation board has been analyzed. First by examining dark count signals and later by illuminated measurements in a homogeneous, laser field of tuneable intensity. A pedestal calibration and common mode correction have been performed and a transfer function has been applied. The common mode correction takes care of temperature induced baseline shifts that occurred during measurements and the tf calibration converts internal ADC counts to voltage values.

Area spectrum and charge determination: To recover the number of photons that are recorded with the SiPM (related to the energy of an air shower), the area underneath the signal pulses has been determined. The area (called "charge") is proportional to the number of p.e. in the SiPM and is determined by integrating the voltage values of the calibrated waveforms in an interval around the peak position. The size and position of this fit interval is determined methodically to achieve the best possible charge resolution and is set to an interval of $-6\,\mathrm{ns}$ to $+8\,\mathrm{ns}$ around the peak position of the signal pulse. The charge per p.e. was determined by the distance between the one p.e. and the two p.e. peak in the area spectrum that was taken under illumination with low intensity laser light and is: 40.79 ± 0.22 in $[\frac{mV \cdot ns}{p.e.}]$.

Comparison of the shaper versions: A modified version of a CHEC shaping circuit for analog pulse shaping is compared to the standard issue in respect for signal gain and performance. The modified version shows a stronger shaping and shortening of the pulse that compensates the longer pulse tail of the used SensL SiPM. Its gain is ~ 2 times higher

than for the standard version. This enables better charge resolution without cutting the dynamic range, as the preamplifier is the limiting factor for saturation. Overall, the modified version has proven to be the favorable choice for the IceAct and has been used to determine the charge resolution and the saturation behavior of the setup.

Parameter optimization: From the dark count measurements the change of the gain with respect to the overvoltage of the SiPM was determined. The overvoltage was set to achieve a gain of 4 mV per photon event. Later this proved too low to yield a good area spectrum where individual peaks are recognizable and it was increased to a gain of $7.5\,mV$ per p.e. (30.4 V). Furthermore the signal offset VPED was increased from 1100 to 1200 in order to shift the signal to an area of the transfer function where it yields a better resolution. This comes at the cost of dynamic range, but greatly improves the charge resolution.

Determination of the laser intensity in p.e.: To determine how many photons of the laser pulse are recorded with the SiPM for a given intensity the Poisson distribution of the number of photons in the laser pulse is used. For a low intensity ($N_{p.e.} \approx 3$) the area spectrum clearly shows the Poisson distribution of photons in its peak structure and the mean number of p.e. (without crosstalk) can be determined from it. By relating this number of p.e. to the measured laser intensity (in [V] by a photodiode), it is possible to calculate the mean number of p.e. for all used intensities.

Saturation behavior and extension of the fit window: The signal pulses saturate at ~ 239 p.e., when their maximum amplitude (determined by the preamplifier and shaper) is reached. However, for fully saturated pulses a elongated plateau like tail is visible after a dip after the main pulse. The length of the tail grows with increasing light intensity and it is possible to recover the charge from the length of this tail to some extend. Therefore the integration window is extended (long integration interval) to the end of the readout window and has no a typical width of 70 ns depending on the peak position of the signal. With this method the charge can be reconstructed up to ~ 800 photon events.

Charge resolution: The fractional charge resolution of the single SiPM pixel is determined by dividing the error of the charge measurement by the charge itself for each laser intensity. The error in the charge is determined from the sigma of the total charge in the area spectrum for each intensity. The error in the charge, that is produced by the Poisson statistic of the laser, is known and subtracted from the measurements as it is artificially induced by the laser and would not be present for real measurements of air showers with the IceAct telescope. An error of the charge measurement, that would be produced by the night sky background (NSB), is added to the measurement (under assumption of a NSB rate of 125 MHz), as no NSB was present for the measurements in the laser test box. The final error of the charge (σ_{real}) is thus a realistic estimation of the performance of a single SiPM of the IceAct telescope under real conditions.

As there are no official IceAct requirements, the fractional charge resolution of the IceAct is compared to the requirements for the camera system CHEC for CTA. For the short integration interval it is better than required for CHEC up to its saturation at ~ 239 photon events. The long integration interval collects more noise of the (NSB) and is thus less precise for low intensities, but offers the possibility to measure a well defined charge resolution up to ~ 500 photon events. Therefore, it makes sense to use a combination of both methods: The short integration interval for precise measurements of low intensities and the long integration interval to extend the saturation range to higher intensities.

Outdoor measurements with the telescope: A field test of the telescope setup with the single SiPM as camera has been conducted in the city area of Erlangen. A trigger rate scan (TRS) over the night sky background has been performed and cosmic radiation events were detected.

A change of slope in the TRS for higher trigger thresholds, when cosmic rays become the dominating part of the spectrum instead of the NSB, was not seen with the single SiPM. However, in the full camera several pixels can be combined to trigger groups that can operate in coincidence and significantly suppress the NSB. Furthermore, for the full camera with 64 SiPM pixels and Winston cones attached to them an increase in sensitivity by a factor of at least $\sim 10^2$ is expected.

References

[1] Sven Lafebre after Swordy. https://commons.wikimedia.org/w/index.php?curid=1555202. visited at 27.03.2018.

[2] H. A. Bethe and L. C. Maximon. Theory of bremsstrahlung and pair production. i. differential cross section. *Physical Review*, 93(4):768–784, feb 1954.

[3] Raymond Davis, Don S. Harmer, and Kenneth C. Hoffman. Search for neutrinos from the sun. *Physical Review Letters*, 20(21):1205–1209, may 1968.

[4] Manlio De Domenico, Mariangela Settimo, Simone Riggi, and Eric Bertin. Reinterpreting the development of extensive air showers initiated by nuclei and photons. *Journal of Cosmology and Astroparticle Physics*, 2013(07):050–050, jul 2013.

[5] Dainis Dravins. Intensity interferometry: optical imaging with kilometer baselines. In Fabien Malbet, Michelle J. Creech-Eakman, and Peter G. Tuthill, editors, *Optical and Infrared Interferometry and Imaging V*. SPIE, jul 2016.

[6] IceCube Collaboration et al. Icetop: The surface component of icecube.

[7] J. Beringer et al. Review of particle physics. *Physical Review D*, 86(1), jul 2012.

[8] Jan Auffenberg et al. Design study of an air-cherenkov telescope for harsh environments with efficient air-shower detection at 100 tev.

[9] V. F. Hess. Ueber Beobachtungen der durchdringenden Strahlung bei sieben Freiballonfahrten. *Physikalische Zeitschrift*, 13:1084–1091, November 1912.

[10] S. Funk, D. Jankowsky, H. Katagiri, M. Kraus, A. Okumura, H. Schoorlemmer, A. Shigenaka, H. Tajima, L. Tibaldo, G. Varner, A. Zink, J. Zorn, and for the CTA Consortium. Target: A digitizing and trigger asic for the cherenkov telescope array.

[11] Benedikt Herrmann. Development and characterization of a test stand for compact high energy camera (chec-s) mass test. Master's thesis, FAU Erlangen Nuernberg, 2018.

[12] Arpad Horvath. The geometry of the cherenkov radiation. https://upload.wikimedia.org/wikipedia/commons/6/6b/Cherenkov.svg, March 2006.

[13] et al. J.E. Dickinson, J.A. Hinton. A new air-cherenkov array at the south pole. *Nuclear Instruments & Methods in Physical Research*, 1999.

[14] Manuel Loos. Characterization of the hamamatsu s12642-1616pa silicon photomultiplier with the newest generation of target asic. Master's thesis, Friedrich-Alexander-Universitaet Erlangen-Nuernberg, 2017.

[15] L. W. NAGEL. Spice-simulation program with integrated circuit emphasis. *Memo No..ERL-M382, Electronics Research Laboratory, Univ. of California, Berkeley*, 1973.

[16] Karlsruhe Institute of Technology. Galactic knee and extragalactic ankle, 2017.

[17] Johannes Schafer. Parameter optimization of the t5tea-asic for the cherenkov telescope array. Master's thesis.

[18] Martin Schroeder. Particle showers produced in earths atmosphere. https://veritas.sao.arizona.edu/, 2012.

[19] L. Tibaldo, J. A. Vandenbroucke, A. M. Albert, S. Funk, T. Kawashima, M. Kraus, A. Okumura, L. Sapozhnikov, H. Tajima, G. S. Varner, T. Wu, A. Zink, and for the CTA consortium. Target: toward a solution for the readout electronics of the cherenkov telescope array.

Acknowledgments

At this point I would like to thank everyone involved in the creation of this Master Thesis for their help and support. In particular:

- Prof. Dr. Stefan Funk for giving me the opportunity to write my Thesis at this chair and for providing me with a very interesting topic
- Dr. Adrian Zink for providing help and advise whenever needed

Finally I want to thank everyone at the chair for the great working atmosphere. I really enjoyed my time here!

Eigenständigkeitserklärung

Ich versichere hiermit, die Masterarbeit ohne fremde Hilfe und ohne Benutzung anderer, als der angegebenen Quellen angefertigt zu haben und dass die Arbeit in gleicher oder ähnlicher Form noch keiner anderen Prüfungsbehörde vorgelegen hat. Alle Ausführungen der Arbeit, die wörtlich oder sinngemäß übernommen wurden, sind als solche gekennzeichnet.

Erlangen, den 14. Juni 2018

_ _ _ _ _ _ _ _ _ _ _ _ _ _ _ _